Direct determination of the phase of a structure factor by X-ray imaging

Maria Civita

Supervisor: Prof. Dr. Ian K. Robinson

London Centre for Nanotechnology

University College London

March 2015

Introduction

A typical X-ray diffraction experiment is performed by illuminating the sample with an X-ray beam and by collecting the resulting diffraction patterns in the far field. In this configuration we are only able to collect part of the information contained in the transmitted wave: its intensity can be recorded with the use of a detector while the phase is lost. This is what we usually call “the phase problem”. In crystallography, the missing phases are usually derived by self consistency with known physical properties of the crystal, that the electron density is real and mostly confined to the cores of the atoms in the unit cell. The development of computational "direct methods" in the 1950’s led to a revolution in crystallography because it allowed direct inversion of diffraction patterns to atomic-resolution real-space images of the crystal structure [1, 2].

Interference methods can be used to measure phases experimentally. The magnitude of one structure factor is predicted to become modulated in a characteristic way when a second Bragg peak is simultaneously excited [3]. The shape of the interference is determined by the relative phases of the two refections involved, and implicitly by that of the difference reflection [4, 5], which are all coupled through the dynamical theory of X-ray diffraction [6]. This has been developed into a practical method for measuring "triplet phases" comprising of the sums of the three phases involved. When enough triplets are known, the individual phases can be deduced and the structure solved [7, 8]. A Bonse-Hart interferometer was used by Hirano and Momose to measure the change in phase of an X-ray beam transmitted through a diamond crystal when a Bragg reflection was excited [9]; as we will show in this Thesis, the effect can be used to measure structure-factor phases. A more direct interference method was recently proposed by Wolf [10] in which the mutual coherence function is evaluated between the direct beam and a single Bragg reflected beam. Since this contains their relative phases, the unknown phase of the Bragg reflection can be extracted. This method has not yet been demonstrated

for X-rays.

In this Thesis work a new method, related to that of Wolf [10], in which the phase of the direct beam transmitted through a crystal is shown to change whenever a Bragg peak is generated will be proposed and demostrated. Since only one diffracted beam is involved, its phase relative to the incident beam is directly determined, without the need for decoding of triplet combinations [7, 8]. The reflected beam needs to be strong enough to influence the forward beam, so the diffraction has to be at least at the beginning of the dynamical regime [6]. The novelty of our method is to measure the phase of the forward beam, using the powerful phase sensitivity of the new X-ray ptychography method [11]. By imaging the phase of the crystal under investigation by ptychography [12] we can accurately measure the phase shift of the beam as it is transmitted through the crystal. This phase shift, which is sensitive to the X-ray refractive index and thickness, is found to change when a Bragg peak is generated inside the crystal.

In Chapter 1 an introduction to X-ray microscopy will be presented starting from a more general overview of modern microscopy. The main aspects of the dedicated optics and traditional setups will be discussed.

Chapter 2 will describe the phase problem in the X-ray Coherent Diffraction Imaging (XCDI) technique and will provide an overview on the most important phase retrieval methods.

In Chapter 3 the attention will be focused on Ptychography. Here different phase retrieval algorithms will be discussed. At the end of this chaper the artifacts introduced in the reconstructed phase will also be discussed, proposing methods that can be used for their correction.

Chapter 4 will discuss the kinematical and dynamical diffraction theories, after a brief introduction on X-ray cristallography.

In Chapter 5 we will discuss the experimental implementation of our phase shift retrieval method by showing the results obtained on a gold nanocrystals sample.

Chapter 6 will show how we designed and produced another set of Si and InP samples in order to continue our experimental investigations.

In Chapter 7 the last results obtained on our Si and InP samples will be presented and discussed.

Chapter 8 will present the conclusions that we could draw after comparing all our experimental results.

Acknowledgements

The completion of this research project would have not been possible without the contribution of many people who supported me during these past few years.

The first person that I would like to thank is my supervisor, Prof. Ian Robinson, who has always believed in this project and whose passion for the research activity has inspired me throughout all these years. His understanding and patience have helped me many times and his humanity and generosity gave me an example that I will try to follow for the rest of my life.

Another very important person that I would like to thank is Dr. Graeme Morrison, who has always been there for me with good advices and smart suggestions. I really had the best time with him and Dr. Malcolm Howells at the TwinMic beamline, where we went several times to perform experiments on structured illumination.

My deepest gratitude goes to Dr. Ana Diaz, beamline scientist at the cSAXS beamline at the Swiss Light Source synchrotron, whose dedication was extremely important in achieving our first experimental results. I would also like to thank Dr. Ross Harder, beamline scientist at the APS 34-IDC beamline, for his support during the many experiments that we conducted with him.

I also had a great time together with my fellow team members. Thanks to them I have many good memories that will always put a smile on my face.

Last but not least, I would like to thank my family.

My husband Guido who has always been there for me with his love and support, giving me the strenght to overcome the many difficulties that I encountered during these years.

My mother Luigia who has always put her needs aside so that I could pursue my dreams. Thank you mom for being the strongest person I know!

Contents

Chapter 1

X-Ray microscopy

1.1 Introduction to modern microscopy

The concept at the basis of a microscope is to use a system of lenses to focus a beam of visible light in order to obtain magnified images of small samples. This basic idea has been developed in many different ways throughout the years because the resolution that one can get from a microscope is limited by the wavelength of the radiation being used to illuminate the samples. Furthermore there are cases where the samples are opaque to visible light so that one need to use a different radiation in order to get not only a higher resolution but also a better penetration.

One first example is the Transmission Electron Microscope (TEM) whose concept follows the same principles at the basis of the light microscope but uses a beam of electrons instead of light. On one side the source's much lower wavelength leads to a dramatic improvement in terms of resolution which makes it possible to see objects to the order of a few angstrom, but on the other hand the TEM has also limitations. In fact unless the sample is very thin, electrons are either absorbed or scattered within the object rather than transmitted. For this reason other research has been consucted in order to develop new electron microscopes which can be capable of examining relatively thick (also called bulk) specimens [13].

In the Scanning Electron Microscopes (SEM) the high-energy electron focused beam is used to scan the specimen. The concept here is to use the waves that are generated by the beam-sample interactions in order to get high resolution images of objects shapes as well as to show spatial variations in chemical

compositions [14]. One important requirement in using this microscope is that the samples must at least have an electrically conductive surface. In most cases specimens to be analyzed are allocated in a proper vacuum chamber and the whole acquisition is remotely assisted using a software. The image resolution which varies between 3 and 10 nm, is much higher to the one obtained with light microscopes but it is not as good as the one that one can get with a TEM acquisition.

Scanning microscopes are another important class of devices. The basic idea is to mechanically scan the sample's surface using a pointed tip, which is commonly known as probe, in order to get the object's local properties. The main difference between the microscopes in this group is the distance between the probe and the sample's surface. The Scanning Tunneling Microscope (STM) [15] was the first one developed in this class and here the probe-surface distance is of approximately 1 nm. Another example is the Atomic Force Microscope (AFM) where the probe is so close to the sample's surface that it basically touches it and senses an interatomic force [16]. In both cases it is possible to achieve a very high resolution (0.1-0.5 nm) but the big limit to these microscopes is that the information that one can get is relative to the sample's surface and not from what lies below it.

In order to overcome this limitation X-ray microscopes have been developed. They are particularly powerful in imaging those samples whose structures are on length scales that are intermediate between those probed by optical and electron based techniques.

The following table presents a summary of what has been said so far, also including the nano-probe microscopes which will not be treated in this report.

Microscope Type	Detect	Resolution	Contrast
visible light	transmitted light	500 nm	bright field
		500 nm	phase contrast
	scattered light	500 nm	dark field
	fluorescence	50 – 500 nm	label
electron microscope (TEM)	scattered electrons	0.1 – 1 nm	heavy metal stain
scanning electron micr. (SEM)	secondary electrons	3 – 10 nm	surface relief
scanning tunneling micr. (STM)	tunneling current	0.1 nm	surface atoms
scanning force micr. (AFM)	force on probe tip	0.5 nm	surface relief
X-ray projection microscope	transmitted X-rays	>1000 nm	absorption
X-ray microscope (TXM)	transmitted X-rays	25 nm	absorption
		25 nm	phase contrast
scanning X-ray microscope (STXM)	transmitted X-rays	25 nm	absorption
			XANES (chemical)
nanoprobe	fluorescence	30 nm	elements
	diffraction	30 nm	strain

Figure 1.1: Overview table on modern microscopes adapted from the Xradia website.

1.2 X-ray microscopes

X-ray microscopes are characterised by a higher resolution, compared to the optical ones, due to the small wave length and by large penetration distance and small radiation damage when compared to electron microscopes. In the past few decades X-ray microscopy has seen a great development [17] given not only by the availability of high resolution X-ray optics to be used together with high brightness synchrotron light sources, but also due to the advancements in scientific research in general with the need of always greater resolutions. Furthermore X-ray microscopy offers both spatial and chemical-physical information so that is has become extremely popular and widely used.

Third generation synchrotrons are characterized by an high Brilliance, defined as the number of photons generated per unit time per unit source area (mm^2) per unit solid angle ($mrad^2$) per 0.1% fractional bandwidth ($\Delta\lambda/\lambda$), and by a sufficiently coherent flux depending on the emittance of the circulating electron beam [18]. In the synchrotron electrons are accelerated in a vacuum environment within a storage ring. The presence of straight sections of undulators in the ring assures that electrons do not follow a purely circular orbit. In this way they are forced to execute small-amplitude oscillations which cause the emission of X-rays. When the different contributions add coherently, the resulting

beam is extremely intense. Another important component is the monochromator which permits to choose a wavelength bandwidth in accordance with what is needed for the experiment. Last but not least for importance, the focusing devices which are necessary to illuminate the sample and to achieve an high resolution.

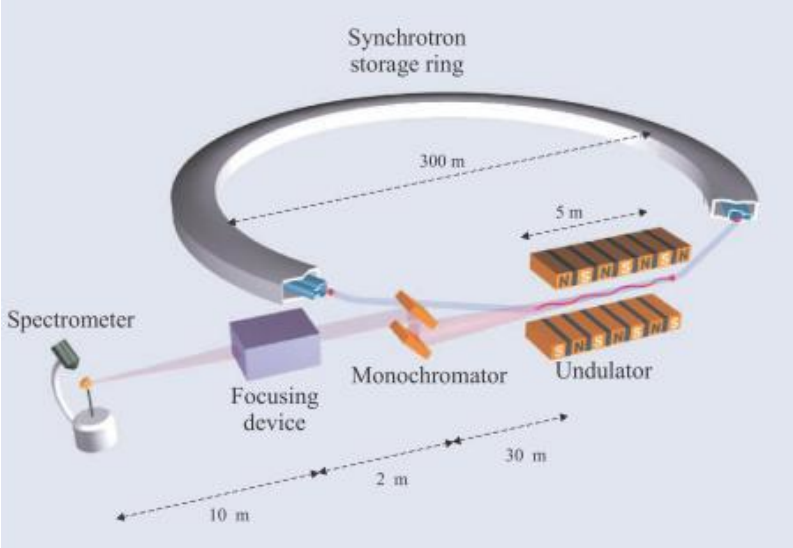

Figure 1.2: Schematic of a typical X-ray beamline at a third generation X-ray source. Here the undulator is pictured as composed by a straight magnets lattice. Figure extracted from [19].

1.2.1 Focusing devices

The first focusing devices developed for X-rays were the KB mirrors, owing their name to their inventors Kirkpatrick and Baez in 1948 [20]. The system is based on two curved mirrors which are placed orthogonally with respect to each other and designed such that they both focus to the same point in space.

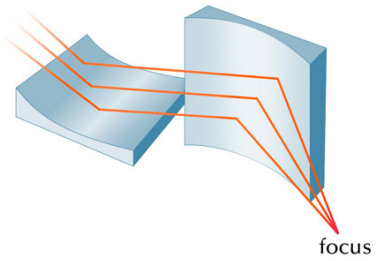

Figure 1.3: KB mirrors schematic adapted from the Xradia website.

The KB mirror system has endured to the present day and in fact we have used it during several experiments at the Advanced Photon Source facility.

Another class of lens based system comprehends Compound Refractive Lens (CRLs) [21] and Fresnel Zone Plates (FZP) which we have used several times during our experiments at APS, Elettra and Swiss Light Source.

A Fresnel zone plate typically consists of a plate with circular concentric ribs, as showed in Figure 1.4, and can be thought of as a circular diffraction grating.

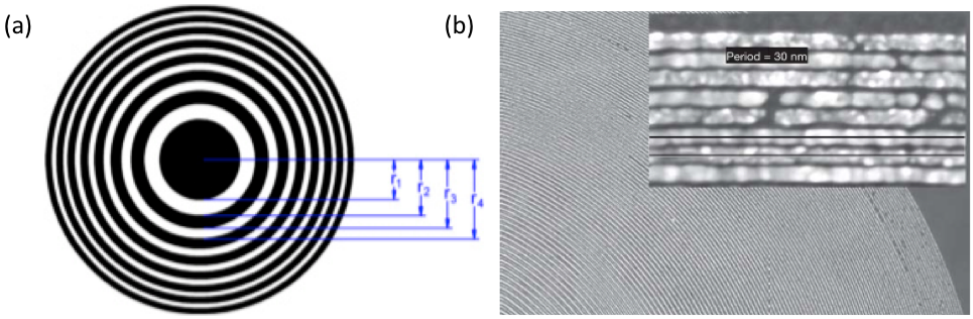

Figure 1.4: Schematic representation of a FZP (a) and scanning electron micrograph of a zone plate with 15 nm outermost zone (b) [22].

The structure of a zone plate is made in such a way that the spacing between the peripheral rings becomes much smaller going to the edge of the plate itself. This is important because in this way the FZP works like a lens with different focal points. In fact the focal distance is related to the spacing between the rings by the formula

$$f_n = \frac{D^2}{4n\lambda} = \frac{Dd_n}{\lambda} \tag{1.1}$$

where D is the zone plate diameter and d_n is the spacing between two rings in a defined region of the FZP. For this reason, when fully illuminated, the zone plate presents several diffraction orders and it is possible to select one by using an Order Sorting Aperture (OSA) downstream of the beam. This will be better illustrated when talking about the Scanning Transmission X-ray Microscope (STXM).

1.2.2 Transmission X-ray Microscope

The first TXM was built at Gottingen University by the group of Günter Schmahl [23]. A representative layout is shown in Figure 1.5. It is similar to a regular optical microscope.

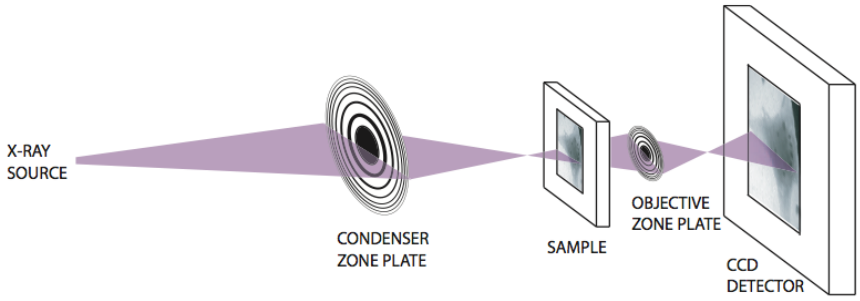

Figure 1.5: TXM schematic. The two condenser and objective zone plate lenses are combined to form an image which is then collected on a charge coupling detector. This setup also uses an order selecting aperture between the two zone plates but it is not shown in this representation. Figure adapted from [24].

In this microscope the sample is illuminated with a focused beam obtained by using a large FZP, the condenser zone plate, which also blocks the direct beam with a central stop. Downstream of the sample is a micro zone plate, usually called objective, which provides a magnified image that is then collected on a CCD detector. An order selecting aperture (OSA) is usually inserted between the condenser zone plate and the sample in order to block the zero and high order diffractions.

1.2.3 Scanning Transmission X-ray Microscope

A Scanning Transmission X-ray Microscope, STXM, works in a way similar to that of a Scanning Electron Microscope (SEM) [25]. The first STXM using a zone plate focused X-ray beam was built by the Stony Brook group at the National Synchrotron Light Source (NSLS) at Brookhaven National Laboratory. Figure 1.6 shows the configuration of a typical STXM.

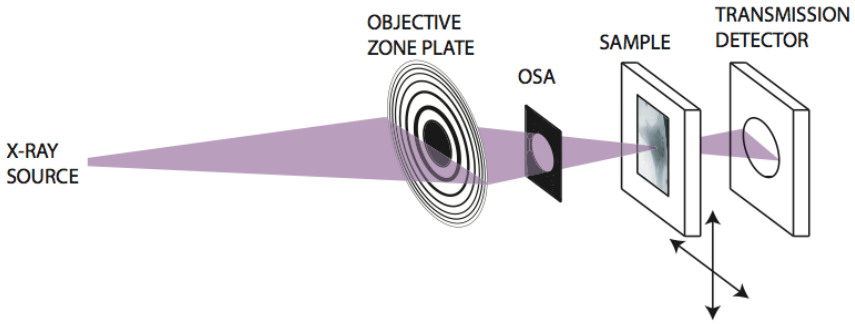

Figure 1.6: STXM schematic representation. The focused beam is obtaine by a FZP-OSA cascade. In this configuration the sample is mounted on a translating stage which moves on a plane perpendicular to the beam. The experiment is performed by scanning the sample and by consequently recording the different diffraction patterns on the downstream transmission detector. Figure adapted from [24].

In this microscope a monochromatic X-ray beam illuminates the objective zone plate which then focuses the beam onto the sample with the use of an order selecting aperture which blocks the unwanted diffraction orders. The sample is mounted on a piezoelectric stage which moves on a plane perpendicular to the beam. In this way the sample can be scanned while keeping the focused beam fixed. For each sample position, th beam emerging from the speciemen is then collected by a downstream detector.

During my PhD I first used a STXM to obtain quantitative phase contrast images during my experiment at the cSAXS beamline at the Swiss Light Source facility. The method that we applied is the Differential Phase-contrast (DPC) X-ray imaging that uses information concerning the phase gradient of an X-ray beam that passes through an object (whose refractive index is complex) in order to create its images [26]. In this case the phase gradient causes a redistribution of the intensity across the detector plane. The idea is then to use an anti-symmetric detector response function that will be sensitive to the redistribution of the intensity. In this experiment, which will be described in detail later in Chapter 5, we were looking at gold nanocrystals deposited on a membrane. We firstly defined a region of interest around the crystal and then we calculated the differential phase contrast along both the x and y directions on the sample plane, as well as the integrated phase in the forward direction, where we had a PILATUS 2M detector at 7.2m downstream of the sample.

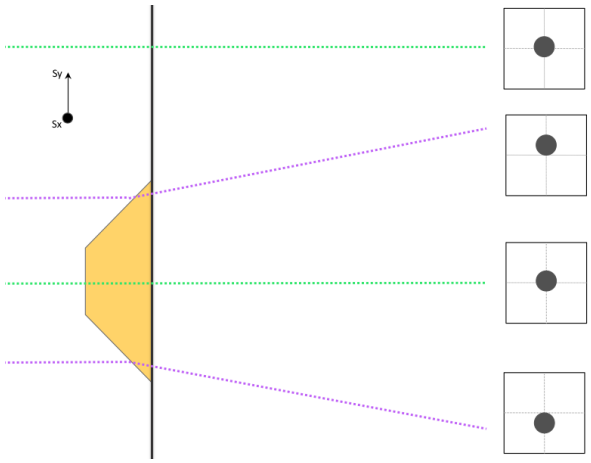

Figure 1.7: Phase contrast acquisition schematic.

The green dashed lines in Fig. 1.7 represent the beam when not touching the crystal or when hitting the crystal surface perpendicular to the beam itself. The result in these conditions was to observe a dark spot on the detector in the middle of our region of interest. If we moved the beam, for example along y (violet dashed lines in the figure), refraction occurred and as a result we saw our spot shifted along y. We then repeated the same procedure along x observing this time a shift of the spot on the left-right side. At this point we used a routine to evaluate the differential phase contrast in both directions by using the relation between the the angular deviation of the beam (dark spot) and the gradient of the phase as

$$DPC_x = \frac{\lambda}{2\pi}\frac{\partial\phi(x,y)}{\partial x} \tag{1.2}$$

$$DPC_y = \frac{\lambda}{2\pi}\frac{\partial\phi(x,y)}{\partial y}.$$

We then calculated the differential phase contrasts integrals to obtain the whole integrated phase which gave us information about the thickness of our crystal as well as the total phase shift, as described in Fig. 1.8.

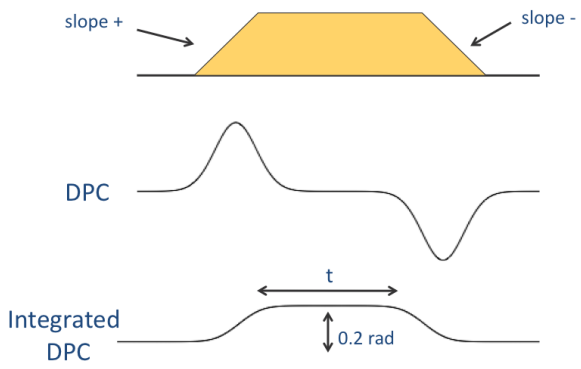

Figure 1.8: Differential phase contrast and integrated phase schematic.

The experimental results of the phase contrast analysis are showed in Figure 1.9.

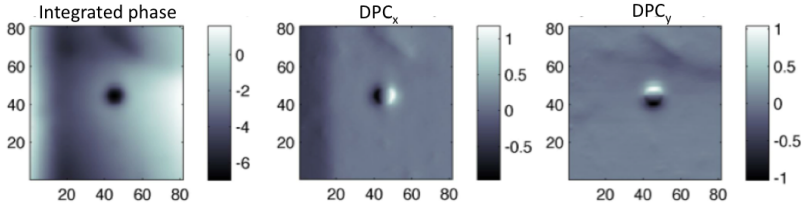

Figure 1.9: Phase Contrast analysis of a gold nanocrystal performed at the cSAXS beamline. The nanocrystal size is about 372x248nm^2(12pixel in horizontal and 8pixels in vertical, where the pixel size is around 31nm).

1.2.4 Structured Illumination Microscopy

Structured illumination microscopy (SIM) is based on the concept of illuminating the sample with patterned light and it is used to gain a factor two improvement in the lateral resolution [27] as well as to achieve optical sectioning [27, 28, 29, 30, 31]. During my PhD I took part to an experiment based on structured illumination using X-rays at the TwinMic beamline at the Elettra synchrotron in Trieste. The TwinMic X-ray spectromicroscope combines full-field imaging (TXM) with scanning X-ray microscope (STXM) in a single instrument. The idea of the experiment was to generate an incoherent structured illumination by imaging a transmission grating on to the sample using a condenser zone plate. We made a distinction between the illumination system, upstream of the sample, which made use the STXM part of TwinMic and the TXM part, downstream of the sample. A schematic representation

of the experiment is showed in Figure 1.10.

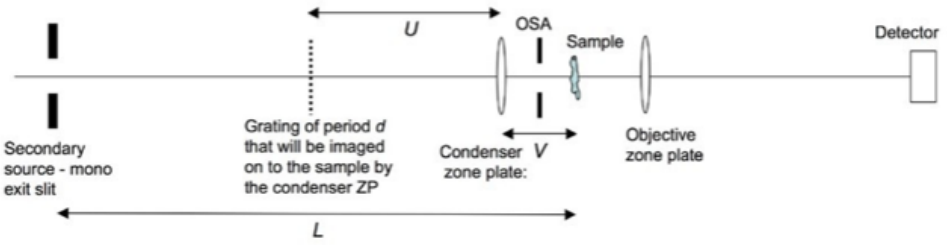

Figure 1.10: Structured illumination experiment at TwinMic.

The sample we used consisted of an etched pattern in a thin tungsten layer on a silicon nitride window. After illuminating the sample we recorded TXM images for a series of transverse shifts of the grating. Each shift moved the grating by a certain portion of a period (for instance one quarter of a period) in the manner of a phase-stepping interferometer [32] so to introduce a phase shift between the intensity functions of the sample and the grating. We then wanted to recover images of each sample section by operating a Fourier transform of the data with respect to the phase-shift variable. To demonstrate optical sectioning we needed to repeat the same procedure described above for a series of positions on and off focus. Successful sectioning would have returned a good image along an in-focus strip and darkness elsewhere. The aim of this proposal was to both achieve optical sectioning of our sample as well as increasing the resolution, but we could not succeed due to technical difficulties.

Chapter 2

Coherent X-ray Diffraction Imaging

Coherent X-ray diffraction imaging (CXDI) is a technique where an highly coherent beam of X-rays is used to resolve the structure of nanoscale samples such as nanotubes [33], nanocrystals [34] and more. The main advantage of CDI is that it does not use lenses to focus the beam so that the measurements are not affected by aberrations and the resolution is only limited by diffraction and dose. In a typical CDI experiment, the coherent beam produced by a synchrotron source is scattered by the sample so that to generate diffraction patterns which are collected downstream by a detector. The recorded data is described in terms of absolute counts of photons, a measurement which describes amplitudes but loses phase information. In order to retrieve the image of the sample in both its amplitude and phase it is then necessary to solve what is commonly called the phase problem.

2.1 The phase problem in CXDI

In CXDI diffraction patterns are collected in the far field, or Fraunhofer region, meaning that the distance between the sample and the detector must be $D > a^2/\lambda$ being a the illuminated sample size and λ the radiation wavelength. In this region the diffracted wave is given by the Fourier transform of the wave exiting from the sample

$$F(\mathbf{q}) = \int \varrho(\mathbf{r}) e^{i\mathbf{2}\pi\mathbf{q}\cdot\mathbf{r}} d^3\mathbf{r} \tag{2.1}$$

where $\mathbf{q}$ is the scattering vector and $\mathbf{r}$ is the real space vector. The $\mathbf{q}$ vector is obtained by the

subtraction of the incoming and diffracted wave vectors, $\mathbf{q} = \mathbf{k} - \mathbf{k}^{'}$, and it can also be related to the detector distance as showed in Figure 2.1.

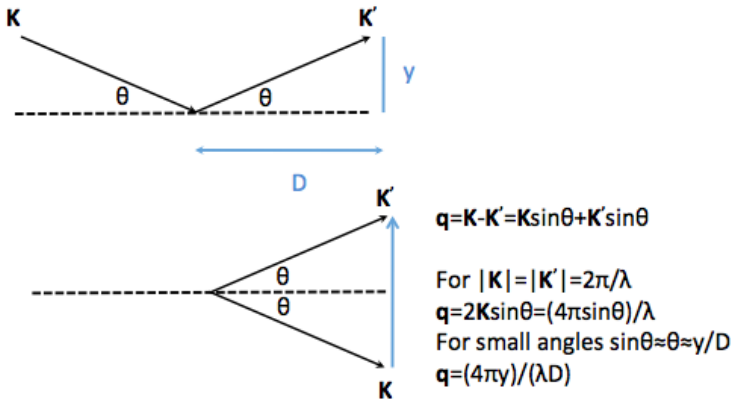

Figure 2.1: Schematic representation for calculating the scattering vector. An incoming beam of wave vector $\mathbf{k}$ hits a surface at a certain angle θ and is scattered along the $\mathbf{k}^{'}$ direction. Because $\mathbf{q}$ is by definition given by $\mathbf{q} = \mathbf{k} - \mathbf{k}^{'}$, in the case the two wave vectors are equal in modulus it is possible to say that $\mathbf{q} = 2\mathbf{k}sin\theta$. Being D the distance to the detector and y the point in which k' hits the detector (whose numerical size can be evaluated by the pixel size multiplied by the pixel number in position y), it is possible to write $\mathbf{q} = \frac{4\pi y}{\lambda D}$, in the case that θ is small enough so that $sin\theta \approx \theta \approx$y/D.

The exit wave is the complex function $\rho(\mathbf{r})$ which encloses the information about the electron density of the scattering object. It would seem straightforward that in order to retrieve all information about the sample it would be enough to just perform the inverse Fourier transform of the diffracted wave

$$\rho(\mathbf{r}) = \mathcal{F}^{-1}[F(\mathbf{q})]. \tag{2.2}$$

The problem with what stated above is that what is collected on the detector is proportional to the intensity of the diffracted wave

$$I(\mathbf{q}) = |F(\mathbf{q})|^2 \tag{2.3}$$

and so all the information about the phase of the complex function $F(\mathbf{q})$ is lost. Always keeping in mind the properties of Fourier transforms it is possible to relate the Fourier transform of the recorded

intensity to the autocorrelation function of the electron density $\rho(\mathbf{r})$

$$|F(\mathbf{q})|^2 = \rho(\mathbf{r}) \otimes \rho(-\mathbf{r}) = g(\mathbf{r}) \tag{2.4}$$

that is a non-zero function twice the size of $\rho(\mathbf{r})$. The sample phase needs to be recovered in other ways and what we usually do is to use iterative inversion algorithms with the aim of recovering the phase starting from a guess which is refined step by step.

2.2 Phase retrieval methods

In principle the process of retrieving the phase consists on extracting this information from the Fourier transform of a function when only its magnitude is known. Because an inversion method is used, starting from the the recorded intensity, it is important to establish whether the obtained solution is unique or not. In 1982, after understanding that the autocorrelation function of any sort of image is twice the size of the image itself in each dimension (as showed in the previous paragraph), Bates [35] concluded that the phase information could be recovered by oversampling the magnitude of a Fourier transform that is twice as fine as the Bragg density (2X oversampling in each dimension: 4X for two dimensions and 8X for three dimensions). In this way he showed that for 2D and 3D problems there is almost always a unique solution to the phase problem.

2.2.1 Oversampling

The sampling theorem, mainly known as the Nyquist-Shannon theory, states that one can reconstruct a band-limited function starting from an infinite sequence of samples if the band-limit B is smaller than 1/2 the sampling rate (samples per second). This can be easily understood if we consider that sampling basically means to extract a series of values from a function, and this can be seen as multiplying the varying function by a Dirac comb.

$$f(x) * \sum_{k=-\infty}^{\infty} \delta(x - kT) \tag{2.5}$$

If we move this to the frequency domain, the multiplication by a Dirac comb results as a convolution by the Fourier transform of the comb, which is still a comb, whose effect is to replicate the function's

spectrum at different frequencies.

$$F_s(s) = F(s) \otimes \frac{\sqrt{2\pi}}{T} \sum_{k=-\infty}^{\infty} \delta(s - k\frac{2\pi}{T}) \tag{2.6}$$

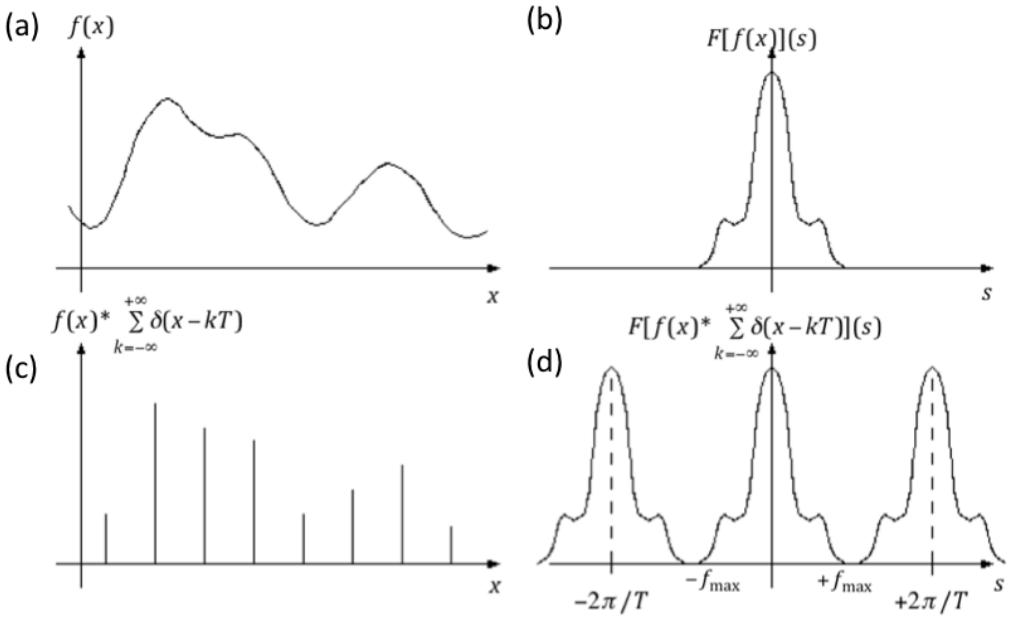

Figure 2.2: Function f(x) is showed in both space (a-c) and frequency domains (b-d). (c) shows the extration of samples from the function in the space domain while (d) is the resulting Fourier transform of the sampled f(x). Adapted from [36].

It can be easily understood from Figure 2.1 that if the sampling condition

$$f_s \geqq 2f_{max} \tag{2.7}$$

is not respected then all spectrums will overlap and aliasing will take place.

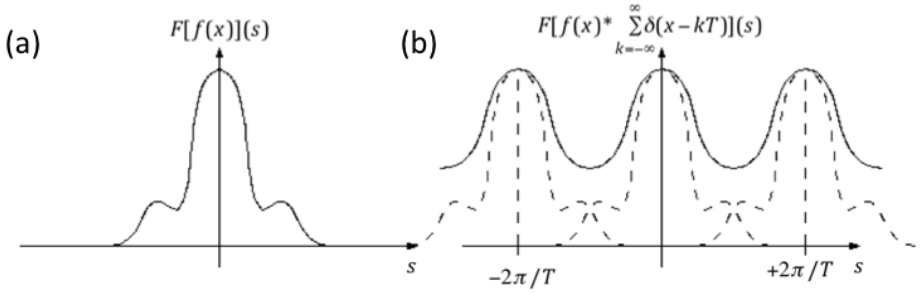

Figure 2.3: (a) Simple Fourier transform of the f(x) function. A wrong sampling results in the aliasing effect in the frequency domain (b). Adapted from [36].

Moving to our main problem, that is what to do with our diffraction intensities, we can say that given the exit wave $\rho(\mathbf{r})$, its Fourier transform $F(\mathbf{q})$ is given by

$$F(\mathbf{q}) = \int_{-\infty}^{\infty} \rho(\mathbf{r}) e^{2\pi i \mathbf{q}\cdot\mathbf{r}} d\mathbf{r} \tag{2.8}$$

where r_i are the spatial coordinates in image space and q_i are the spatial-frequency coordinates in Fourier space. Adopting this notation is convenient because what we collect is discretized in pixel units, so we need to approximate the object and its Fourier transform by arrays. If we now apply a conventional sampling and consider the discretized Fourier transform of the object function, we get

$$|F(\mathbf{q})| = \left| \sum_{\mathbf{r}=0}^{N-1} \rho(\mathbf{r}) e^{2\pi i \mathbf{q}\cdot\mathbf{r}/\mathbf{N}} \right| \tag{2.9}$$

where N is the number of pixels (from 0 to N-1 in each direction). Equation 2.9 is, according to Miao [37], actually a set of equations and the phase problem solution leads to solving $\rho(\mathbf{r})$ for each element of the array (or pixel). Finding a solution for this set of equations is not easy. First of all, due to the loss of phase there can be some ambiguities such as not being able to distinguish between these quantities: $\rho(\mathbf{r})$, $\rho(\mathbf{r}+\mathbf{r}_0)e^{i\theta_c}$ and $\rho^*(-\mathbf{r}+\mathbf{r}_0)e^{i\theta_c}$ where $\mathbf{r_0}$ and θ_c are real constants. If we concentrate on other nontrivial solutions we can distinguish between two cases. The first is to consider $\rho(\mathbf{r})$ complex and this means having, for the 1D problem, N equations to solve and 2N unknown variables (phase and amplitude for each pixel). This happens for the 2D and 3D cases where we have $N^2$and N^3equations and $2N^2$and $2N^3$variables, respectively. If we instead consider $\rho(\mathbf{r})$ to be real and

we take the central symmetry of diffraction patterns into account (Friedel's law), the equation number in the system drops by a factor of 2, as well as the number of unknown variables. Still we have a problem which is underdetermined (number of equations $<$ number of unknown variables) by a factor of 2 for all dimensions. At this point it is clear that in order to solve equation 2.9 we need to have some a priori information about our sample and we need to introduce some constraint in our set of equations if we want to retrieve the phase. Miao thought about two main strategies to solve this problem. The first strategy consists on decreasing the number of unknown variables with the use of objects characterized by a known scattering density inside them. For example one could use a sample with some non scattering density inside it so that few pixels will have a known value. In this case it is possible to consider the ratio σ

$$\sigma = \frac{total - number - pixels}{not - known - pixels} \tag{2.10}$$

being the not known pixels the number of variables to be solved. To solve the system of equations it would be enough to have $\sigma > 2$. One could argue that having an equal number of unknown variables and equations is just a necessary but not sufficient condition to solve Equation 2.9. Miao states that in these conditions this should not be a problem, referring to Barakat and Newsam's work on phase recovery[38], as well as to the important roles played by the positivity constraints[1] . Another strategy to solve Equation 2.9 is to use the oversampling method. The idea is to oversample the magnitude of the Fourier transform to make the ratio $\sigma > 2$. Extending this to two and three dimensions it is necessary to have $\sigma > 2^{1/2}$ and $\sigma > 2^{1/3}$ respectively.

2.2.2 Iterative algorithms

All iterative phase retrieval algorithms are based on the idea of assigning a phase to the diffraction intensities and refining this value at each iteration. In order to converge to a solution it is necessary to provide some constraints, related to a priori information about the sample or the experimental method. The general scheme of these algorithms is showed in Figure 2.4.

[1] In the case of x-ray diffraction, the complex-valued object density can be expressed by using the complex atomic scattering factor, $f1 + if2$ where f1 is the effective number of electrons that diffract the photons in phase (usually positive for x-ray diffraction), and f2 represents the attenuation, that is always positive for ordinary matter. The statement that f1 is usually positive and f2 is always positive is rigorously verified in experiments and for this reason it it possible to say that the object is positive, even for complex samples [37].

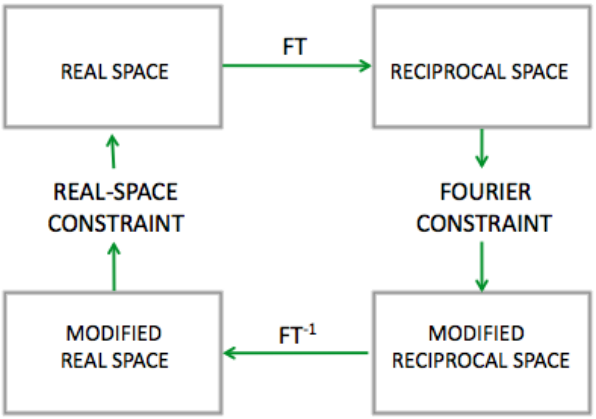

Figure 2.4: Phase retrieval iterative algorithm schematic.

If the iterative procedure gets to convergency, the now phased diffraction can be inverted to obtain the whole object reconstruction in both phase and amplitude.

The starting point of these algorithms is to define a guess of the object in the real space $\rho(r)_c$ which is then transformed, using the discrete fast Fourier transform (FFT). The resulting complex quantity is then compared with the experimental data. The computed amplitudes are then replaced with the experimental ones while the phase is kept, following the formula

$$F(\boldsymbol{q})^{'} = \frac{F(\boldsymbol{q})}{|F(\boldsymbol{q})|}\sqrt{I(\mathbf{q}_{measured})} \tag{2.11}$$

which is commonly called the Fourier constraint. What is obtained after applying Equation 2.11 it then converted to the real space by using an inverse Fourier transform. It is at this point that real space constraints are applied to get the updated object function $\rho(r)_{c+1}$. This procedure is repeated iteratively until getting to a convergency condition.

There are several algorithms which are used to retrieve the phase and here I will talk about the two that are mostly used: the Error Reduction (ER) and the Hybrid Input-Output (HIO) [39]. Both of them start with the definition of a region of space where the object is defined, the support, and it is assumed that the real space outside this region has zero amplitude for all the iterative transformations. In order to make such an assumption it is necessary to have some a priori knowledge of the sample or

to derive it from the autocorrelation function of the object function (see Equation 2.4).

The ER algorithm is directly descendant from what stated above and it consists on updating the object function in such a way that the object is always forced to only exist within the support S, whereas it is set to zero outside.

$$g_{c+1}(\boldsymbol{r}) = \begin{cases} g'_c(\boldsymbol{r}) & \text{if } \boldsymbol{r} \in S \\ 0 & \text{if } \boldsymbol{r} \notin S \end{cases} \tag{2.12}$$

This algorithm minimizes the distance between the distance between the real and Fourier space constraints at each iteration and when a local minima is reached the object function is no longer updated[39]. This can be a problem since the stagnation in the local minima condition may lead to a wrong solution.

In order to solve this problem the HIO algorithm updates the object function by using together the outputs of the current and previous iterations (c^{th} and $c-1^{th}$), controlled by a feedback parameter β whose value is usually chosen between 0 and 1.

$$g_{c+1}(\boldsymbol{r}) = \begin{cases} g'_c(\boldsymbol{r}) & \text{if } \boldsymbol{r} \in S \\ g_c(\boldsymbol{r}) - \beta g'_c(\boldsymbol{r}) & \text{if } \boldsymbol{r} \notin S \end{cases} \tag{2.13}$$

The two algorithms are also used together, for example the iterations start with the HIO to look for a solution and then there is a switch to the ER to converge to a local minimum. In this case and under certain conditions, stagnation may still occur [40].

2.3 Coherence of X-ray sources

The theoretical treatment discussed in the previous paragraphs relies on the coherence of the beam. Optical coherence occurs if, considering a given radiating region, the phase differences between all pairs of points have definite values which are constant with time. The resulting sign of high coherence is the ability to form interference fringes of good contrast [41].

There are two types of coherence that need to be specified: the longitudinal and transverse ones. An example of radiating region with longitudinally and transversely coupled points is showed below in Figure 2.4.

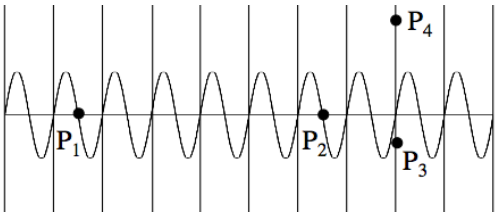

Figure 2.5: Radiating region with a couple of longitudinally separated points (P1-P2) and transversely separated points (P3-P4). Figure adapted from [41].

The longitudinal coherence length can be defined by considering two wavefronts with different wavelength which start off in phase and travel in the same direction. The distance the two wavefronts cover before going back to being in phase is defined as twice the longitudinal coherence length ($2L_{L)}$, while when they are out of phase by a factor of π the distance is only L_L.

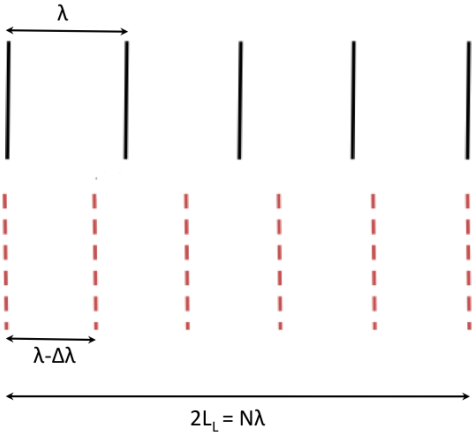

Figure 2.6: Example to show how to calculate the longitudinal coherence length L_L. Figure adapted from [19].

If we assume that $2L_L$ is equal to a multiple N of wavelengths, then it is easy to calculate the longitudinal coherence length as a function of λ

$$L_L = \frac{\lambda^2}{2\Delta\lambda}. \tag{2.14}$$

The transverse coherence length is related to the collimation of the beam, in fact in order to define it we consider two waves with the same λ emitted from a source of a finite size D.

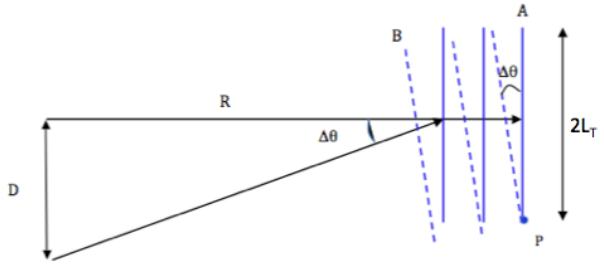

Figure 2.7: Example to show how to calculate the longitudinal coherence length. Figure adapted from [19].

In this case the two wavefronts (A and B in the figure) only differ in their propagation directions by a small amount defined by the angle $\Delta\vartheta$. At point P the wavefronts coincide and the transverse coherence length L_T is defined as the distance along A in which the two waves are out of phase. Again as for the longitudinal case, if proceeding to a distance of $2L_T$the two waves go back to being on phase. From Figure 2.7 it is easy to observe that $\lambda = 2L_T\Delta\vartheta$ where the angle $\Delta\vartheta$ can also be defined as $\Delta\vartheta = R/D$, so in the end we get

$$L_T = \frac{\lambda}{2\Delta\vartheta} = \frac{\lambda R}{2D}. \tag{2.15}$$

In synchrotrons sources the beam obtained by the circulating flux of electrons has a Gaussian shape and its coherence is defined by the undulators. In this case we define horizontal and vertical transverse coherence lengths as

$$L_{TH} = \frac{\lambda R}{2\pi\sigma_H},\ L_{TV} = \frac{\lambda R}{2\pi\sigma_V} \tag{2.16}$$

where σ_H and σ_V are the horizontal and vertical sizes of the beam, respectively. The transverse coherence can be improved thanks to the use of slits in the beamline.

The longitudinal coherence obtained in a synchrotron is related to the bandwidth of the optics used in the beamline. The most influent component is the monochromator and the optical path length difference (OPLD) between two different parts of the beam traveling in it, is defined as the longitudinal coherence of the beam. If the OPLD is smaller than the L_T the beam is in the coherent limit.

Chapter 3

Ptychography

Ptychography is an imaging method which can be considered as a development of the classical CXDI described in the previous chapter. The first inventors of Ptychography were Hegerl and Hoppe in 1970 [42], who also named it starting from the greek word 'ptycho', which means 'to fold', to describe that at the basis of this method there is a convolution operation between two functions (that is two functions folding together in mathematical terms). It was clear from the beginning that Ptychography was a useful tool to solve the phase problem, but the limits in the computing power in the early 70s did not allow a real application. For this reason it was only in the past decade that this powerful tool has been further developed and used as an imaging method. The pioneer in the field was John Rodenburg who proved in the late 90s the effectiveness of this method and provided the first inversion algorithm [43, 44, 45, 46, 47].

The X-ray ptychography method is based on the use of a confined and coherent beam, the probe, to scan an extended object at different positions. The resulting set of diffraction patterns is then collected in the far field and used to retrieve the sample's electron density. The probe position is controlled so to always assure an overlap region between two contiguous positions. In contrast to what happens in traditional Coherent X-ray Diffraction Imaging (CXDI) methods [48], Ptychography allows to use the additional information contained in the overlap regions to remove the support constraint in the real space, when reconstructing the sample using itherative inversion algorithms [49]. The redundancy of the collected dataset together with the knowledge of each scanning position, enables to reconstruct the phase of the sample without being limited by its size and at the same time allows to clearly separate

the two contributions of sample and illuminating probe. Ptychography can also be defined as a phase sensitive imaging technique because it measures the phase of one part of an object relative to other parts with high sensitivity. This new method has seen rapid development over the past few years and it has been used in many fields, from imaging computer chips [50] to biological samples [51, 52, 53]. Particularly, a phase sensitivity as good as 0.005 rad has been recently demonstrated [54]. The new frontier is to remove the requirement of perfect coherence in the beam [55].

3.1 Theoretical principles of Ptychography

The idea at the basis of Ptychography is to use an highly focused and coherent beam, the probe, to scan an extended object at different positions and to then collect the resulting diffraction patterns in the far field. This is a big difference from the CXDI described in Chapter 2 because in that case there was only one diffraction pattern, while now the dataset is composed by a number of recorded diffraction patterns, one for each probe position. The scanning probe must move onto the sample in such a way that there is always an overlap region between two contiguous illuminating positions. This causes a redundancy in the dataset which helps to retrieve the phase of the object without the requirements to oversample the diffraction patterns in the Fourier plane and to have a sample of finite extent within the coherent beam.

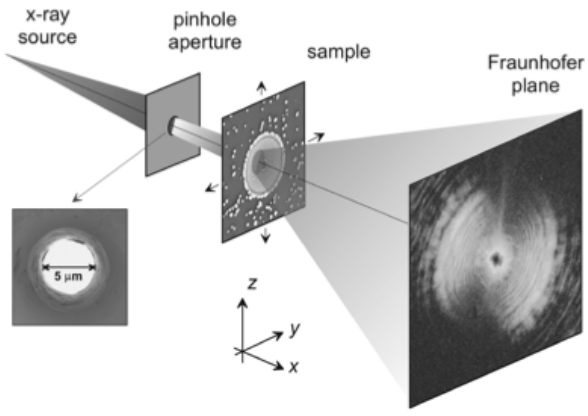

Figure 3.1: Schematic representation of the setup used by Rodenburg in 2007, extracted from his publication [45]. In this case the beam is focused with a pinhole and the sample is mounted on a 2D piezo stage which moves on the yz plane. For each probe position a diffraction pattern is recorded by a CCD camera at the Fraunhofer plane (far field).

This method has proved to be successful not only in the X-Rays regime, but also at optical [56] and electron microscopy [57] wavelengths.

The phase problem is solved with the aid of iterative inversion algorithms which transform and update functions back and forth between the real and Fourier spaces. What is different from what described in the previous chapter is that the redundancy in the collected data is used to update the object function in the real space, so that there is no requirement for a real space constraint (defined region of space where the real object exists).

There are many algorithms to process this kind of inversion, and this is something which will be briefly discussed in the last chapter of this report, but here I will describe the most robust and famous ones: PIE, ePIE and the Difference Maps algorithms.

3.2 Ptychographic Iterative Engine (PIE)

The PIE algorithm was the first one to be implemented by Rodenburg [12] and it assumes, as well as all the following methods do, a multiplicative relationship between the object and probe complex wave-functions to create the exit-wave

$$\psi(\mathbf{r}) = O(\mathbf{r})P(\mathbf{r}) \tag{3.1}$$

being $O(\mathbf{r})$ the object function and $P(\mathbf{r})$ the probe or illumination function and where $\mathbf{r}$ is the spatial coordinates vector. Rodenburg pointed out in his paper that this relation is generally accurate for thin objects. It is also assumed that $O(\mathbf{r})$ or $P(\mathbf{r})$ can be moved relative to one another by various distances $\mathbf{R}$. When using this method, the illumination function $P(\mathbf{r} - \mathbf{R})$ needs to be known. In the following description it will be considered the case of the probe moving with respect to the object, but the result would not be different if moving the object function instead. In order to use this method it is necessary to know all the illumination functions as well as all the scan positions, and of course all the diffracted intensities collected in the far field.

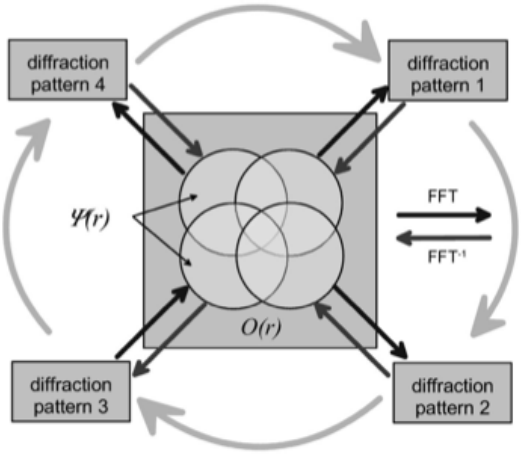

Figure 3.2: Schematic representation of how the PIE algorithm works on four overlapping probe positions (circles) illuminating a region of an extended object (central square). Figure obtained by [45].

The whole method followed by the algorithm is graphically showe in figure 3.2 and can be described by several steps.

1. The algorithm starts with a guessed (g) object function in the real space $O_{g,n}(\mathbf{r})$ at the 0th iteration.

2. It is then necessary to multiply the current guessed object function by the illumination function $P(\mathbf{r}-\mathbf{R})$ at the current position $\mathbf{R}$, so to produce a new guessed exit wave function

$$\psi_{g,n}(\mathbf{R}) = O_{g,n}(\mathbf{R})P(\mathbf{r}-\mathbf{R}). \tag{3.2}$$

3. The guessed exit wave is then Fourier transformed to obtain the corresponding function in the diffraction space, indicated by the reciprocal space coordinate $\mathbf{k}$.

$$\boldsymbol{\psi}_{g,n}(\mathbf{k},\mathbf{R}) = \mathscr{F}[\psi_{g,n}(\mathbf{R})] = \left|\boldsymbol{\psi}_{g,n}(\mathbf{k},\mathbf{R})\right| e^{i\theta_{g,n}(\mathbf{k},\mathbf{R})}. \tag{3.3}$$

It is worth noticing that this function is a guessed version of the diffracted exit wave, since it is obtained starting from a guessed object function in the real space. Because the transformed exit wave is complex, it can be decomposed in both amplitude and phase.

4. Being the dataset composed by a series of diffracted intensities, it is now possible to replace the guessed amplitude of the transformed exit wave with the recorded one

$$\boldsymbol{\psi}_{c,n}(\mathbf{k},\mathbf{R}) = |\boldsymbol{\psi}(\mathbf{k},\mathbf{R})|\, e^{i\theta_{g,n}(\mathbf{k},\mathbf{R})} \tag{3.4}$$

where $|\boldsymbol{\psi}(\mathbf{k},\mathbf{R})|$ is the modulus of the diffracted intensity.

5. At this point it is possible to inverse transform the modified exit wave, so to obtain a new improved guess in the real space

$$\psi_{c,n}(\mathbf{k},\mathbf{R}) = \mathscr{F}^{-1}\left|\boldsymbol{\psi}_{c,n}(\mathbf{k},\mathbf{R})\right|. \tag{3.5}$$

6. The guessed object function in the real space is then updated by

$$O_{g+1,n}(\mathbf{R}) = O_{g,n}(\mathbf{R}) + \frac{|P(\mathbf{r}-\mathbf{R})|}{|P_{max}(\mathbf{r}-\mathbf{R})|}\frac{P^*(\mathbf{r}-\mathbf{R})}{\left(|P(\mathbf{r}-\mathbf{R})|^2+\alpha\right)} \times \beta\left(\psi_{c,n}(\mathbf{k},\mathbf{R}) - \psi_{g,n}(\mathbf{k},\mathbf{R})\right) \tag{3.6}$$

where α and β are opportune parameters and $|P_{max}(\mathbf{r}-\mathbf{R})|$ is the maximum value of the illumination function. The value α is used to prevent a division by zero in the case that the modulus of the probe function assumes that value. The constant β controls the feedback in the algorithm and can assume values in the range between 0.5 and 1. At lower values of β the importance of the object function's newest estimate is increased, whereas the previous estimate results more revelavant when this parameter assumes higher values.

7. The algorithm continues by moving to a contiguous position, for which there is an overlapping illumination region with the previous one.

8. All steps from 2 to 7 are repeated until the sum squared error (SSE) is small enough

$$SSE = \frac{\left(|\psi(\mathbf{k},\mathbf{R})|^2 - |\psi_{g,n}(\mathbf{k},\mathbf{R})|^2\right)^2}{N}, \tag{3.7}$$

where N is the number f pixels in the array representing the wave function.

The concept underneath this algorithm is similar to other iterative phase retrieval algorithms. For the case where $\beta = 1$ and $\alpha = 0$, and the function $|P(\mathbf{r}-\mathbf{R})|$ is a mask, or support function, this method has many similarities with the well known Fienup algorithm [39].

3.3 Extended Ptychographic Iterative Engine (ePIE)

As the name suggests the ePIE algorithm is an extension of the simple PIE algorithm where the requirement for an accurate model of the illumination function is removed [58].

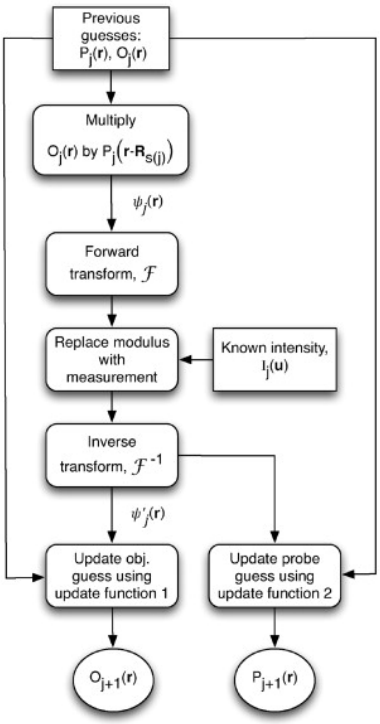

Figure 3.3: Flowchart of the ePIE method. At j=0 initial guesses at both the sample and probe waveforms are provided to the algorithm. Figure extracted from [58].

For this new version of the algorithm it is necessary to have initial guesses for both the object and probe wave-functions, labelled $O_0(\mathbf{r})$ and $P_0(\mathbf{r})$ respectively. At the starting stage of this method the object guess is considered as just free-space and the probe function is considered as a support function whose size is approximately given by the intense region of the probe wavefront. Each diffraction pattern then is considered with the update of both the object and probe guesses at each step. The result is a much quicker rate of convergence.

If compared with the PIE method, this new extended version consists on following the steps described above, with the exception of the sixth one, where is a significant change in the use of update

function, which is modified and applied to both object and probe functions.

$$O_{g+1,n}(\mathbf{R}) = O_{g,n}(\mathbf{R}) + \frac{P^*_{g,n}(\mathbf{r}-\mathbf{R})}{|P_{g,n}(\mathbf{r}-\mathbf{R})|^2_{max}} \times \beta\left(\psi_{c,n}(\mathbf{k},\mathbf{R}) - \psi_{g,n}(\mathbf{k},\mathbf{R})\right) \tag{3.8}$$

$$P_{g+1,n}(\mathbf{R}) = P_{g,n}(\mathbf{R}) + \frac{O^*_{g,n}(\mathbf{r}-\mathbf{R})}{|O_{g,n}(\mathbf{r}-\mathbf{R})|^2_{max}} \times \alpha\left(\psi_{c,n}(\mathbf{k},\mathbf{R}) - \psi_{g,n}(\mathbf{k},\mathbf{R})\right). \tag{3.9}$$

3.4 Difference Map method

The Difference Map method was initially defined in 2003 for CDI by Elser [59] and then widely adopted by Thibault for Ptychography [60, 61]. The DM algorithm solves those problems that can be expressed as the search for the intersection point between two constraint sets. The exit waves ψ_j ("views" on the specimen) definition helps to relate the two intersecting constraints.

The Fourier constraint which relates the calculated amplitudes to the measured intensities can be written as

$$I_j = \left|\mathscr{F}\left(\psi_j\right)\right|^2, \tag{3.10}$$

while the Overlap constraint imposes that each view can be decomposed into probe and an object functions:

$$\psi_j(\mathbf{r}) = O(\mathbf{r})P(\mathbf{r}-\mathbf{r_j}). \tag{3.11}$$

As it was for the PIE and ePIE algorithm, this method is based on several steps.

1. At the beginning it is necessary to produce an initial guess for the illumination function $P(\mathbf{r})$ and construct an initial state vector $,\boldsymbol{\psi} = \{\psi_1(\mathbf{r}), \psi_2(\mathbf{r}), ..., \psi_N(\mathbf{r})\}$, being N the number of probe positions, formed following Eq. 3.11.

2. The method goes on with the update of both object and illumination functions

$$O_g(\mathbf{r}) = \frac{\sum_j P^*_g(\mathbf{r}-\mathbf{r_j})\psi_j(\mathbf{r})}{\sum_j |P_g(\mathbf{r}-\mathbf{r_j})|^2} \tag{3.12}$$

$$P_g(\mathbf{r}) = \frac{\sum_j O^*_g(\mathbf{r}+\mathbf{r_j})\psi_j(\mathbf{r}+\mathbf{r_j})}{\sum_j |O_g(\mathbf{r}-\mathbf{r_j})|^2} \tag{3.13}$$

using a small number of alternate applications of equations 3.12 and 3.13 and thresholding the guessed

object function$O_g(\mathbf{r})$ to maintain all amplitudes smaller than 1.

3. Once we have arrived at this point all views contained in state vector are also updated by using the difference map update function

$$\psi_{j,n+1} = \psi_{j,n}(\mathbf{r}) + p_F\left(2P_g(\mathbf{r}-\mathbf{r_j})\,O_g(\mathbf{r}) - \psi_{j,n}(\mathbf{r})\right) - P_g(\mathbf{r}-\mathbf{r_j})\,O_g(\mathbf{r}) \tag{3.14}$$

where p_F the projection of each views onto the Fourier space constraint set, obtained by replacing the calculated amplitudes with the corresponding experimental diffraction intensities, while keeping the computed phase values.

4. The previous 2 and 3 steps are iterated until convergency is reached

$$Error_{n+1} = \|\psi_{n+1} - \psi_n\|.^2 \tag{3.15}$$

There are few big differences between the Difference Map method and ePIE. One is that the former is a parallel method which updates the object and probe functions simultaneously for the entire set of views, so that also the Fourier projection p_F can be calculated in a parallel fashion. This does not happen in ePIE, where all updates and projections are calculated serially. Another difference is in the update of the state vector, which is easier in ePIE and more complex in the DM method.

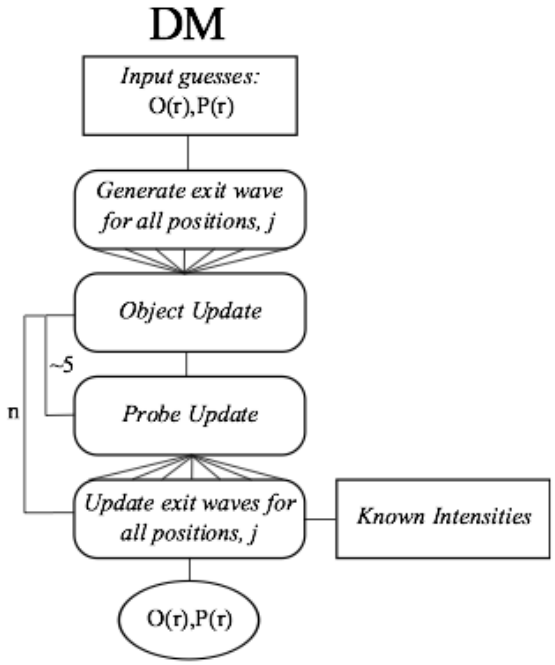

Figure 3.4: Difference Map algorithm flow-chart from [18].

3.5 Artifacts introduced in the reconstructed phase

Whenever an inversion algorithm is used to retrive the phase of a complex object function, artifacts are introduced. If on one side the phase-wrapping phenomenon is common to any inversion algorithm, the presence of phase ramps is particularly related to ptychography. The aim of this section is to address the two problems so to also explain an extremely crucial step in the data analysis presented in the following Chapters.

3.5.1 Phase wrapping

In a diffraction experiment the incoming beam illuminates an object characterized by a given refractive index n and thickness d. In a first approximation we can say that the phase of the diffracted beam emerging from the back of the sample will be affected by both n and d, so that we can assume a linear

dependency in the form

$$\phi = k\,(n-1)\,d = \frac{2\pi}{\lambda}\,(n-1)\,d.$$

The aim of a diffraction experiment is to recover the information about the sample, so the phase is used in this sense to retrieve the structure of the diffracting object which is strictly related to its thickness. So given a known refractive index, being able to quantify d starting from the reconstructed phase is of great importance. For this reason we need to make sure that the phase is deprived of any artifact introduced by the inversion algorithms being used.

The phase wrapping is a common artifact introduced by any inversion procedure because it basically relies on the fact that the reconstructed phase is constrained to assume values in the interval $[-\pi, \pi]$ and that this is independent from the nature of the sample, as shown in Figure 3.5.

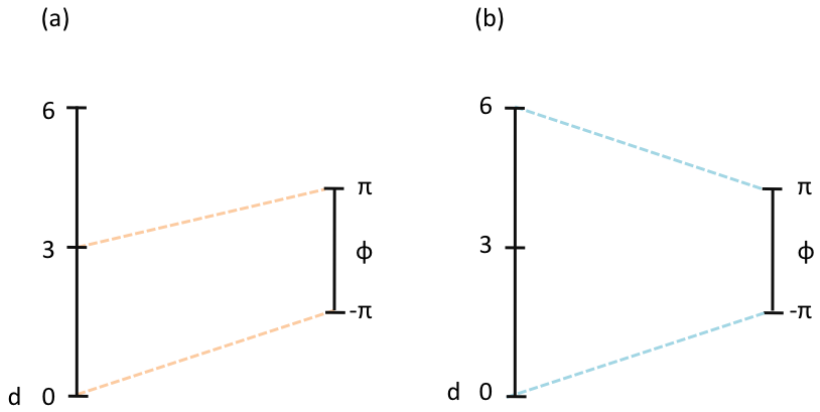

Figure 3.5: Phase assignment. (a) The reconstructed phase of a crystal whose thickness is 3 microns is correctly assigned in the $[-\pi, \pi]$ interval. (b) Even if we assume that the thickness changes to 6 microns, the reconstructed phase will still be confined in the same range. For this reason when the calculated value tries to exceed the limits, the phase profile will show jumps.

In practice the calculated phase can assume any value and typically exceedes the range $[-\pi, \pi]$. For this reason the phase profile will have jumps of $\pm 2\pi$ any place that this happens as illustrated below in Figure 3.6.

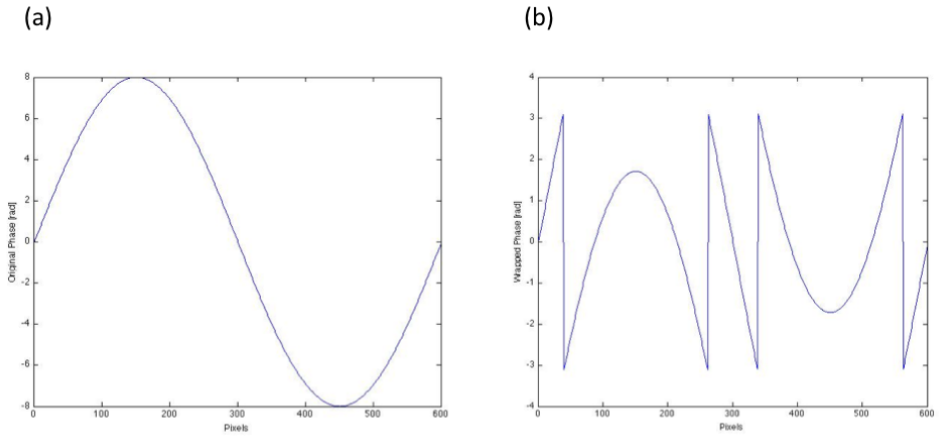

Figure 3.6: Phase wrapping. (a) The original linear phase profile varies between ± 8 radians, thus exceeding the $[-\pi, \pi]$ range. (b) The reconstructed linear phase is constrained in the $[-\pi, \pi]$ interval so that for phase values $|\phi| > 8$ we see jumps of $\pm 2\pi$.

The general approach for the unwrapping process is to estimate phase differences (gradients) between two neighboring pixels. In this way one can define a phase gradient field that is then used to reconstruct the unwrapped phase. It is also assumed that the phase difference between two adjacent pixels satisfies Nyquist's criterion, so that the discrete gradient $|\Delta\phi| = |\phi_i - \phi_{i-1}|$ should always be less than π, or half a cycle if we make the assumption that a 2π interval corresponds to a complete phase cycle.

If we consider the one dimensional case corresponding to extracting a line of phase values from a matrix, we can easily understand that a good way to estimate the phase is to integrate phase differences from point to point while constantly adding an integer number of cycles that minimizes the phase difference. By referring to the phase values as fractions of a cycle, as shown in Figure 3.7, it is easy to recognize a phase jump and to fix it in order to meet Nyquist's condition. In the example illustrated in Figure 3.7.a, a jump of amplitude 0.75 occurs between the third and fourth phase values so that it violates the condition that the maximum allowed gradient has to be less than 0.5. In this case it is possible to adjust the phases by adding one full cycle to the last three values as shown in Figure 3.7.b. The result is a phase ramp without discontinuities, since the gradient between two adjacent phase values is constant in the whole line.

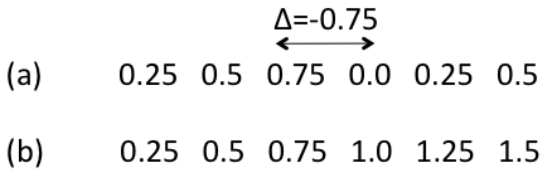

Figure 3.7: 1D phase unwrapping. (a) Wrapped phase values. The phase jump of -0.75 cycles does not respect Nyquist's criterion which demands for the maximum value allowed for a phase jump to be 0.5. (b) Unwrapped phase values. One can easily solve the situation presented in (a) by adding a complete cycle to the last three values. The unwrapped result is a phase ramp. It is worth noticing that adding a cycle corresponds to adding 2π to the phases.

In two dimensions the problem needs to be addressed in a slightly different way. Because we are now moving in two directions, we need to make sure that our result should not depend on the chosen integration path. In other words we need tho say that the phase field is a conservative vector field where the integration from one point to another point is path independent. A well known property of conservative vector fields is that they are irrotational so that one can calculate the curl of the vector gradient over a closed loop and have as a result zero

$$\nabla \times \nabla\phi = 0, \tag{3.16}$$

where ϕ is our phase field and ∇ is the gradient operator defined as

$$\nabla = \left(\frac{\partial}{\partial x}\mathbf{i} + \frac{\partial}{\partial y}\mathbf{j} \right).$$

The assumption that the field is irrotational means that if we consider four adjacent phase values, the summation of the phase gradients over a close loop is equal to zero, as illustrated in figure 3.8. What stated above is always true for the unwrapped phase field, so that one can say that because the result of the integration does not depend on the chosen path, the unwrapped gradients completely specify the associated field.

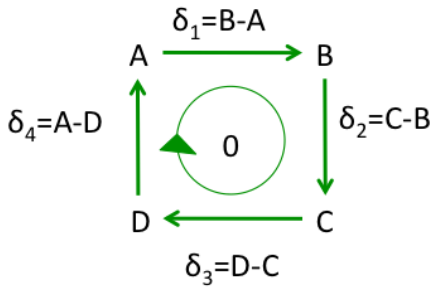

Figure 3.8: Calculation of phase gradients for a set of four adjacent points. Here we assume to move within the points in clock-wise order and to calculate the associated gradients. If $\sum_{i=1}^{4} \delta_i = 0$ the phase field is called irrotational.

Unfortunately this is not the case for the wrapped field, in fact as shown in Figure 3.9, the closed loop integrals of wrapped gradients can give non-zero solutions so that these fields are not conservative [62]. In these cases the curl applied to the gradient field gives as a result a vorticity, or 'residue', whose meaning is that we do not have a unique solution because the obtained result becomes path dependent as shown in Figures 3.9.b-c.

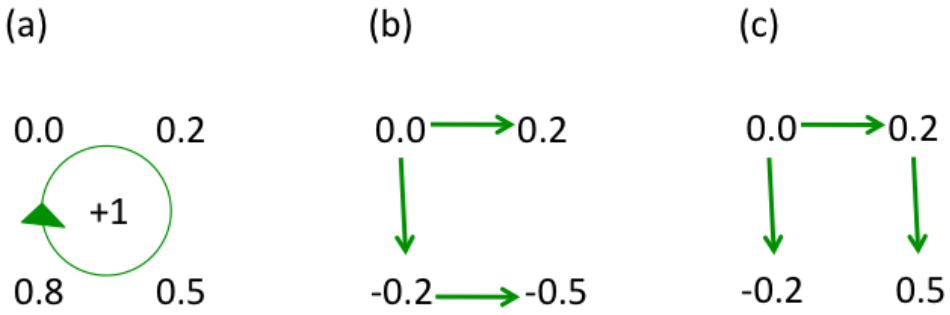

Figure 3.9: 2x2 array of wrapped phase values. (a) The loop integral calculated clockwise starting from value 0.0 gives as a result value $+1$. In this case we calculate $\delta_1 = 0.2 - 0.0 = 0.2$, and similarly we obtain $\delta_2 = 0.3$, $\delta_3 = 0.3$ and $\delta_4 = -0.8$ that violates Nyquist's criterion. In order to unwrap this set of values we should need to add one cycle to 0.0 so that it becomes 1.0 and $\delta_4 = 1 - 0.8 = 0.2$. In this way $\delta_1 + \delta_2 + \delta_3 + \delta_4 = +1$. If we now consider to start from value 0.0 and to recover the unwrapped phases by using the calculated gradients, we can get either (b) or (c), where δ_4 is considered with negative sign. This result shows that when the wrapped phase field is not irrotational, the unwrapped solution is not unique.

The reasons for a non-conservative phase field can for example be undersampling or noise and

where the former can be controlled, while the latter is difficult to eliminate.

Because only one unwrapped solution is the true one, finding a correct unwrapping strategy is a problem of great importance. During the years many approaches have been proposed and among them, Goldstein [62] implemented the branch-cut method in 1988. It is based on calculating the gradients and their respective residues in the way we showed above and it is expected that they can only assume values ± 1 and 0. The sign associated to the calculated residues is of great importance, in fact Goldstein made a clear distinction between positively or negatively charged residues. The core of his method is to introduce branch-cuts to connect positive and negative charges in such a way that a cut is 'charge free'. These cuts serve as a barrier for the integration so that no net residue can be included in the unwrapping process and the spreading of general errors is avoided. Local errors in the immediate vicinity of residues may still occur. Those pixels that are at the opposite edges of a cut will certainly see a phase discontinuity of more than half a cycle, but the goal of the method is to minimize the total length of cuts so to minimize the total discontinuity. In this way the inconsistency of the solution is avoided and a final unique unwrapped field is achieved independent of integration path.

Let us consider the case of a two dimensional field of noisy phase measurements of which Figure 3.10 shows a 4x4 extract. As already mentioned it is possible to calculate the residues of 2x2 pixels sub systems and in this case there is only one point where the residue is $+1$. If we now imagine to move in the complete phase field, we can imagine to place a box of size 3x3 around this residue and to scan the full matrix until another residue is found. When the residue is found, it is connected to the starting one with a line, or cut. If the cut is uncharged, it is considered complete so that the next residue is selected and same steps are repeated. If a residue is not found, the size of the box is increased to 5x5 and same steps are taken.

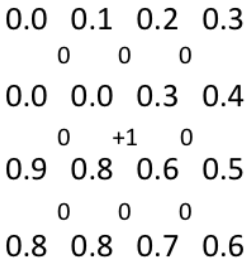

Figure 3.10: 4x4 matrix of wrapped phase values. In the central part we can extract a 2x2 array of residue +1. If this 4x4 system is part of a complete wrapped phase field, we can imagine to center a 3x3 searching box around the +1 residue and to move it around in the complete array to look for other non-zero residues. When one is found, the two are connected by a cut.

In the end, all of the residues lie on cuts which are uncharged, so that no global errors are allowed. Where the residues are sparse, they are connected by cuts as shown in Figure 3.11.b. Where they are very dense as in Figure 3.11.c, whole areas are isolated so that the algorithm "gives up". In this case it is not possible to obtain an optimum solution, however we can get a good approximation over most of the matrix, and where it is not the user is warned by the density of the branch cuts [62].

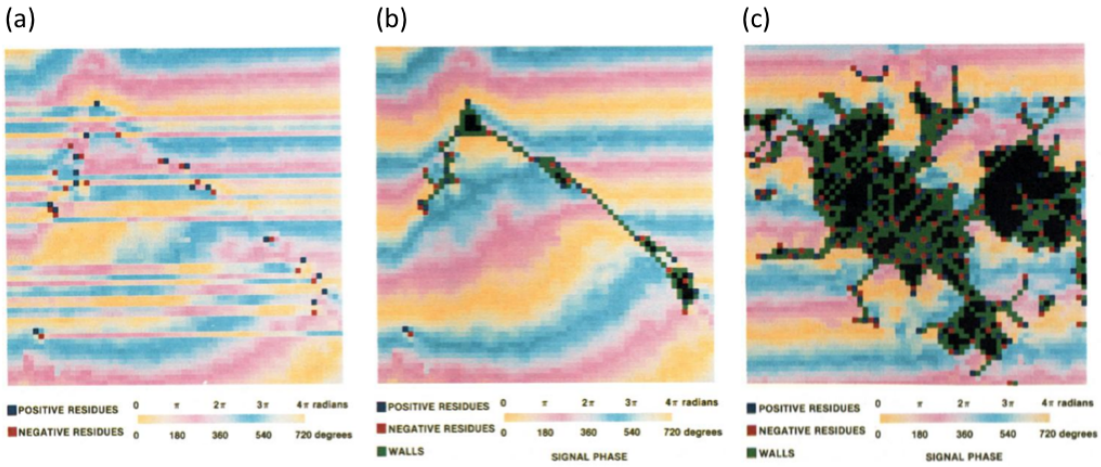

Figure 3.11: Wrapped and unwrapped phase maps. (a) Residues have been calculated by choosing the closest 2π multiple. In this map, two cycles in phase are represented by one revolution of the color bar. (b) Same region of (a) but where cuts are in place before unwrapping, so to avoid global errors. (c) A different region in the phase map showing a high density of residues. The area is entirely isolated from phase estimation because no reliable phase can be calculated in this region. Figures extracted from [62].

A practical approach to use when performing the analysis of experimental data is to discard part of the reconstructed object so to only focus on the area around the sample. The definition of a region of interest is a crucial step because the total field of view of an object reconstruction also includes peripheral areas where the signal to noise ratio is very low. In terms of phase unwrapping we can expect that these areas are going to be extremely problematic and no matter how careful we can be when applying our method, they will generate errors that will propagate to other regions. This is in accordance with what showed in Figure 3.11.c, because if there is a region where the unwrapping algorithm gives up, we can't expect that this is not going to affect the final result in the reconstructed phase. For this reason it is wise to cut the reconstruction defining a proper region of interest before unwrapping the phase, so that we can simplify the algorithm's task and we are sure to obtain a better result.

3.5.2 Phase ramps

While performing the data treatment of the experiments that will be later discussed in this work, we have always faced the phase ramps removal step. In this section the main concepts at the basis of the algorithms used in our data analysis will be presented. However it is worth noticing that the problem of phase ramps removal can be addressed in more elaborate ways whose description is beyond the purpose of this Thesis.

Phase ramps are a recurring problem when treating ptychographic reconstructions and an easy way to understand how they are generated is to consider a simple diffraction experiment. We can think to perform an easy CDI experiment where we illuminate the sample and we collect the resulting diffraction pattern in the far field. From the previous Chapter we know that the relationship between the object and the diffraction pattern is a Fourier transform. We can now think to modify the diffraction pattern and to operate the inverse Fourier transform to go back to the real space and quantify what is the resulting effect. If we decide to shift a whole column of pixels by one position, no matter in which direction, we will see that the real space object will not be well defined anymore because it will show stripes. These stripes are given by the introduction of a phase ramp. If we imagine to extract a line from the object and to plot the phase profile, as shown in Figure 3.12, we will see that the result will indeed not be flat. The amplitude of the phase ramp introduced by a shift of one pixel is 2π.

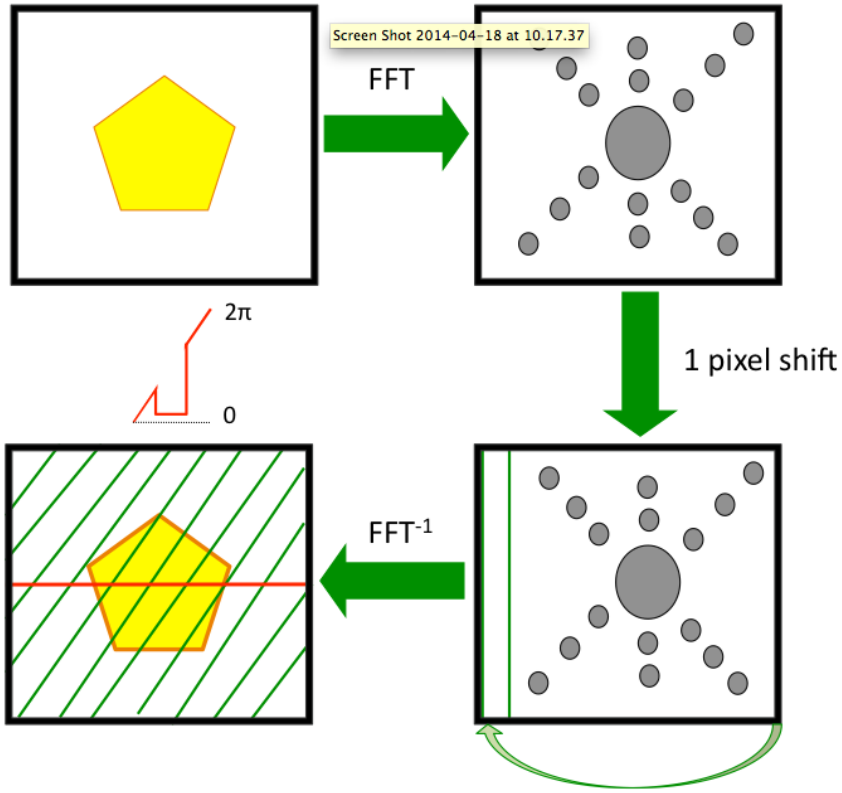

Figure 3.12: Phase ramp introduced by a shift of one pixel. When performing a diffraction experiment, for instance a CDI one, we illuminate the sample and we collect the diffraction pattern in the far field. It is well known that the two objects are linked by a Fourier transform. If we now operate a shift of one pixel in the recorded diffraction pattern, for example by using the circshift function in matlab, and we inverse transform the obtained result, we will see stripes shown here as green lines. In order to estimate the linear phase one can extract a line, here in red, and plot its phase values. The result, illustrated as a red profile, clearly shows that a shift of one pixel in the frequency domain corresponds to the introduction of a phase ramp of amplitude 2π in the object domain.

If we now consider what happens in ptychography we can easily understand that the problem is way more complicated than the one presented above. First of all in ptychography we do not collect a single diffraction pattern but a series of them, so that intuitively one can think how difficult it can be to control shifts. Even assuming that the experiment is perfectly conducted and that there are no drifts, there is another important issue to consider regarding how the exit wave function is generated. By recalling Equation 3.1 we see that the exit wave propagating in the far field ψ is given by the multiplication of two complex quantity being the illumination function, or probe, and the

object function which represents the sample. If we now think that the probe can have a linear phase contribute in the form $\phi = a + bx + cy$, where for simplicity we are considering a two dimensional case, we can say that Equation 3.1 still holds in the form

$$\psi(\mathbf{R}) = P(\mathbf{R})\, e^{i\phi} O(\mathbf{R})\, e^{-i\phi} = P(\mathbf{R})\, O(\mathbf{R}) \tag{3.17}$$

as illustrated in Figure 3.13.

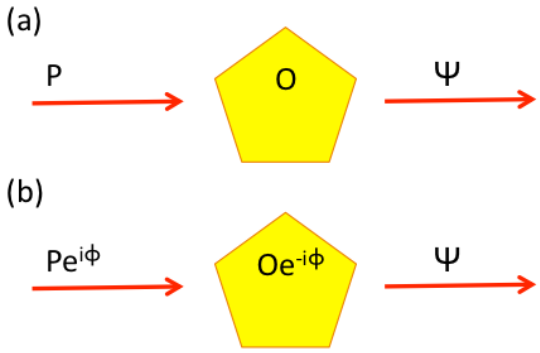

Figure 3.13: Exit wave composition. (a) We assume that the probe function has a flat phase so that we can obtain the exit wave by simply multiplying the probe and object functions. (b) When the probe has a linear phase, ϕ, it introduces a contribute that also affects the object function. In fact, in order to obtain the exit wave in accordance with equation 3.1 we need to write $\psi(\mathbf{R}) = P(\mathbf{R})\, e^{i\phi} O(\mathbf{R})\, e^{-i\phi}$ where $O(\mathbf{R})\, e^{-i\phi}$ is the new object function.

If we now perform our ptychography experiment by translating the probe to a different position (x_0, y_0), this translation will also affect the phase in the form

$$\psi(\mathbf{R}) = P(\mathbf{r}-\mathbf{R})\, e^{i[a+b(x-x_0)+c(y-y_0)]} O(\mathbf{R})\, e^{-i[a+b(x-x_0)+c(y-y_0)]} = P(\mathbf{r}-\mathbf{R})\, O(\mathbf{R}), \tag{3.18}$$

so that the new probe and object functions will include the shift in their phases. When the exit wave will be recovered from the diffraction pattern with the use of an inversion algorithm, the calculated probe and object functions will include this shift and for this reason we will see a phase ramp.

In order to remove the phase ramp we need to find the linear phase parameters a, b and c. A convenient way of proceeding would be to select an empty area in the reconstructed object so to isolate a region where the phase ramp is the most relevant contribute. In order to retrieve the parameters

one can select three points and solve the set of equation

$$\begin{cases} \phi_1 = a + bx_1 + cy_1 \\ \phi_2 = a + bx_2 + cy_2 \\ \phi_3 = a + bx_3 + cy_3 \end{cases} \tag{3.19}$$

where the three points have coordinates $A = (x_1, y_1)$, $B = (x_2, y_2)$ and $C = (x_3, y_3)$ as illustrated in Figure 3.14.c. This system of three equations and three unknowns is easily solvable, but the mistake lies in the fact that if we choose a region of n pixels to estimate the phase ramp, the obtained result will be different for each set of three-points.

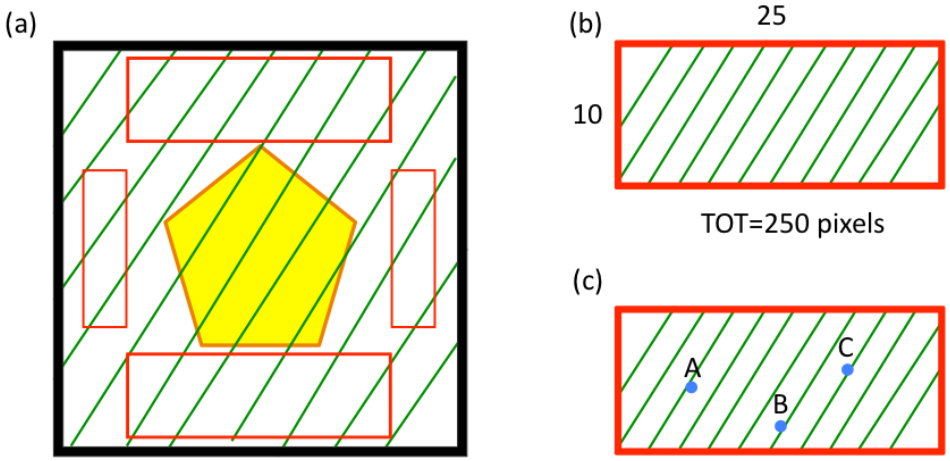

Figure 3.14: Phase ramp removal. (a) In order to remove the phase it is necessary to draw masks in the reconstructed object so to select empty space areas where the phase is the most relevant contribute. (b) The masks can have a different size and the phase values contained in each pixels are used to quantify the linear phase parameters. (c) Because the linear phase is specified by three parameters, one can think to solve the problem by only selecting a set of three points, but as explained in the text this procedure does not give a correct solution.

In order to correctly address this problem we need to consider all points in the region so that we

can solve the system

$$\begin{bmatrix} \phi_1 \\ . \\ . \\ \phi_n \end{bmatrix}_{1\times n} = \begin{bmatrix} 1 & x_1 & y_1 \\ . & . & . \\ . & . & . \\ 1 & x_n & y_n \end{bmatrix}_{n\times 3} \cdot \begin{bmatrix} a \\ b \\ c \end{bmatrix}_{3\times 1} \tag{3.20}$$

$$\Phi = T \cdot P$$

which is overdetermined because the number of equations is bigger than the number of unknowns. In the case where the number of equations is the same as the number of unknowns, the solution of the problem would simply be

$$\begin{aligned} T^{-1} \cdot \Phi &= T \cdot T^{-1} \cdot P \\ T^{-1} \cdot \Phi &= I \cdot P \\ T^{-1} \cdot \Phi &= P \end{aligned} \quad , \tag{3.21}$$

where I is the identity matrix and T^{-1} is the inverse of matrix T. Our case is different and in particular, because T is not a square matrix, we can't operate the inverse operation so that there is no way that we can directly obtain the parameters vector P. In order to solve our problem we can instead calculate the Moore-Penrose pseudoinverse matrix of T

$$T^* = \left(T^T \cdot T\right)^{-1} \cdot T^T \tag{3.22}$$

where T^T is the transpose of matrix T. The pseudoinverse has many similarities with the inverse matrix, but one particular difference between the two is that commutivity is not guaranteed so that

$$T^* \cdot T = I \tag{3.23}$$

but

$$T \cdot T^* \neq I. \tag{3.24}$$

We can now apply matrix T^* to Equation 3.20 so to obtain

$$\begin{aligned} T^* \cdot \Phi &= T^* \cdot T \cdot P \\ T^* \cdot \Phi &\approx I \cdot P \\ T^* \cdot \Phi &\approx P, \end{aligned} \tag{3.25}$$

where exact equality is not guaranteed because the pseudoinverse operates a least square fit of the data. Once the system is solved and the linear phase $\phi = a + bx + cy$ is fully determined, the last step is to multiply the complex reconstructed object by the complex conjugate phase

$$O(\mathbf{R}) = O(\mathbf{R})\, e^{i(a+bx+cy)} e^{-i(a+bx+cy)} \tag{3.26}$$

so that the phase ramp can be corrected.

Chapter 4

Diffraction of X-rays by crystals

4.1 Introduction to X-ray Crystallography

In the early years of the 20th century many discoveries were made in the Crystallography field. It was back in 1912 that everything started when von Laue realized that a crystal could have been used as a diffraction grating for X-rays. He performed an experiment where he used a flux of X-rays to illuminate a copper sulfate crystal to then record the resulting diffraction pattern on photographic plates in the far field. The result showed diffraction spots surrounding the central spot given by the primary beam. This effect was explained by von Laue by saying that the spots present in the diffraction pattern originated by X-rays hitting a regular array of atoms which acted as scatterers. In particular he went on explaining that whenever the incoming beam hit an atom, a sherical wave was produced. Because this process happened for many atoms at the same time, as a result there was the generation of a regular array of spherical waves which could interfere destructively or constructively, being the latter the cause for the bright spots on the photographic plate. Von Laue's experimental demonstration of X-rays diffraction showed the wave nature of X-rays and his results gave new imputs to this part of physics which at the time was mostly used to study the morphology of minerals.

After a short time William Lawrence Bragg used those new theories to solve the first crystal structure and stated that the rule to apply in retrieving the diffraction pattern was

$$2dsin\theta = n\lambda \tag{4.1}$$

where d is the spacing between two contiguous diffracting planes, ϑ is the incident angle, n is any integer, and λ is the wavelength of the beam [63].

The discoveries gave evidence of the fact that X-rays are electromagnetic waves, whose wavelength is in the region of angstrom units, and that the internal structure of crystals is regular in the three dimensions with spacings of the same order. Nowadays Crystallography has become an extremely important discipline at the basis of many branches of Science, from Physics to Chemistry and Biology. Thanks to the new discoveries and advancements in this field, we can not only study but even produce new materials with specific properties that can be designed for many different uses.

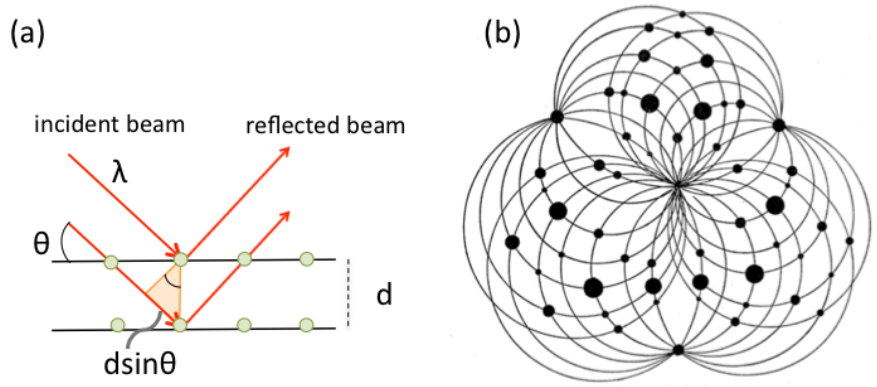

Figure 4.1: (a) Schematic representation of Bragg's law. The incident X-ray beam produces a Bragg peak if the reflections off the various planes interfere constructively (the phase shift between two beams is 2π). In other terms, the path difference between the waves hitting different planes must be multiple of the wavelength λ as shown in Equation 4.1. (b) Rock-salt crystal structure obtained by Bragg in 1913 [63].

4.2 Kinematical diffraction

The first formulation of kinematical diffraction was provided by von Laue in first papers on X-ray scattering. In this section a simplified version of this theory will be presented through the use of several initial assumptions following the approach used by [64]. The model under consideration is represented by a traveling plane wave (the X-ray beam) that interacts with an extended crystal so to generate a diffraction pattern that will be collected in the far field (Fraunhofer diffraction). Therefore we will assume that the source-object and the object-detector distances are much greater than the

distances separating the various scatterers (atoms) in the crystal. We will also assume that both the incident and scattered beams can be illustrated by a flux of parallel waves with no divergence. In this approximation we will consider that the interference between scattered beams emerging from atoms at different positions can be represented by superposition of waves traveling with different paths. In the end we will neglect the condition of multiple scattering inside the crystal and we will assume that all the scattered beams are generated by elastic scattering, so that it will be possible to use the conservation of energy.

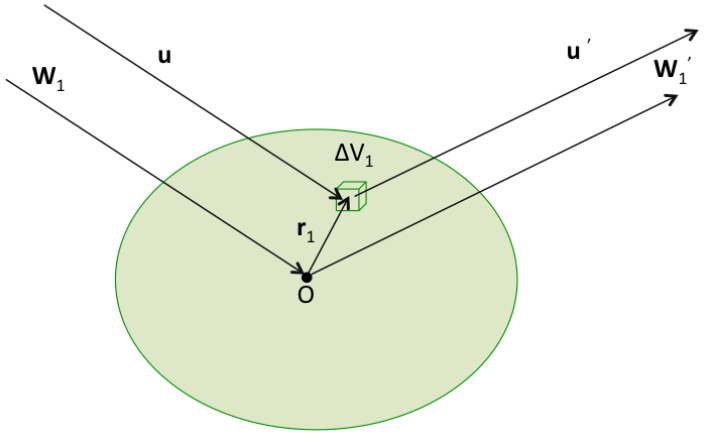

Figure 4.2: Schematic representation of the model used to explain the kinematic theory of diffraction. An extended crystal of origin O is hit by a plane wave $\mathbf{W}_1$ traveling along the direction specified by the unit vector $\mathbf{u}$. The diffracted beam $\mathbf{W}_1^{'}$ is then scattered in the direction specified by the unit vector $\mathbf{u}^{'}$. A generic diffracting unit is represented by ΔV_1 and its distance from the origin is given by vector $\mathbf{r}_1$. Figure adapted from [64].

By considering the model shown in Figure 4.2 it is possible to state that if an incoming beam, represented by a plane wave traveling along $\mathbf{u}$, interacts with a specimen, in this case an extended crystal, it generates a scattered beam that travels along the direction given by the unit vector $\mathbf{u}^{'}$. If we now consider that the extended sample can be divided into volume units ΔV, we can say that waves scattered from different increments of volume will interfere with each other, or in other terms, their instantaneous amplitudes will be additive [64]. For this reason we can say that the total scattered wave along direction $\mathbf{u}^{'}$ is given by a sum of components scattered from the each volume element. In order to better understand the interaction between the different scattered beams, it is possible to observe

that the phase difference between two waves scattered from different volume units is strictly related to their the path difference. For example if $\mathbf{r}_1$ is the vector that connects two scattering units, in our case the origin of the crystal, point O, and the volume unit element ΔV_1, we can show that the path difference between two rays scattered from these two points is

$$\Delta r_1 = \mathbf{r}_1 \cdot \mathbf{u} - \mathbf{r}_1 \cdot \mathbf{u}^{'} = \mathbf{r_1} \cdot \left(\mathbf{u} - \mathbf{u}^{'}\right). \tag{4.2}$$

Under this condition, the phase shift between the two scattered waves can be related to the path difference by assuming that a difference in the path equal to λ corresponds to a phase difference $\Delta\phi = 2\pi$ radians

$$\frac{\Delta\phi}{2\pi} = \frac{\Delta r_1}{\lambda}. \tag{4.3}$$

It is now possible to generalize the phase shift due to the scattering of the jth element of volume ΔV_j relative to the phase of the wave scattered from the center of the crystal by writing

$$\Delta\phi_j = \frac{2\pi\Delta r_j}{\lambda} = \frac{2\pi\mathbf{r}_j \cdot \left(\mathbf{u} - \mathbf{u}^{'}\right)}{\lambda}. \tag{4.4}$$

The quantity expressed in brackets in equation 4.4 can be related to the scattering vector $\mathbf{q}$ defined in Chapter 2. In order to unify the notations that we have been using so far we can write the scattering vector $\mathbf{q}$ as

$$\mathbf{q} = \mathbf{2}\pi\frac{\mathbf{u} - \mathbf{u}^{'}}{\lambda} \tag{4.5}$$

where $\mathbf{u}/\lambda$ and $\mathbf{u}'/\lambda$ represent the incident and diffracted beam direction unit vectors normalized against the wavelength as shown in Figure 4.3[1].

[1]Equation 4.5 is the same as $\mathbf{q} = \mathbf{k} - \mathbf{k}'$ where $\mathbf{k}$ is the wavevector of the incoming beam.

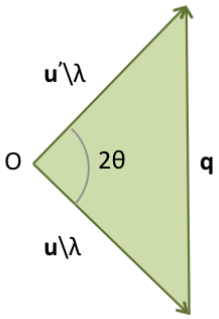

Figure 4.3: The scattering vector $\mathbf{q}$ is defined as the difference of the two vectors $\mathbf{u}\backslash\lambda$ and $\mathbf{u}^{'}\backslash\lambda$ .The diffraction angle 2θ is also defined by the incoming and scattering vectors. Figure adapted from [64].

By following our initial assumptions, the phase of the generic jth scattered radiation is then expressed by a plane wave in the form of $e^{i\phi_j}$, and the resultant total amplitude is obtained by

$$A = \sum_j f_j e^{2\pi i \mathbf{q}\cdot\mathbf{r}_j} \tag{4.6}$$

where f_j represents the scattering power of the jth scattering element. In order to better understand the meaning of this quantity we can consider that the scattering of X-rays from atoms is predominantly from the electrons within the atom itself. Because electrons in atoms are commonly described with a wavefunction that satisfies the Schrodinger equation, the scattering power for X-rays from an atom can be expressed as a function of the scattering vector $\mathbf{q}$ by an integration over the entire volume of the atom of all waves scattered from these electrons[2] as

$$f(\mathbf{q}) = \int_{atom} \rho(\mathbf{r})\, e^{2\pi i \mathbf{q}\cdot\mathbf{r}} dV_r \tag{4.7}$$

where $\rho(\mathbf{r})$ represents the electron density function and dV_r is the volume increment.

[2]The intensity scattered from a single electron is commonly known as Thomson scattering per electron

$$I_c = \frac{I_0 e_4}{m^2 r^2 c^4}\left(\frac{1+cos^2(2\theta)}{2}\right)$$

where I_0 is the incident beam flux, e is the electron charge, m is the electron mass, c is the speed of light, r is the electron-detector distance and 2θ is the scattering angle. The quantity in brackets represents the polarization factor [19].

Given the amplitude in Equation 4.6, we can derive the scattered intensity $I(\mathbf{q})$ as

$$I(\mathbf{q}) = AA^* = \left| \sum_j f_j e^{2\pi i \mathbf{q}\cdot\mathbf{r}_j} \right|^2 \tag{4.8}$$

which is expressed in absolute units, commonly known as electron units.

In order to further develop this formulation it is now necessary to take the crystalline structure of the specimen into account.

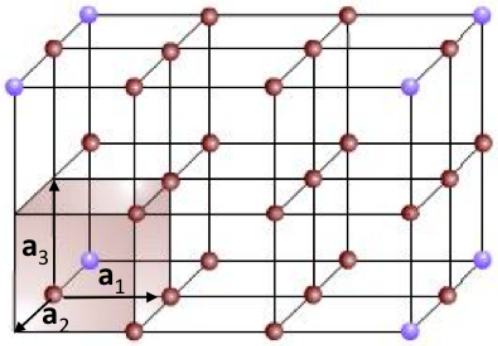

Figure 4.4: The Bravais lattice is an infinite array of discrete points which are regulargly spaced in the three dimentions. The smallest part of a crystal is commonly referred to as primitive unit cell and here it is shown in red. The whole crystal structure can therefore be decomposed into a repetition of unit cells. In the three dimesions unit cells are described trough lattice vectors $\mathbf{a}_1$, $\mathbf{a}_2$ and $\mathbf{a}_3$. Figure adapted from [65].

By dividing the crystal into primitive unit cells of lattice vectors $\mathbf{a}_1$, $\mathbf{a}_2$ and $\mathbf{a}_3$, we can also divide the summation in equation 4.8 into two parts: one is the summation over a single unit cell while the other is a summation over all the unit cells in the diffracting volume

$$I(\mathbf{q}) = \left| \sum_j^{u.c.} f_j e^{2\pi i \mathbf{q}\cdot\mathbf{r}_j} \right|^2 \left| \sum_n f_j e^{2\pi i \mathbf{q}\cdot\mathbf{r}_n} \right|^2 = |F(\mathbf{q})|^2 |G(\mathbf{q})|^2 . \tag{4.9}$$

The first term is commonly known as structure factor, $F(\mathbf{q})$, and is a summation of all the scattering contributions within one unit cell. The other term defines the interference function, $G(\mathbf{q})$, which is a Fourier transformation of the real space point lattice [64]. The vector $\mathbf{r}_n$ that appears in the

interference function is related to the unit cell lattice vectors as

$$\mathbf{r}_n = n_1\mathbf{a}_1 + n_2\mathbf{a}_2 + n_3\mathbf{a}_3 \tag{4.10}$$

and its function is to connect the origin O of the crystal to the nth lattice point, being n_1, n_2 and n_3 integer numbers. If we now take this into account, we can expand the interference function formula by replacing the single summation with a triple one over n_1, n_2 and n_3

$$|G(\mathbf{q})|^2 = \left|\sum_{n_1}^{N_1} e^{2\pi i\mathbf{q}\cdot n_1\mathbf{a_1}}\right|^2 \left|\sum_{n_2}^{N_2} e^{2\pi i\mathbf{q}\cdot n_2\mathbf{a}_2}\right|^2 \left|\sum_{n_3}^{N_3} e^{2\pi i\mathbf{q}\cdot n_3\mathbf{a}_3}\right|^2 \tag{4.11}$$

where N_1, N_2 and N_3 are numbers of unit cells along the three lattice vector directions. If we consider a large number of unit cells and we evaluate each of the three terms by the formula of the geometric sum[3], we obtain

$$|G(\mathbf{q})|^2 = \frac{sin^2\left(\pi\mathbf{q}\cdot N_1\mathbf{a}_1/2\right)}{sin^2\left(\pi\mathbf{q}\cdot\mathbf{a}_1\right)} \frac{sin^2\left(\pi\mathbf{q}\cdot N_2\mathbf{a}_2/2\right)}{sin^2\left(\pi\mathbf{q}\cdot\mathbf{a}_2\right)} \frac{sin^2\left(\pi\mathbf{q}\cdot N_3\mathbf{a}_3/2\right)}{sin^2\left(\pi\mathbf{q}\cdot\mathbf{a}_3\right)}. \tag{4.12}$$

It is worth noticing that when the number of cells approaches infinity, the interference function can be written as

$$|G(\mathbf{q})| = N_1N_2N_3 = N_v \tag{4.13}$$

where N_v is the total number of unit cells in the diffracting volume. This can be explained if we remember that each term in Equation 4.12 is periodic as shown in Figure 4.5. It is noted that if we increase the value of N_i, the peak becomes sharper and its height equals ${N_i}^2$. When N_i tends to infinity, the interference function becomes a delta function with amplitude N_i.

[3]It is possible to apply the substitution $\sum_{n=0}^{N-1} e^{2\pi i\mathbf{q}\cdot n\mathbf{a}} = \frac{1-e^{i2\pi qNa}}{1-e^{i2\pi qa}}$ for each term and then through easy algebric steps one can obtain Equation 4.12.

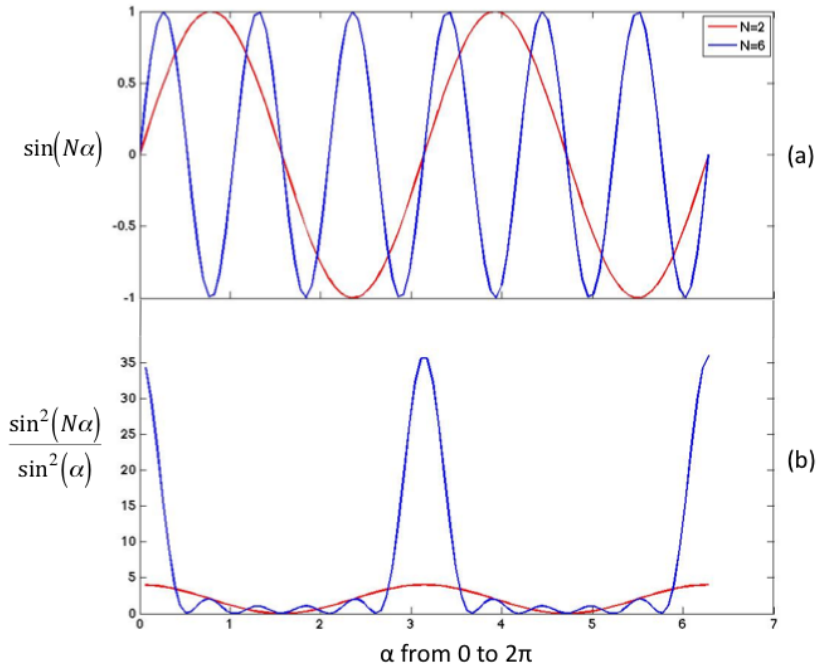

Figure 4.5: Schematic representation of the interference function for two values of N. It is worth noticing that the amplitude of the function in (b) equals N^2 while the peak's width is proportional to 1/N, where N is the number of unit cells contributing to diffraction.

If we want to maximize the diffracted intensity we need to impose the equalities

$$\begin{cases} \frac{\mathbf{q}\cdot N_1\mathbf{a}_1}{2} = \frac{\pi}{2}h \\ \frac{\mathbf{q}\cdot N_1\mathbf{a}_2}{2} = \frac{\pi}{2}k \\ \frac{\mathbf{q}\cdot N_1\mathbf{a}_3}{2} = \frac{\pi}{2}l \end{cases} \tag{4.14}$$

that are widely known as Laue conditions and where the integers h, k, l may adopt any value between $-\infty$ and $+\infty$. The Laue conditions show that scattering can be described by sets of planes spaced $h/\mathbf{a}_1$, $k/\mathbf{a}_2$, and $l/\mathbf{a}_3$ apart and perpendicular to $\mathbf{a}_1$, $\mathbf{a}_2$, and $\mathbf{a}_3$, respectively [19]. In three dimensions, the Laue conditions define what is commonly known as reciprocal lattice.

The reciprocal lattice is a construction with vast importance for condensed matter physics. Starting with a Bravais lattice, the reciprocal lattice is the set of all wave vectors $\mathbf{g}$ that give plane waves $e^{i\mathbf{g}\cdot\mathbf{r}}$

with the periodicity of the Bravais lattice[4]. If as mentioned above, $\mathbf{a}_1$, $\mathbf{a}_2$, and $\mathbf{a}_3$ are the primitive vectors of the direct lattice, the reciprocal lattice is described by the corresponding primitive vectors

$$\begin{cases} \mathbf{b}_1 = 2\pi \frac{\mathbf{a}_2 \times \mathbf{a}_3}{\mathbf{a}_1 \cdot (\mathbf{a}_2 \times \mathbf{a}_3)} \\ \\ \mathbf{b}_2 = 2\pi \frac{\mathbf{a}_1 \times \mathbf{a}_3}{\mathbf{a}_1 \cdot (\mathbf{a}_2 \times \mathbf{a}_3)} \\ \\ \mathbf{b}_3 = 2\pi \frac{\mathbf{a}_1 \times \mathbf{a}_2}{\mathbf{a}_1 \cdot (\mathbf{a}_2 \times \mathbf{a}_3)} \end{cases} \tag{4.15}$$

which corresponds to

$$\mathbf{b}_i \cdot \mathbf{a}_j = 2\pi \delta_{ij} \tag{4.16}$$

where δ_{ij} is the Kronecker delta function, defined as

$$\delta_{ij=} \begin{cases} 1 \quad for \quad i = j \\ \\ 0 \quad for \quad i \neq j. \end{cases} \tag{4.17}$$

At this point we can define the reciprocal space vector $\mathbf{g}$ as

$$\mathbf{g} = h\mathbf{b}_1 + k\mathbf{b}_2 + l\mathbf{b}_3 \tag{4.18}$$

where h, k and l are integers that identify a given family of crystallographic planes. In scientific literature these integers are commonly known as Miller indices. Each index represents a plane orthogonal to a direction (hkl) in the basis of the reciprocal lattice vectors. The magnitude of the reciprocal space vector $\mathbf{g}$ results equal to $1/d_{hkl}$ in the direct space where

$$d_{hkl} = \frac{a}{\sqrt{h^2 + k^2 + l^2}}, \tag{4.19}$$

being a is the lattice constant.

[4] r is a vector depicting a point in a Bravais lattice.

One can show that vector **g** satisfies the three Laue conditions of Equation 4.14 [19], so that the interference function only assumes significant values when

$$\mathbf{q} = \mathbf{g}, \tag{4.20}$$

which is the vector form of Bragg's law. If the scattering vector **q** matches one of the reciprocal space lattice vectors **g**, we will have constructive interference (Bragg diffraction). After recalling equation 4.9, we can conclude that when Bragg's law is met, the diffracted intensity becomes

$$I(\mathbf{q}) = N_v \left|F(\mathbf{q})\right|.^2 \tag{4.21}$$

At this point it is possible to highlight the role covered by the structure factor $F(\mathbf{q})$. It is worth noticing that the structure function can be rewritten for a given hkl reflection as

$$F(hkl) = \sum_j^N f_j e^{2\pi i(hx_j + ky_j + lz_j)} \tag{4.22}$$

where we consider that a single unit cell contains a set of N atoms, with coordinates x_j, y_j, and z_j for the ith atom in the unit cell. In the case the single unit cell only contains one atom of coordinates $(xyz) = (000)$, the structure factor becomes $F = f$. If we instead consider a body-centered cell with two atoms of coordinates (000) and $\left(\frac{1}{2}\frac{1}{2}\frac{1}{2}\right)$, the structure function becomes

$$F = f\left(1 + e^{i\pi(h+k+l)}\right) = \begin{cases} 2f & when \quad (h+k+l) = 2n \\ \\ 0 & when \quad (h+k+l) = 2n+1, \end{cases}$$

where n is any positive integer. The above are only two examples of structure function calculations, but a similar approach can be used for different geometries.

4.2.1 The Ewald sphere

Before discussing the dynamical theory of diffraction it is worth examining a very useful tool that makes it easier to visualize diffraction events in reciprocal space. In order to do that it is also important to

understand the relationship between the real space lattice and the reciprocal space one described by Equation 4.18. It can be easily shown that the reciprocal lattice can be derived by operating a Fourier transform of the real space lattice.

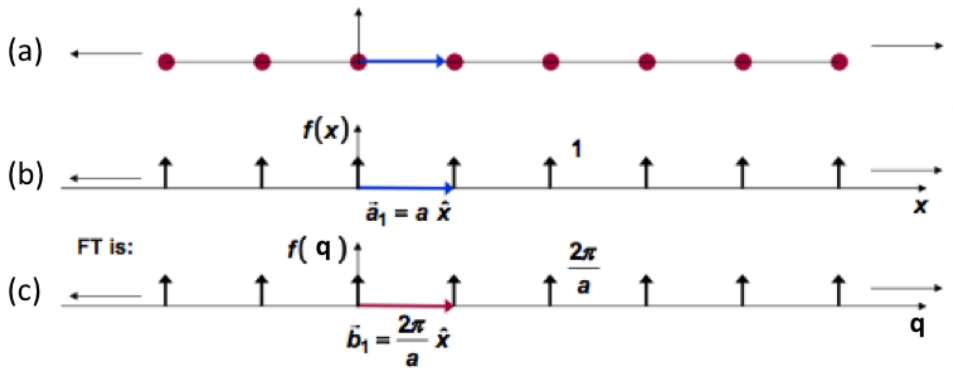

Figure 4.6: Real space and reciprocal space lattices. (a) The real space 1D Bravais lattice is described by a series of equally spaced dots. (b) The lattice function associated to the real space is a comb function where the delta functions have amplitude 1 and the spacing is given by the lattice constant a. (c) The reciprocal space lattice is obtained by operating the Fourier transform of the real space lattice. The reciprocal lattice function is again a comb function where the amplitude and the spacing of the delta functions is $b_1 = 2\pi/a_1$. Figure adapted from [66].

If we consider the case of a 1D lattice shown in Figure 4.6 we can write the real space lattice function as a comb

$$L(x) = comb(x) = \sum_{n=-\infty}^{\infty} \delta(x - na) \tag{4.23}$$

where a is the lattice constant. If we now operate the Fourier transform, we obtain

$$L(\mathrm{q}) = \int_R \sum_n \delta(x - na)\, e^{i2\pi qx} dx = \sum_{n=-\infty}^{\infty} e^{i2\pi qna} \tag{4.24}$$

where

$$\sum_{n=-\infty}^{\infty} e^{i2\pi qna} = \begin{cases} \infty & for \quad q = \frac{n}{a} \\ \\ 0 & elsewhere \end{cases} \tag{4.25}$$

which in fact corresponds to the comb function

$$L(q) = b_1 \sum_{m=-\infty}^{\infty} \delta(q - mb_1) \tag{4.26}$$

where $b_1 = 2\pi/a$. At this point we can extend this result to the 3D case by just remembering equations 4.15 and 4.18. In this case we can say that the 3D reciprocal lattice is generated by integer coordinates (h, k, l) of the reciprocal basis vectors ($\mathbf{b}_1$, $\mathbf{b}_2$, $\mathbf{b}_3$).

Let us now consider the 2D case where the lattice points are given by $\mathbf{g} = h\mathbf{b}_1 + k\mathbf{b}_2$. In the case $h = 1$ and $k = 2$, the resulting $\mathbf{g}_{hk}$ vector is the one shown in figure 4.7(a). We can now define a circle where a monochromatic incident radiation $\mathbf{k} = AO$ can be scattered to any wave vector $\mathbf{k}' = AB$ terminating on the circle of radius k, as presented in Figure 4.7.b. The Ewald circle is obtained in Figure 4.7.c, where vector $\mathbf{k}$ is on the origin of the reciprocal lattice, that is when a point in the reciprocal lattice overlaps with point O in the circle. It is worth noticing that the scattering vector $\mathbf{q}$ is a chord in the Ewald circle and as previously mentioned is obtained from the incident and scattered wave vectors.

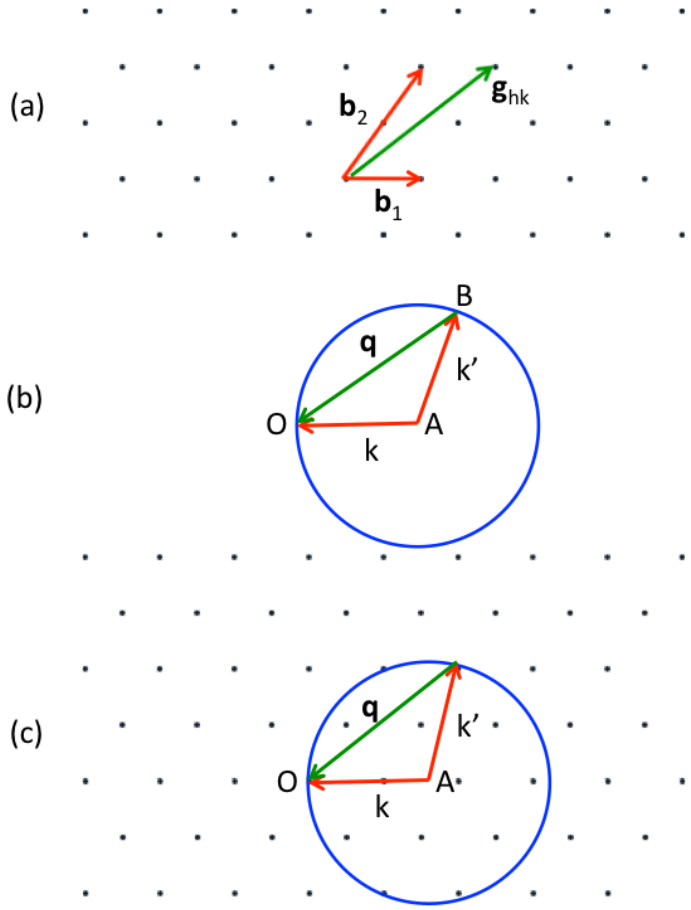

Figure 4.7: Construction of the 2D Ewald circle. (a) A reciprocal lattice is shown for points given by $\mathbf{g} = h\mathbf{b}_1 + k\mathbf{b}_2$, with $h = 1$ and $k = 2$. (b) We define a circle of radius k=AO where $\mathbf{k}$ represents the incoming wave vector. The scattered wave is also represented by vector $\mathbf{k}'$ which in this case has equal modulus of $\mathbf{k}$. The scattering vector $\mathbf{q}$ is once again given by $\mathbf{q} = \mathbf{k} - \mathbf{k}'$ and is represented by a chord in the circle. (c) By superimposing (a) and (b) we obtain the Ewald circle, where point O is the reciprocal lattice origin.

As shown in Figure 4.7.c, if any reciprocal lattice point falls on the circle, then the Laue condition of Equation 4.20 is fulfilled. If we now position a detector in the direction of the corresponding $\mathbf{k}'$ vector, we can observe a diffraction peak. If two or more reciprocal lattice points fall on the Ewald circle, we have the condition of multiple scattering as shown in Figure 4.8.

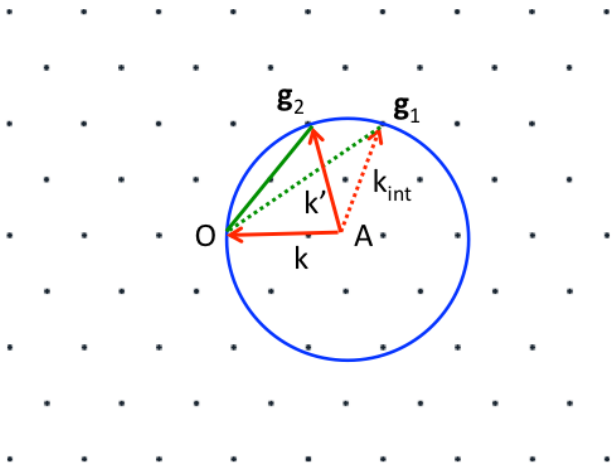

Figure 4.8: Multiple scattering in the Ewald circle.

If for example we only want to consider the $\mathbf{g}_2$ reflection, we can rotate the crystal and the detector so to maximize the corresponding peak along the $\mathbf{k}^{'}$ direction. Even in this case we will have additional contributions given by $\mathbf{g}_1$. In fact because $\mathbf{g}_1$ is on the circle, the incident beam will also be scattered to $\mathrm{k_{int}}$. This means that inside the crystal $\mathbf{k}_{int}$ is scattered to $\mathbf{k}^{'}$ by the reflection $\mathbf{g}_2 - \mathbf{g}_1$, so that an additional intensity may appear along the $\mathbf{k}^{'}$ direction.

It is worth noticing that the thickness of the Ewald circle, blue line in figures 4.7 and 4.8, is related to the bandwidth of the incident radiation Δk. In the case of a white beam, all reflections will be observed within the circles of radius equal to the maximum and minimum $\mathbf{k}$ vector in the beam, as shown below in Figure 4.9. All the reciprocal lattice points in the white area enclosed by the bigger circle will reflect simultaneously [19].

Similar results can be obtained when considering the three dimensional case of the Ewald sphere.

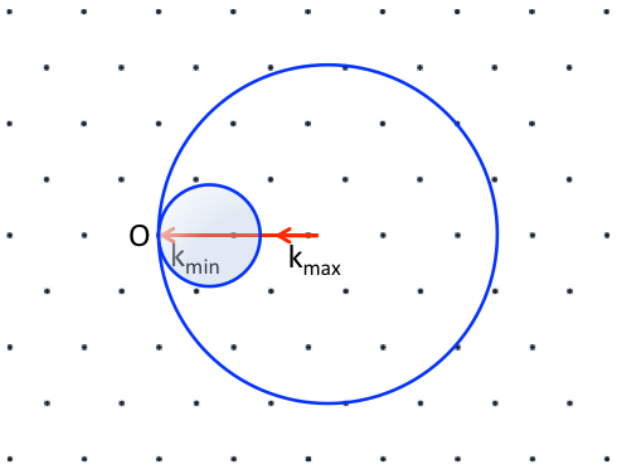

Figure 4.9: Ewald circle for a beam containing wave vectors from $k_{min}$to k_{max}.

4.3 Dynamical diffraction

The theory that has been developed so far is based on the underlying assumption that each individual diffraction event inside the crystal acts independently. Away from this simplicity it is easy to show that many complications can occur. For example we can note that if an X-ray beam is incident at an angle θ that satisfies Bragg's law, it will be reflected at the angle θ to these planes as shown in Figure 4.10.a. It then follows that the diffracted ray will continue to satisfy Bragg's law and therefore is at the correct Bragg angle to diffract a second time (point 2 in Figure 4.10.a) so that it can travel in the direction of the original incident beam; similarly it remains available for diffraction a third time (point 3), back into the first diffraction direction, and so on. If we now suppose that the whole crystal is perfect and is illuminated with X-rays which are subject to multiple diffraction throughout the crystal, we can assume that all of these waves will then interfere with each other as shown in Figure 4.10.b. This process was described by Ewald during the early part of the 20th century [67]. Its theory, in which the diffraction is so strong that it affects the intensity of the primary beam, is referred to as dynamical regime.

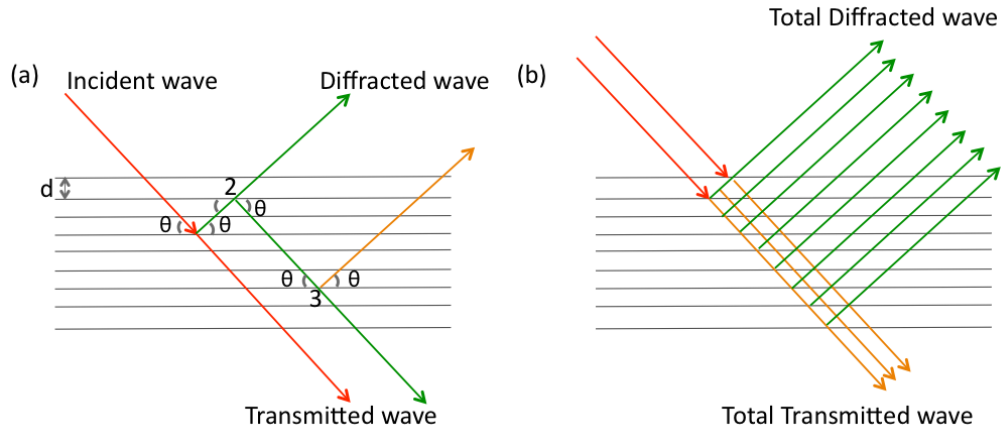

Figure 4.10: Dynamical diffraction schematic representation. (a) The incident beam interacts with the specimen at different crystallographic planes. The diffracted beam is composed by waves diffracted from different loci inside the crystal. (b) Schematic representation of the diffracted beam obtained when scattering from all planes is taken into account.

What is stated above let us understand that the assumptions made to develop the kinematical model can only be applicable if the diffracting crystal is so thin that dynamical effects do not have enough space to occur. In practice it is necessary to highlight the fact that a real crystal does not have a perfect periodic structure as we have assumed so far. It is commonly stated that crystals have mosaic structures where we can identify small ideal crystal grains which have different orientations. It is reasonable to state that the size of each grain is small enough so that internal scattering can be neglected. In this case we can say that the kinematical diffraction theory fully applies within each grain. If we now consider the case of an X-ray beam illuminating an extended crystal, we can say that due to its mosaic structure only a limited number of grains will have the correct orientation to meet the Bragg condition. For this reason dynamical diffraction effects can only be observed for nearly perfect crystals, so that the mosaic grains orientations are distributed within a narrow set of values. In this case it is likely that when illuminated by an incoming X-ray beam, a large number of grains inside the crystal will meet the Bragg condition simultaneously, so to generate internal multiple scattering events.

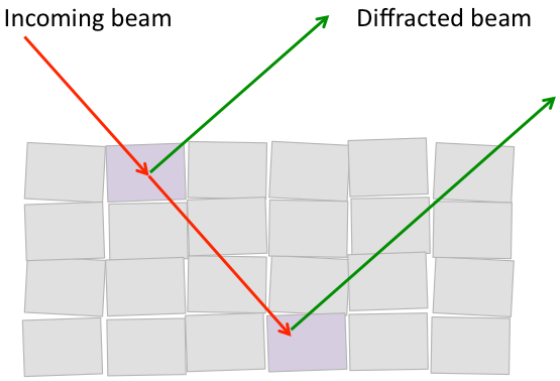

Figure 4.11: Mosaic grains in a crystal. Real crystals present a mosaic structure composed by single blocks, or grains, that can be considered ideal crystals. The blocks have different orientations and when an incoming beam illuminates the crystal, only few blocks will meet the Bragg condition for a given (hkl) reflection. In this case we consider that only two blocks have the correct orientation, so it means that the diffracted beams originated from them will not interact with other blocks so that multiple scattering is avoided. For simplicity this drawing does not show the different crystallographic planes within each box, but if we take them into account, we can say that each plane in the two boxes will generate a diffracted beam, but again, these beams will not interact with other blocks in the crystal.

A well known effect related to dynamical diffraction is the Borrmann effect or *anomalous transmission.* It was shown that the intensities of the transmitted beams are different when considering thin and thick crystals. If we imagine to vary the angle of incidence of an X-ray beam hitting a thin crystal, we can easily see that there will be a drop in the transmitted beam in correspondence of the Bragg angle, as shown below in Figure 4.12.c. This can be easily explained if we remember that we need to take the conservation of energy into account, therefore, the generation of a diffracted beam at the Bragg condition, will consequently affect the transmitted wave by lowering its intensity. The Borrmann effect happens when repeating the same experiment for thick crystals. In this case when meeting the Bragg condition, the transmitted intensity shows a peak this apparently violating the conservation of energy. In a very first attempt to explain this effect we can say that part of the incoming beam travels inside the crystal along the crystallographic planes and emerges on the exit surface. This *forward diffracted* beam is generated by the fact that there is some mechanism operating inside the crystal that extinguishes the normal photoelectric absorption so that we see a peak in the transmitted intensity instead of the expected dip [68].

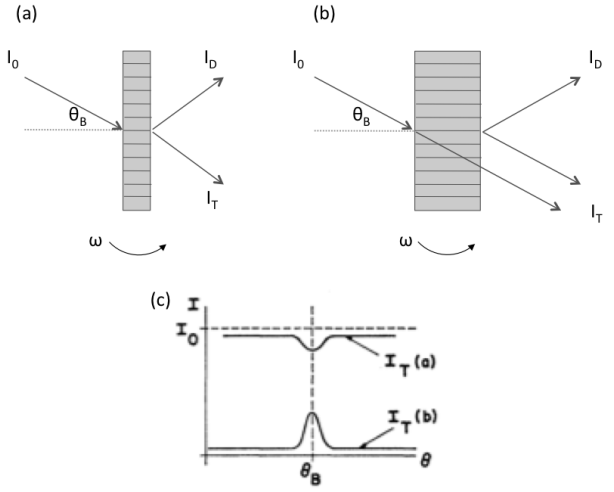

Figure 4.12: Anomalous transmission schematic. A thin (a) and a thick (b) crystals are illuminated in the Laue geometry. (c) Transmitted intensity for the thin and thick crystals versus the rocking angle. When the Bragg condition is met we observe a drop in the transmitted beam for the thin crystal and a peak for the thick one. It is worth noticing that in both cases the intensity of the transmitted wave is lower than the incoming one. This is can be explained by taking photoelectric absorption into account and remembering that $I_t = I_0 e^{-\mu_0 t}$ where μ_0 is the absorption coefficient an t is the thickness of the crystal. We can assume that in case (a) $\mu_0 t \ll 1$, while in case (b) $\mu_0 t > 10$. Figure adapted from [68].

4.3.1 Description of the crystallographic structure

In order to give a more formal description to the Borrmann effect and more in general to dynamical diffraction effects, we need to describe the crystal as a periodic dielectric constant. This can be done by including this information in the definition of the structure factor.

By recalling what stated in the previous sections, we can write the structure factor for the (hkl) reflection, given the reciprocal lattice vector $H = h\mathbf{b}_1 + k\mathbf{b}_2 + l\mathbf{b}_3$ as

$$F_H = \int_V \rho(\mathbf{r})\, e^{(i2\pi \mathbf{H}\cdot\mathbf{r})} dv \tag{4.27}$$

where V is the volume of the unit cell. If we assume that there are n atoms in one unit cell and that each one of them can be considered as a rigid sphere, F_H can be obtained by the sum of discrete quantities in the form

$$F_H = \sum_n f_n e^{(i2\pi \mathbf{H}\cdot\mathbf{r_n})} \tag{4.28}$$

where f_n is the atomic scattering factor of the nth atom.

The electric field $\mathbf{E}$ in a dielectric material causes the bound charges (atomic nuclei and their electrons) to separate thus inducing a local electric dipole moment. The electric displacement field $\mathbf{D}$ can be defined as

$$\mathbf{D} = \epsilon_0 \mathbf{E} + \mathbf{P} \tag{4.29}$$

where ϵ_0 is the vacuum permittivity and $\mathbf{P}$ is the polarization. In a linear, homogeneous and isotropic dielectric $\mathbf{P}$ depends linearly on $\mathbf{E}$ so that we can write

$$\mathbf{P} = \epsilon_0 \chi \mathbf{E} \tag{4.30}$$

where χ is the electric susceptibility of the material. At this point equation 4.29 can be rewritten as

$$\mathbf{D} = \epsilon_0 \mathbf{E} + \mathbf{P} = \epsilon_0 \kappa \mathbf{E} \tag{4.31}$$

where $\kappa = 1 + \chi$ is the dielectric constant. This quantity can be extracted from Equation 4.31 in the form

$$\kappa = 1 + \frac{\mathbf{P}}{\epsilon_0 \mathbf{E}}. \tag{4.32}$$

It is now important to understand that the dielectric constant, which is a function of polarization and electric field, needs to be also related to the structure factor of Equation 4.28, so to really provide a complete description of the crystal. This step can be done by first relating it to the electron density $\rho(\mathbf{r})$ in the form

$$\kappa(\mathbf{r}) = 1 - r_e \frac{\lambda^2}{\pi} \rho(\mathbf{r}) \tag{4.33}$$

where r_e is the electron radius[5]. After introducing the symbol Γ

$$\Gamma = \frac{r_e \lambda^2}{\pi V},$$

[5]This equation can be derived after considering $\mathbf{P} = \rho(\mathbf{r}) ex$ where e is the electron charge and x is the amplitude electron motion induced by a sinusoidal electric field $\mathbf{E}$.[68]

we can rewrite Equation 4.33 as a Fourier series in the form

$$\kappa\left(\mathbf{r}\right) = 1 - \Gamma \sum_{H} F_H e^{(-i2\pi \mathbf{H}\cdot\mathbf{r})}. \tag{4.34}$$

It is now important to highlight the fact that the atomic scattering factor taken into account when deriving the structure factor formula, is also a complex quantity so that Equation 4.28 can be rewritten as

$$F_H = \sum_{n} \left(f + \Delta f^{'} + i\Delta f^{''}\right)_n e^{(i2\pi \mathbf{H}\cdot\mathbf{r})} = \sum_{n} \left(F_H^{'} + iF_H^{''}\right)_n e^{(i2\pi \mathbf{H}\cdot\mathbf{r})} \tag{4.35}$$

where $\Delta f^{'}$ and $\Delta f^{''}$ are the Hönl correction that also take resonance and absorption into account[68]. The importance of this two additional factor resides in the fact that for the case of $hkl = 000$ the dielectric constant is still complex in the form

$$\kappa_0 = 1 - \Gamma \left[F_0^{'} + iF_0^{''}\right] \tag{4.36}$$

where $F_0^{'}$ and $F_0^{''}$ are real quantities. It is worth noticing that the linear absorption coefficient is related to the imaginary part of the average dielectric constant

$$\mu_0 = \frac{2\pi}{\lambda}\Gamma F_0^{''}. \tag{4.37}$$

4.3.2 Maxwell's equations solution

Under the assumptions that the electric and magnetic fields can be expressed as sums of plane waves, that the crystal has the same magnetic behavior as empty space and that the conductivity σ is zero at X-ray frequencies, we can write Maxwell's equations in the form

$$\begin{aligned} (a) \qquad & \nabla \times \mathbf{E} = -\mu_0 \frac{\partial \mathbf{H}}{\partial t} \\ (b) \quad & \nabla \times \mathbf{H} = \frac{\partial \mathbf{D}}{\partial t} = \epsilon_0 \frac{\partial(\kappa \mathbf{E})}{\partial t}. \end{aligned} \tag{4.38}$$

where $\mathbf{D} = \epsilon_0 \kappa \mathbf{E}$ is the electric displacement field. If we now assume that an incoming beam of wave vector $\mathbf{K}_0$ interacts with the crystal so that a scattered wave is generated by the Fourier components of charge density described by the reciprocal lattice vector H ($|H| = 1/d$ where d is the spacing between

crystallographic planes), then we can write the scattered wave vector as

$$\mathbf{K}_H = \mathbf{K}_0 + \mathbf{H} \tag{4.39}$$

which is equivalent as to say that the momentum is conserved after the scattering event. It is worth noticing that the wave vector $\mathbf{K}$ is complex so that it can be written as

$$\mathbf{K} = \mathbf{K}^{'} - i\mathbf{K}^{''} \tag{4.40}$$

where the imaginary part describes absorption.

At this point one can use the plane wave approximation for both magnetic and electric fields, apply it in equations 4.38a and .b, and together with the expression provided for the dielectric constant in Equation 4.34, it is now possible to come to a solution. The fundamental set of equations describing the field inside the crystal can be reduced to a set of two when considering the case of only one active reflection inside the crystal. They can be written in the form [68]

$$\begin{aligned} \left[k^2\left(1-\Gamma F_0\right)-\left(\mathbf{K}_0\cdot\mathbf{K}_0\right)\right]E_0 - k^2P\Gamma\bar{F}_H E_H = 0, \\ -k^2P\Gamma F_H E_0 + \left[k^2\left(1-\Gamma F_0\right)-\left(\mathbf{K}_H\cdot\mathbf{K}_H\right)\right]E_H = 0 \end{aligned} \tag{4.41}$$

where P is a parameter whose value changes in accordance with the polarization state under consideration ($P = 1$ for the σ polarization and $P = cos2\theta$ for the π one) and k is the vacuum value of the wave vector. In order to solve this set of two equations it is possible to study the determinant of the associated matrix and set it to zero in order to avoid trivial solutions:

$$\begin{vmatrix} k^2\left(1-\Gamma F_0\right)-\left(\mathbf{K}_0\cdot\mathbf{K}_0\right) & -k^2P\Gamma\bar{F}_H E_H \\ -k^2P\Gamma F_H E_0 & k^2\left(1-\Gamma F_0\right)-\left(\mathbf{K}_H\cdot\mathbf{K}_H\right) \end{vmatrix} = 0 \tag{4.42}$$

where F_i are the structure factors of the corresponding reflections. It is worth noticing that the terms on the principal diagonal of matrix 4.42 represent the difference between the square of the wave vectors $\mathbf{K}_i$ inside the crystal and the square of the vacuum value k^2 corrected by the factor $(1-\Gamma F_0)$. If this difference is zero, there is no unique solution for the set of equations. It is now clear that this

difference is the most important parameter in this problem. In order to better understand these terms it is possible to define two new parameters[6]

$$\begin{aligned} (a) \quad & \xi_0 = (\mathbf{K}_0 \cdot \mathbf{K}_0)^{1/2} - k\left(1 - \tfrac{1}{2}\Gamma F_0\right) \\ (b) \quad & \xi_H = (\mathbf{K}_H \cdot \mathbf{K}_H)^{1/2} - k\left(1 - \tfrac{1}{2}\Gamma F_0\right), \end{aligned} \tag{4.43}$$

where ξ_0 represents the difference between the wave vector inside the crystal $\mathbf{K}_0$ and the vacuum value corrected by the average index of refraction[7]. If we now rewrite Equation 4.42 introducing these new parameters, we find

$$\xi_0 \xi_H = \frac{1}{4} k^2 P^2 \Gamma^2 F_H F_{\overline{H}} \tag{4.44}$$

which is commonly known as *dispersion surface* and where term $F_{\overline{H}}$ is the structure factor for the $\left(\overline{hkl}\right)$ reflection[8]. We can now say that all the solution of Maxwell's equations will need to exist within this surface.

The important role of these new elements becomes clearer when considering the Ewald's sphere construction. The main difference with what described in the previous sections is that we need to take the wave vector correction into account. If in the normal case the centre of Ewald's sphere is given by the Laue point, whose distance from the origin of the reciprocal lattice is k, now we need to change the radius of our sphere so that it becomes $k - \left(1 - \frac{1}{2}\Gamma F_0\right)$ as shown in Figure 4.13.a. This traduces in a change of the sphere's centre which moves to point Q. In order to find the dispersion surface we need to draw two spheres of radius $k - \left(1 - \frac{1}{2}\Gamma F_0\right)$ centered around points H and O, as illustrated in Figure 4.13.b, which respectively represent the (hkl) reflection and the origin of the reciprocal lattice. As expected these two spheres will meet at point Q. If we now draw the two vectors $\mathbf{K}_0$ and $\mathbf{K}_H$ departing from points O and H respectively, we can observe that they will meet the two spheres in two distinct points as shown in Figure 4.13.b. The two points represent the difference between the wave vectors $\mathbf{K}_0$ and $\mathbf{K}_H$ and the $k - \left(1 - \frac{1}{2}\Gamma F_0\right)$ term; in other words they represent ξ_0 and ξ_H. It is now easier to visualize the dispersion surfaces as the hyperbolic sheets drawn in Figure 4.14.c. Point

[6] It is possible to write for each equation $2k\xi \equiv (\mathbf{K} \cdot \mathbf{K}) - k^2\left(1 - \Gamma F_0\right)$ and by writing the righthand side term as the product of the sum and difference one can obtain $2k\xi = 2k\left[(\mathbf{K}_0 \cdot \mathbf{K}_0)^{1/2} - k\left(1 - \frac{1}{2}\Gamma F_0\right)\right]$.

[7] This can be observed by recalling that the index of refraction is $n = \sqrt{\kappa}$.

[8] Even though we assumed that only the (hkl) reflection was operative, the presence of this structure factor is reasonable since in our system we assume that the wave with wave vector $\mathbf{K}_H$ is scattered by the backside of the atomic planes back into the $\mathbf{K}_0$ direction.

A showed in figure 4.13(b) lays on one of the hyperbolic sheets and so it is a possible solution of our problem.

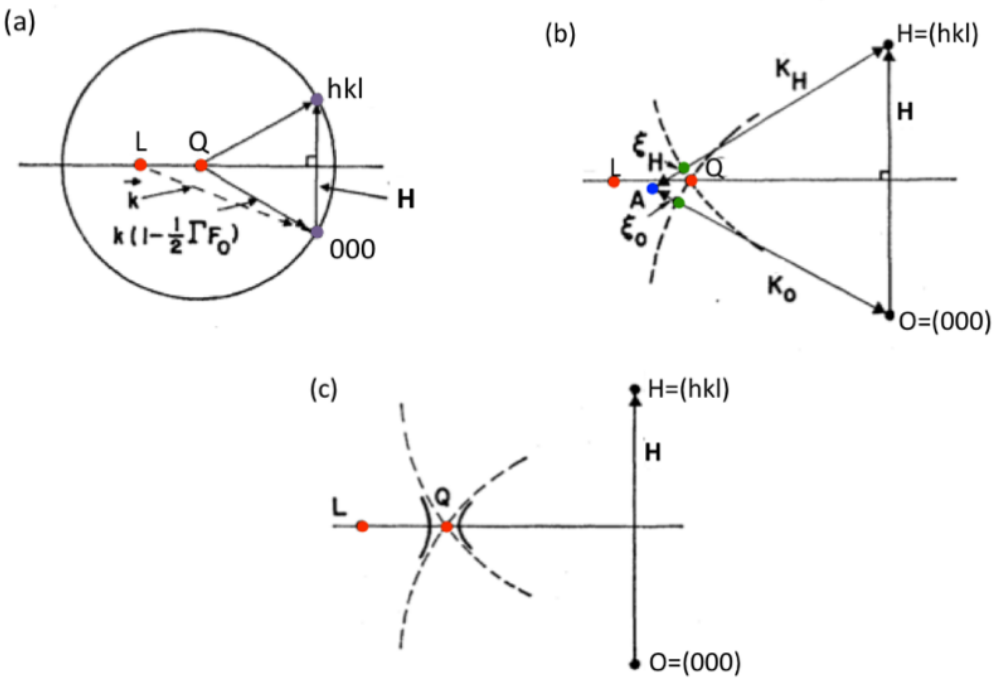

Figure 4.13: Construction of Ewald's sphere and dispersion surface retrieval. (a) If compared with the vacuum case, the Ewald's sphere has a shorter radius which takes the correction factor $\left(1-\frac{1}{2}\Gamma F_0\right)$ into account. Point O represents the origin of the reciprocal lattice, while point H is the (hkl) reflection. (b) In order to find the two factors ξ_0 and ξ_H we need to graphically apply equation 4.43 which corresponds to subtracting quantity $k\left(1-\frac{1}{2}\Gamma F_0\right)$ from vectors $\mathbf{K}_0$ and $\mathbf{K}_H$. Point A is a valid tie point from which wave vectors can be drawn to O and H to represent permitted solutions of Maxwell's equations. (c) The dispersion surfaces are hyperbolic sheets and can be defined as the locus of tie points. We can identify two branches: the one closer to the Laue point, L, is commonly called α branch, while the other one is the β branch. It is worth noticing that the polarization parameter P affects the definition of the dispersion surfaces, so that we will have a set of two branches for the σ polarization and another set for the π polarization ($P=1$ for the σ polarization and $P=cos2\theta$ for the π one). Figure adapted from [68].

There are few considerations that need to be done at this point. The first is related to the geometry of the problem under examination which is in the Laue case, as shown in Figure 4.12. The Bragg geometry will not be treated in this Chapter, however it is possible to say that similar considerations to the ones done so far, can apply to this new case. In particular the dispersion surfaces will be oriented

in a different way so to account for the fact that in this geometry the diffracted beams exits from the same face that the incident beam enters.

Another thing worth noticing is that the dispersion surface is a complex quantity and this can be explained by remembering that the wave vectors are also complex. For this reason one can derive the real and imaginary parts of ξ_0 in the form

$$\begin{aligned} (a) \quad & \xi_0^{'} \cong K_0^{'} - k\left(1 - \tfrac{1}{2}\Gamma F_0^{'}\right) \\ (b) \quad & \xi_0^{''} \cong -K_0^{''} cos\beta + \tfrac{1}{2}k\Gamma F_0^{''}, \end{aligned} \tag{4.45}$$

where β is the angle between $\mathbf{K}^{'}{}_0$ and $\mathbf{K}^{''}{}_0$ [68]. This result shows us that the real and imaginary parts of ξ_0 are closely related to those of $\mathbf{K}_0$. For this reason one can conclude that the absorption process is strictly related to $\xi_0^{''}$ and that it is function of the excited tie point as shown in Figure 4.14.

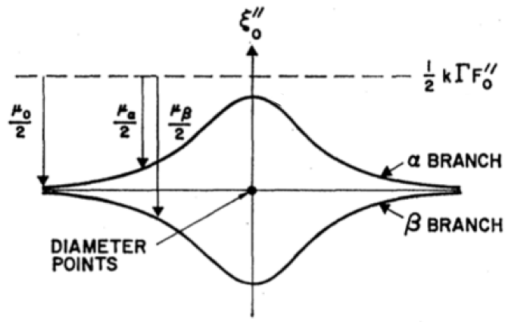

Figure 4.14: Absorption associated with each tie point. The two curves relative to the α and β branches are shown for different tie points and are derived as a difference from the upper curve set to the value $\xi_0^{''} = \frac{1}{2}k\Gamma F_0^{''}$. If confronting with equation 4.45 one can easily see that the different behavior is contained within term $-K_0^{''} cos\beta$ where $K_{0\alpha}^{''} \neq K_{0\beta}^{''}$. The diameter points are tie points that are in the Bragg condition configuration; this will be explained later in the text. Figure adapted from [68].

In order to better understand the meaning of tie points it is necessary to investigate what happens when an incoming beam hits the entrance surface of an extended crystal in the Laue geometry. To start, we need to set boundary conditions for both wave vectors and fields. One can easily write the

boundary conditions for the amplitudes of incident and diffracted fields as

$$\begin{aligned} (a) \quad & \mathbf{E}_0^i = \mathbf{E}_{0\alpha} + \mathbf{E}_{0\beta} \\ (b) \quad & 0 = \mathbf{E}_{H\alpha} + \mathbf{E}_{H\beta}, \end{aligned} \tag{4.46}$$

where the conservation of energy is imposed. When considering wave vectors, geometrical considerations need to be done. In the reciprocal space that we have described so far, we can imagine the incident wave vector $\mathbf{k}_0^i$ as entering the Ewald sphere somewhere, point P, and ending at the origin O of the reciprocal lattice as shown in Figure 4.15.a. The direction followed by $\mathbf{k}_0^i$ is perpendicular to the physical entrance surface of the crystal, line SS. If point P coincides with the Laue point L it means that the incidence angle is the Bragg one, but in the case they are different it is possible to estimate the deviation from the correct Bragg angle as $\Delta\theta = LP/k$ where, as previously mentioned, k is the LO distance. It is now possible to see that when the incoming wave enters through point P, it crosses the dispersion surface in two points, A and B in the figure; these are the tie points relative to the entrance point P at the α and β branches, respectively. Starting from these tie points, we can finally draw the two vectors $\mathbf{K}_{0\alpha}$ and $\mathbf{K}_{\mathbf{0}\beta}$ which satisfy the boundary condition at the entrance surface

$$\begin{aligned} (a) \quad & \mathbf{K}_{0\alpha} = \mathbf{k}_0^i - \mathbf{PA} \\ (b) \quad & \mathbf{K}_{0\beta} = \mathbf{k}_0^i - \mathbf{PB}. \end{aligned} \tag{4.47}$$

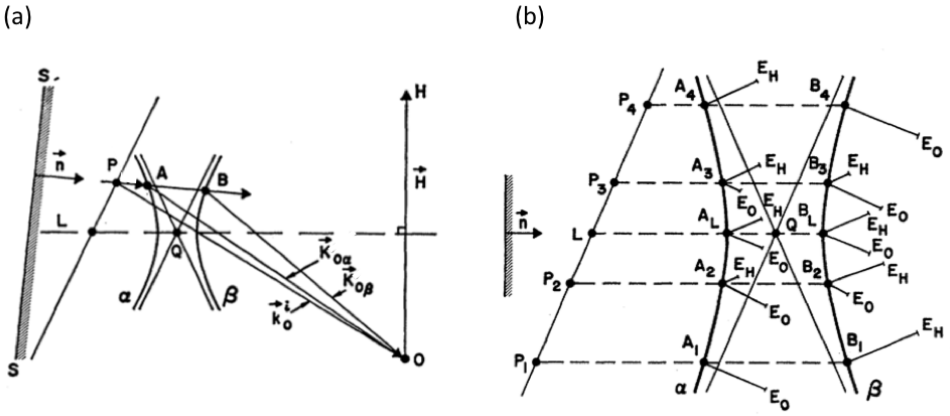

Figure 4.15: Tie points in dispersion surfaces. (a) Schematic representation of how to select a couple of tie points by using the entrance point P. Vector **PO** represents the outside incident wave vector, while **AO** and **BO** are the inside incident wave vectors. (b) Tie points for the case where the normal vector to the entrance surface SS is parallel to LQ. If the entrance point corresponds with L the Bragg condition is fully satisfied. Points $A_L$and $B_L$are called diameter points. Figure adapted from [68].

If for simplicity we now consider the case where the perpendicular to the entrance surface SS is parallel to the line LQ, we find a difference configuration that is shown in Figure 4.15.b. In the case the tie points on the hyperbolas are also lying on LQ, this meaning that the incident angle is exactly the Bragg angle, we find that the distance between these two points is the minimum distance between the two branches. This distance is known as diameter D of the hyperbola and for this reason the two tie points are named diameter points. An expression for D can be written in the form [68]

$$D = k\Gamma \left|P\right| \left|F_H\right| sec\theta_B. \tag{4.48}$$

It is worth noticing that Figure 4.15.b also shows how different tie points on the dispersion surface characterize the ratio of the field amplitudes. Following Batterman and Cole's analysis [68] one can write

$$\frac{E_0}{E_H} = -\frac{2\xi_0}{kP\Gamma F_{\overline{H}}} = -\frac{kP\Gamma F_H}{2\xi_H}, \tag{4.49}$$

which represents the ratio of the field amplitudes for each tie point. For points well off the Bragg condition, such as P_1or P_4, we see that one of the two components vanishes and this can be explained by saying that either ξ_0 or ξ_H goes to zero. In the case of diameter points the ratio of the field

amplitudes is equal to one.

Another important phenomenon that takes place is the Pendellösung that is one of the consequences of the gap between the two branches of a dispersion surface. The waves emerging from each tie point travel inside the crystal with slightly different wave vectors. Thus, at some locations within the crystal they can superpose constructively or destructively. The oscillation between the two conditions is known with the name of Pendellösung effect for crystals (Pendellösung from German means solution of the pendulum). This effect can also be seen if one calculates the time average of the Poynting vector $\langle \mathbf{P} \rangle = \frac{1}{2}\mathscr{R}\left[\mathbf{E} \times \mathbf{H}\right]$ that shows how the flux of energy changes when two tie points are considered. The solution obtained by [68] is

$$\mathbf{S}_T = \mathbf{S}_\alpha + \mathbf{S}_\beta + \mathbf{S}_{\alpha\beta}, \tag{4.50}$$

where $\mathbf{S}_\alpha$ and $\mathbf{S}_\beta$ are the effective energy flows associated with a tie point on the α and β branches and are independent from the depth inside the crystal, while $\mathbf{S}_{\alpha\beta}$ is an oscillating term that has a sinusoidal dependence. Its value is related to the difference $(\mathbf{K}_{0\alpha} - \mathbf{K}_{0\beta})$ and by looking at the geometrical construction of Figure 4.15.a this quantity is the distance between the coupled tie points and lays on the normal direction to the surface SS. The Pendellösung period can be written in the form

$$\mathcal{P} = \frac{1}{(\mathbf{K}_{0\alpha} - \mathbf{K}_{0\beta})} \tag{4.51}$$

and in the case of the symmetric Laue case at the Bragg angle, $1/\mathcal{P}$ is simply the diameter of the hyperbola of the dispersion surface of Equation 4.48 [68, 69]. Following the geometrical construction of Figure 4.16, one can notice that $\mathbf{S}_\alpha$ and $\mathbf{S}_\beta$ are perpendicular to the hyperbola at the tie points A and B. The different directions of the two vectors show that the two energy flows are directed above and below the atomic planes. In the case when L is the incidence point, the two vectors lay on line LQ this meaning that the energy flows along the atomic planes. The coupling vector $\mathbf{S}_{\alpha\beta}$ orientation changes as a function of the depth so that it cancels the two $\mathbf{S}_\alpha$ and $\mathbf{S}_\beta$ contributions in the primary beam direction $\mathbf{s}_0$ or in the diffracted beam direction $\mathbf{s}_H$ with a period $\mathcal{P}$ [9]. For this reason, if the crystal is very thin with respect to a Pendellösung period there is no diffracted beam. When the thickness of the crystal reaches one-half of P, we have that at the Bragg angle all the energy flows in the diffracted beam direction. If we move from the Bragg condition this energy gets smaller so that

[9] $\mathbf{s}_i$ are unit vectors defining the incoming and diffracted beams directions.

we can understand that with respect to the varying θ angle around the Bragg, we can find a changing integrated intensity for the diffracted beam. When the crystal gets as thick as the Pendellösung period, there is again no diffracted beam.

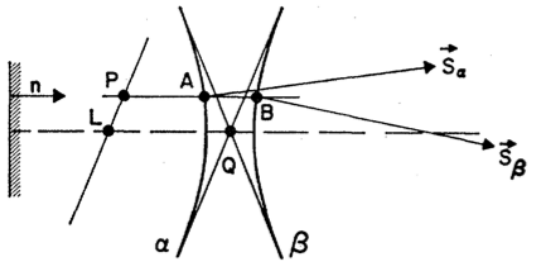

Figure 4.16: Pointing vectors associated with two tie points. For the case where the entrance point is L the two vectors will be perpendicular to the surface. Figure extracted from [68].

After multiple interactions within the crystal, the generated waves reach the exit surface. In this case we can write the boundary conditions for the fields intensities in the $\mathbf{s}_0$ and $\mathbf{s}_H$ directions

$$\begin{aligned} (a) \quad & \left|\mathbf{E}_H^e\right|^2 = \left|\mathbf{E}_{H\alpha}\right|^2 + \left|\mathbf{E}_{H\beta}\right|^2 \\ (b) \quad & \left|\mathbf{E}_0^e\right|^2 = \left|\mathbf{E}_{0\alpha}\right|^2 + \left|\mathbf{E}_{0\beta}\right|^2, \end{aligned} \tag{4.52}$$

which mean that the fields just inside the boundary equals the fields just outside. For what concerns the boundary condition on the wave vectors, it is possible to easily conclude that in the case of Laue diffraction where the exit surface is parallel to the entrance surface, $\mathbf{k}_0^e$ of the exit wave is the same as $\mathbf{k}_0^i$ at the entrance.

It is now possible to understand what happens in terms of diffracted and forward diffracted intensities. For the diffracted intensity given by either the α or β branches, it is common use to derive the rocking curve that can be written as a function of θ as [68]

$$\frac{I_H}{I_0} = \frac{1}{4}\frac{1}{1+\eta^2} e^{-\frac{\mu_0 t}{cos\gamma}\left(1 \mp \frac{|P|}{\sqrt{1+\eta^2}}\right)}, \tag{4.53}$$

where $\eta = (\Delta\theta sin2\theta) / |P| \Gamma \left|F_H^{'}\right|$, t is the thickness of the crystal, γ is the angle between the surface and the incoming beam, and P is the polarization state as defined above. For a given polarization

state (σ or π) the shape of the rocking curve can be retrieved for different crystal thicknesses, as shown in Figure 4.17. In the case of a thin crystal the factor $\mu_0 t$ tends to zero so that the exponential part disappears from Equation 4.53

$$\frac{I_H}{I_0} = \frac{1}{2}\frac{1}{1+\eta^2}, \tag{4.54}$$

where we are considering the two α and β contributions together (this explains why we see $1/2$ instead of $1/4$). Similar considerations can be done for the thick crystal which corresponds to condition $\mu_0 t > 10$ where the corresponding peak will result less tall. It is worth noticing that these different behaviors for thin and thick crystals are in accordance with what predicted by considering the Pendellösung effect.

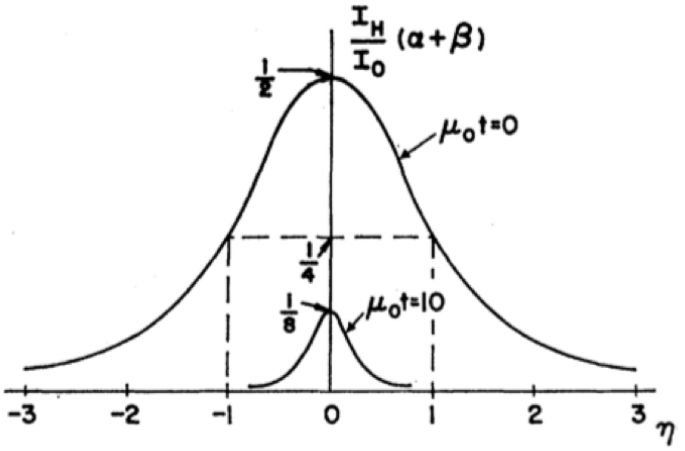

Figure 4.17: Rocking curves for crystals in the Laue geometry. The taller curve is relative to a thin crystal while the lower one describes the case of a thick crystal. Figure adapted from [68].

The forward diffracted or transmitted beam is of great interest since it shows the effect of the anomalous transmission, if the proper conditions are met. In this case we can define the intensity ratio between the exit wave in the $\mathbf{s}_0$ direction and the incoming beam as [68]

$$\frac{I_0^e}{I_0} = \frac{1}{4}\left(1 \mp \frac{\eta}{\sqrt{1+\eta^2}}\right)^2 e^{-\frac{\mu_0 t}{cos\gamma}\left(1 \mp \frac{|P|}{\sqrt{1+\eta^2}}\right)}, \tag{4.55}$$

where if we consider the thin crystal case $\mu_0 t \to 0$ we get for each polarization state

$$\frac{I_0^e}{I_0} = \frac{1}{4}\left(1 - \frac{\eta}{\sqrt{1+\eta^2}}\right)^2 + \frac{1}{4}\left(1 + \frac{\eta}{\sqrt{1+\eta^2}}\right)^2. \tag{4.56}$$

The first term represents the α branch while the other term represents the β branch. The two curves can be graphically composed as shown in Figure 4.18.a. As expected, in the case of thin crystals the transmitted intensity has a dip for a range of angles around the Bragg angle. If we now study the case of a thick crystal we will get a different curve that shows the anomalous transmission peak as in Figure 4.18.b.

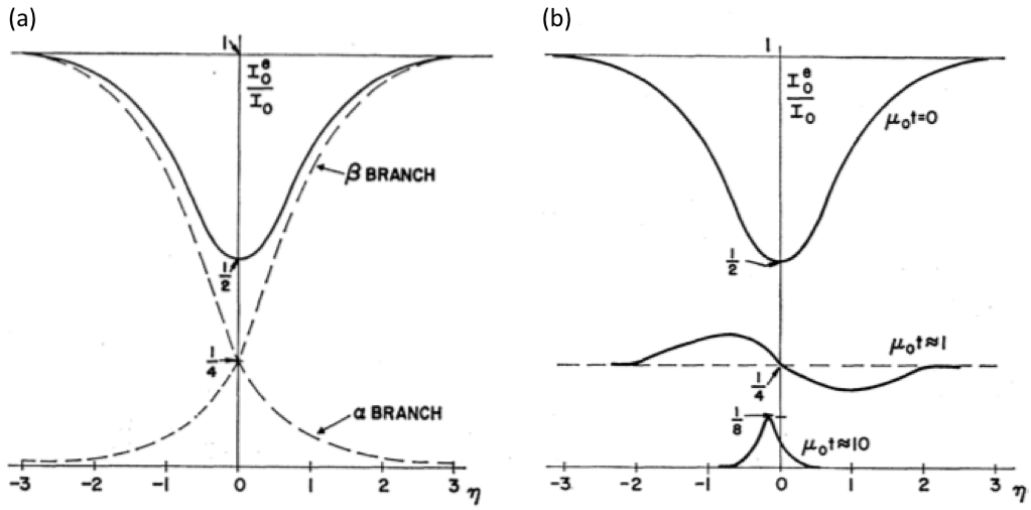

Figure 4.18: Forward diffracted beam representation. (a) The two components of the α and β branches are used to derive the forward diffracted beam integrated intensity for the case of a think crystal. (b) Curves are shown for different thicknesses. A peak results for the thick crystal, this accounting for the case of anomalous transmission. Figure adapted from [68].

Chapter 5

First experimental results: gold nanoscrystals

5.1 Ptychography on gold nanocrystals

Gold nanocrystals have been the subject of study of the UCL group for a number of years. This experiment was performed by using ptychography to collect diffraction patterns in the transmission geometry, while rocking the sample at different angles around the Bragg condition. We also used a second detector at the Bragg angle, in reflection geometry, with the aim of collecting the reflected intensities to then retrieve the experimental rocking curve. As a result we could measure, for a set of rocking angles around the Bragg condition, a phase shift in the transmitted beam.

5.1.1 Experimental setup

This experiment was conducted at the coherent small-angle X-ray scattering (cSAXS) beamline at the Swiss Light Source, Paul Sherrer Institute in Villigen, Switzerland. The experimental setup is shown in Figure 5.1 and was composed of several components precisely aligned with the aid of an X-ray camera. To focus the beam we used a 75 micron diameter Fresnel Zone Plate (FZP) made of Au with 100 nm outermost zone width, and 1 micron thickness. A central stop of 30 micron diameter was placed upstream the FZP to block the zeroth diffraction order. Downstream of the FZP we used a 20 micron pinhole serving as order sorting aperture (OSA) to select the first diffraction order. The focal length

of the zone plate was 52.66 mm at the energy of 8.7 KeV.

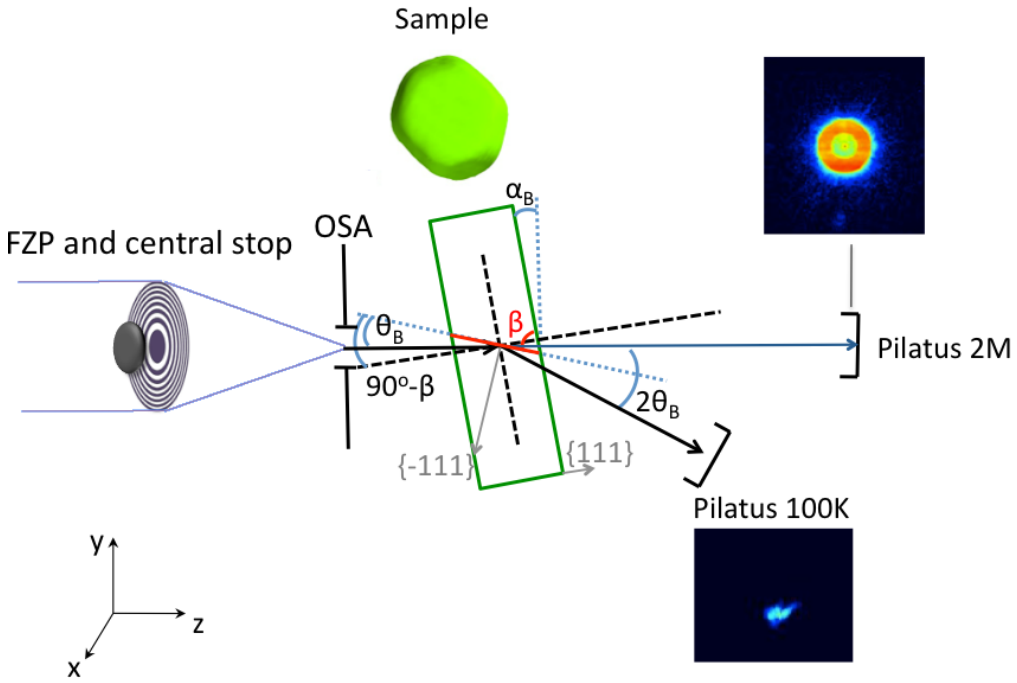

Figure 5.1: Lateral view of the experimental setup. A Fresnel zone plate is used to focus the beam. The Au nanocrystals were placed at the focus with their {111} crystal planes oriented at the angle α_B with respect to the incoming beam. A 2D detector is placed in the forward direction and another 2D detector in the direction of the Bragg reflection.

Our sample consisted of a random array of 250 nm gold nanocrystals with cylindrical shape, grown on a 100 nm thick Si_3N_4 membrane. The scanning electron microscope (SEM) analysis confirmed the size of the crystals and showed a mutual spacing of approximately 1 micron. The Au nanocrystals were oriented with the {111} crystallographic planes normal to the substrate. By rotating the sample membrane to an angle of $\alpha_B = 1.86$ deg, we aligned the Au {111} reflection, with Bragg angle $\theta_B = 18$ deg. The sample was mounted downstream at the focus of the FZP which was illuminated with a coherent beam, forming the ptychographic probe. The expected beam size for this experiment is equal to the FZP outermost zone width of 100 nm, but a more precise estimation can be done by analyzing the reconstructed probe profile (Figure 5.2).

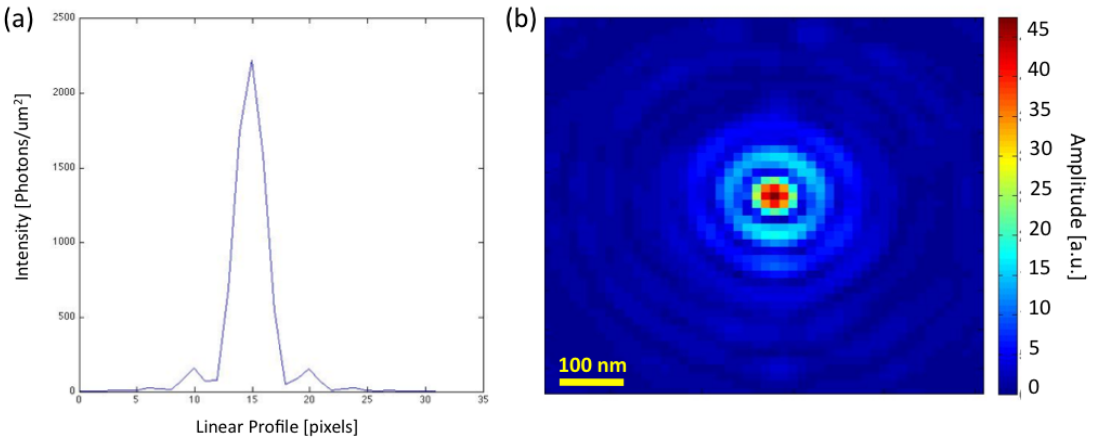

Figure 5.2: Reconstructed probe's intensity linear profile (a) and amplitude (b).

The beam size can be retrieved by measuring the FHWM in the probe linear profile and by multiplying it by the pixel size at the sample plane which for this configuration is around $31nm$.

$$pix_{sample} = \frac{\lambda z}{npix_{det}} \tag{5.1}$$

where z is the sample-detector distance, in this case $7.2m$ in the forward direction and n is the recorded data array size, 192 for us. The result is a beam size of around $110nm$ which is consistent with what expected.

We used two Pilatus detectors to collect the diffracted and transmitted intensity distributions while scanning the sample across the probe. As shown in Figure 5.1, a Pilatus 2M detector was placed at 7.2 m from the sample in the transmission direction, while a smaller Pilatus 100k was placed at the reflected Bragg direction at an angle $2\theta_B = 36$ deg and at a distance of 1.03 m.

We started our experiment by finding a crystal at the precise Bragg angle at which our reflection detector would collect the highest intensity (as shown in Figure 53), then we defined a series of angles centered around the Bragg angle and we performed a ptychographic acquisition at each of them. The whole set of positions is observed in a rocking curve where the integrated intensity is plotted at each angle.

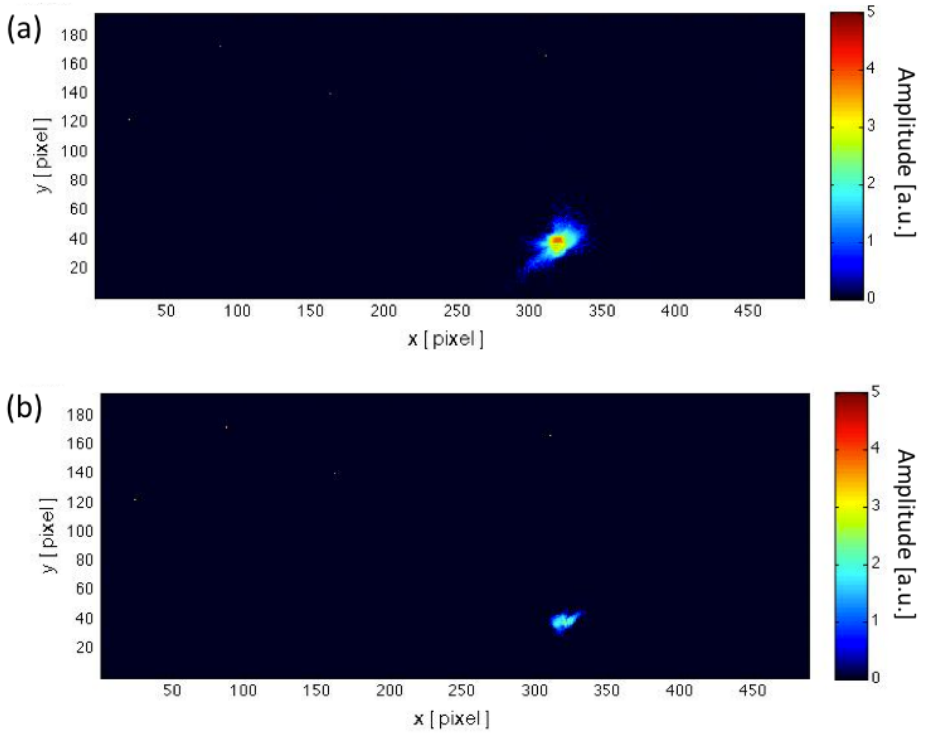

Figure 5.3: Recorded intensity on the PILATUS 100k detector. In (a) the Bragg angle is detected, while in (b) the weaker intensity confirms that we are off the Bragg.

The rocking curve for a set of nine scans around the Bragg angle can be observed in Figure 5.4.

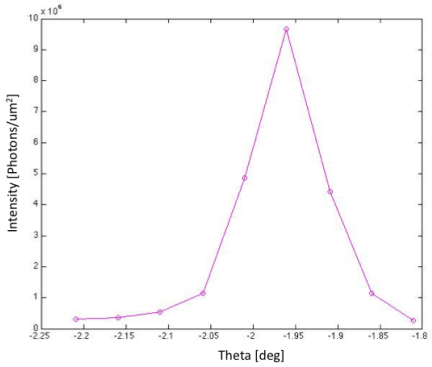

Figure 5.4: Rocking curve for a set of scans.

Once defined the rocking curve, we performed a series of ptychographic acquisitions by circular-scanning the sample.

5.1.2 Data analysis

Each ptychographic data sets consisted of a series of 458 acquisitions of 0.5 sec in a grid of concentric circles with a radial step size of 0.05 microns covering a field of view of 1.2x1.2 microns [53]. Ptychographic reconstructions were done using a difference map algorithm described in [60, 61]. For the reconstructions, a region of the Pilatus 2M detector od 192x192 pixels was used, corresponding to a pixel size of 31.2 nm in the reconstructed image.

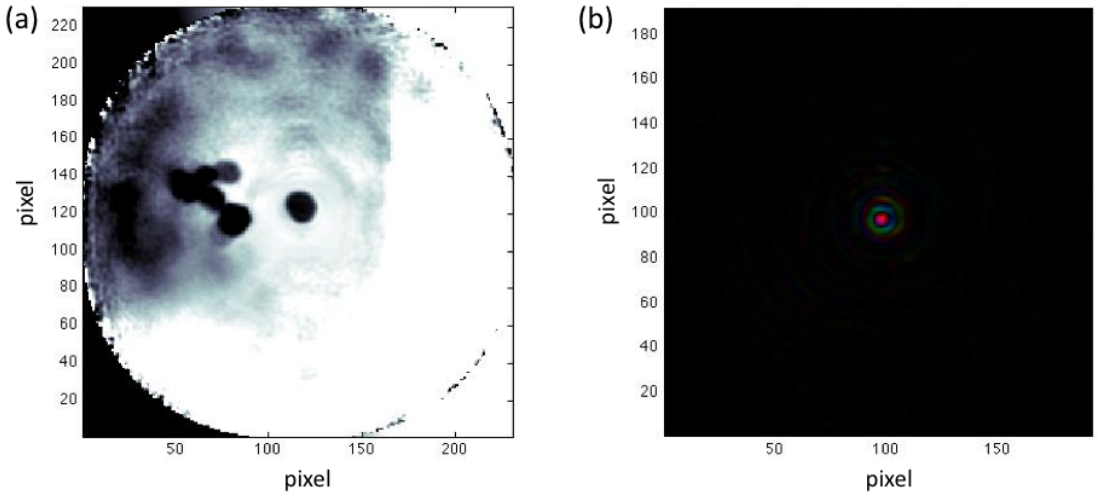

Figure 5.5: Reconstructed sample phase (a) and probe (b)

Reconstructed phase images where then corrected for a phase offset and ramp which are ambiguities arising from the ptychographic reconstructions [70].

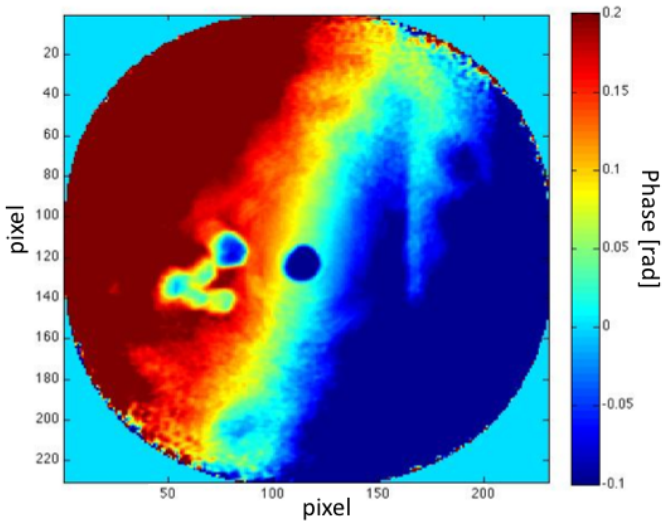

Figure 5.6: Phase ramp on the reconstructed sample.

The phase ramp removal method being used was based on the search of gradients in the reconstructions. The above figure also shows that during each reconstruction the field of view also included other structures as well as the edge of the sample support. This of course contributed to the formation of the phase ramp. For this reason and to better analyze the reconstructions, a region of interest was defined around the crystal in order to only concentrate the data analysis on that portion of the reconstructed phase. One other issue was relative to the drift of the sample. In fact since we performed very long acquisitions during our experiment (usually 456 points for each ptychographic scan) a drift of the sample was inevitable. In order to compare all phase profiles we needed to register the reconstructed images with subpixel precision using the method described in [71].

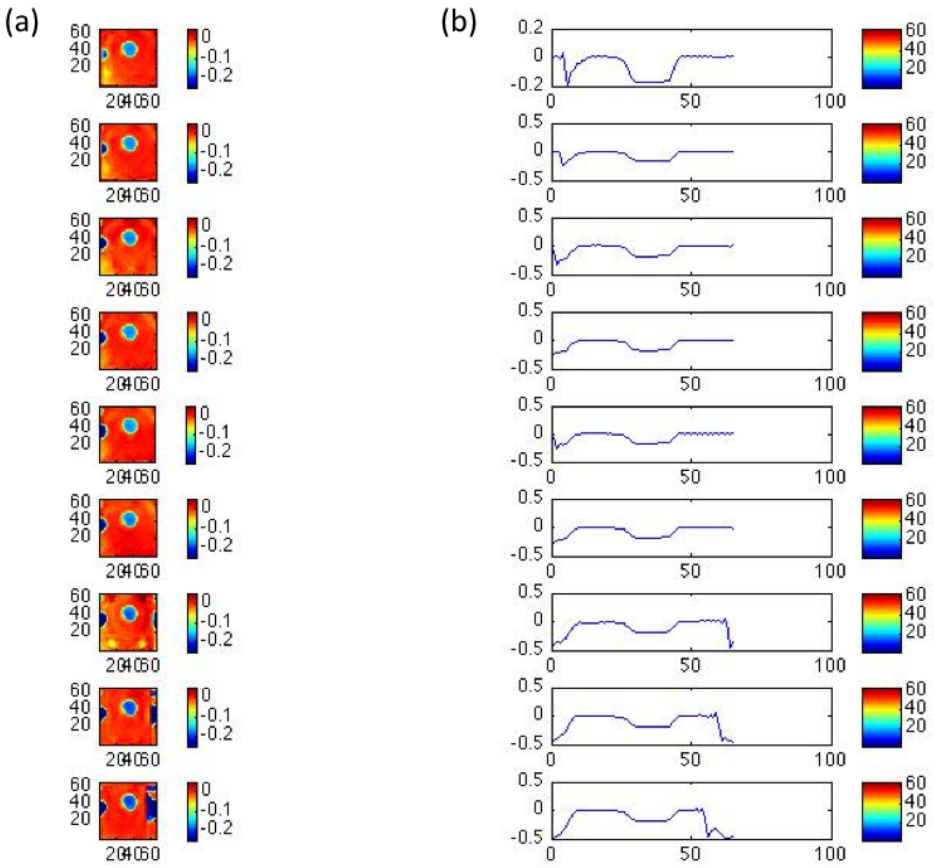

Figure 5.7: Reconstructions alignments (a) and linear phase profiles (b).

It appears clear that in order to establish if the observed phase shift inside the crystal could really be quantified in 0.03 rad, further analysis were needed. In particular we wanted to make sure that the noise outside the crystal was negligible if compared with the phase shift inside the crystal itself. For this reason we wrote a Matlab routine to draw boxes outside and inside the crystal. We then used the phase values in each box to estimate the mean value and the standard deviation. In this way it was possible to calculate the error which affected the reconstructions and to define error-bars which helped to establish if the phase shift inside the crystal was bigger than the noise or not.

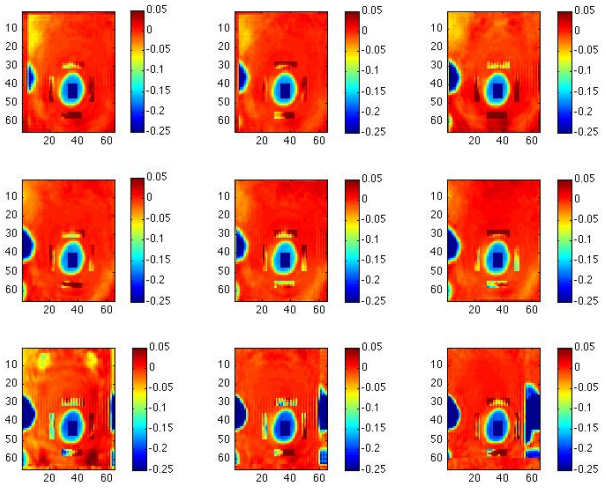

Figure 5.8: Boxes used to calculate the mean value and the standard deviation of the phase inside and outside the crystal.

In the end we obtained a graphic of phase versus angles showing nine points and error-bars. The phase value for each scan (identified by the correspondent angle) was calculated as

$$phase_{av} = phase_{av,c} - \frac{phase_{av,1} + phase_{av,2} + phase_{av,3} + phase_{av,4}}{4} \tag{5.2}$$

where $\text{phase}_{\text{av,c}}$is the average phase calculated in the box inside the crystal and $\text{phase}_{\text{av,i}}$are the phases calculated in the four boxes outside the crystal. The error-bars were calculated for each scan by combining the standard deviation of the phase in each box following the formula

$$\varepsilon_{tot} = \sqrt{\varepsilon_c^2 + \frac{1}{16}\varepsilon_1^2 + \frac{1}{16}\varepsilon_2^2 + \frac{1}{16}\varepsilon_3^2 + \frac{1}{16}\varepsilon_4^2} \tag{5.3}$$

where $\varepsilon_{\text{i}}$are the squared standard deviation inside and outside the crystal.

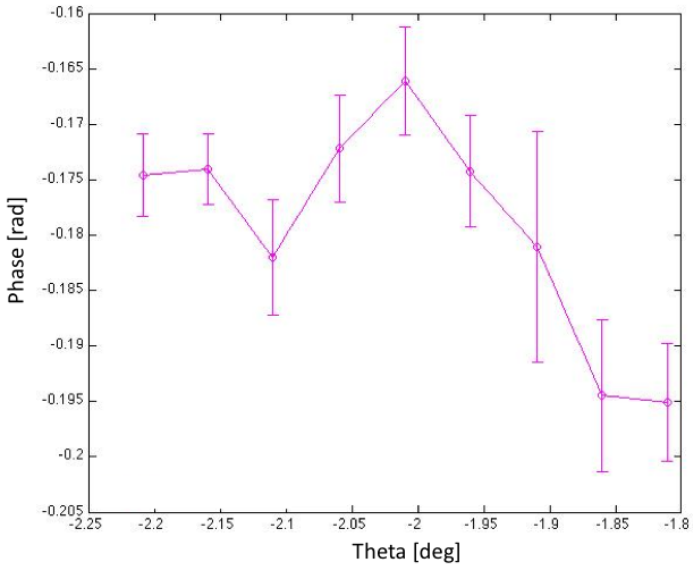

Figure 5.9: Error-bar plot showing the phase shift. The error-bars have been plotted with amplitude of $\pm\varepsilon_{\text{tot}}$. The plot is centered around the Bragg angle position and it is possible to see that the maximum phase shift between the on and off Bragg conditions is around 0.03 rad, as previously showed in Figure 5.8.

In order to make sure that this effect was also present in other sets of acquisitions, I also performed the data analysis, following all steps described above, for all our data. Besides the fact that the results I have been showing so far are relative to the biggest set we collected (nine scans well placed around the Bragg angle), a trend in the phase shift appears evident (Figure 5.10). It is worth noticing that all scans refer to the same crystal and in the figure are all centered around the Bragg. I also decided to include a set containing a bad reconstruction (the one drawn in red clearly shows a point which represents a bad reconstruction) to show that even in that case the trend is still visible if considering the well reconstructed scans of that series.

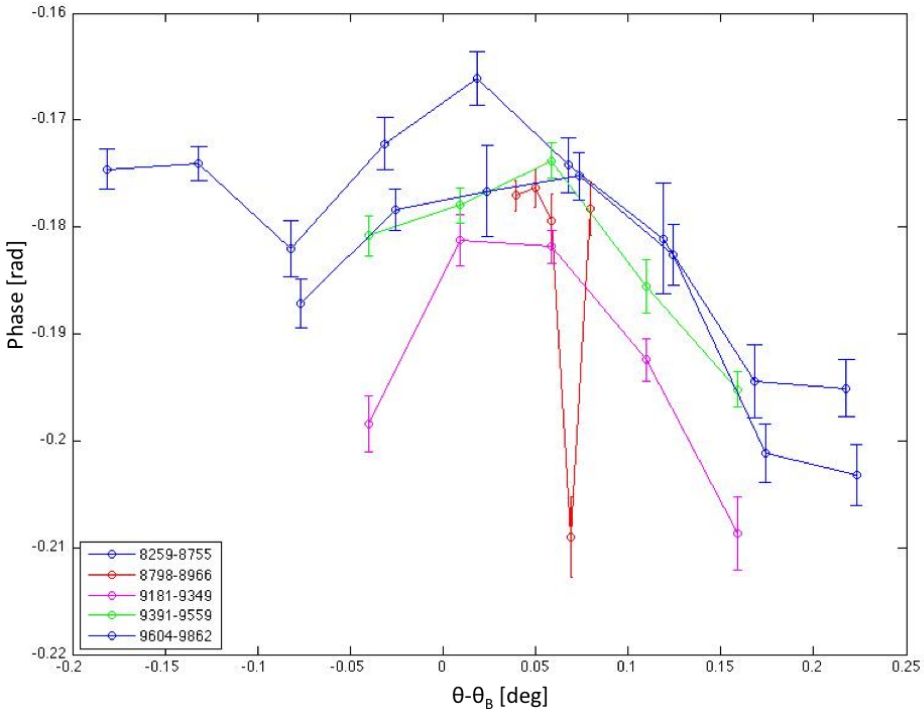

Figure 5.10: Phase shift trend in various sets of scans. In this figure all curves have been shifted so that the Bragg position is set to zero.

5.1.3 Theoretical background

We started this experiment with the aim of investigating the dynamical domain, which exists when diffraction takes place inside a thick crystal. In this case the dynamical theory describes how the scattered waves, emerging from various crystallographic planes, interact to define a total wave field inside the crystals as explained in Chapter 4.

In this section a first explananation to this effect is be provided by using a quasi kinematical approach where the scattering by a simple slab of crystal is examined. By only considering the phase contributions from each diffracting plane, we can decompose the complex amplitude of the scattered beam as

$$R_N(\mathbf{q}) = \alpha \sum_{\mathbf{j=0}}^{\mathbf{N-1}} \mathbf{e}^{\mathbf{q \cdot d_j}} = \alpha \frac{1 - e^{iqN}}{1 - e^{iqd}} \tag{5.4}$$

where N is the number of planes being considered, α is a cross section parameter which can be used to adjust the fitting to experimental data and d_j are the positions of the planes in the crystal. The term d is the 111 plane spacing, which is 0.235 nm for gold.

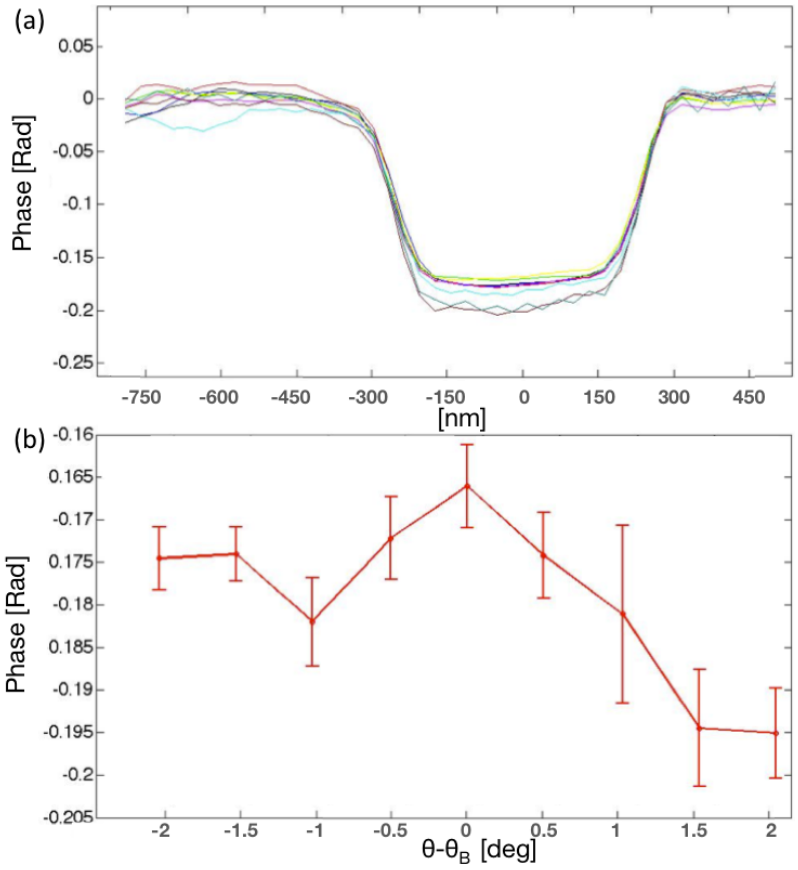

Figure 5.11: (a) Phase profiles for different angles theta around the Bragg reflection. (b) Phase shift difference between the particle and the outside region as a function of the angle theta around the Bragg reflection.

The experimental rocking curve can be plotted by integrating the intesities collected on the reflection detector. This is overlaid with the relationship $I_R(\mathbf{Q}) = |R(\mathbf{Q})|^2$, to compare experimental and theoretical data, as shown in Figure 5.12.a in red and green lines, respectively .

The transmitted wave in the forward direction (T) can be easily calculated from the reflected beam by considering that when energy is conserved, the transmitted beam is reduced by the generation of R and this can be modeled as

$$|T(\mathbf{Q})|^2 + |R(\mathbf{Q})|^2 = 1. \tag{5.5}$$

At this point the theoretical transmitted wave is a complex function whose phase is used to fit our experimental results (Fig. 5.12.b). It is worth noticing that the fitting is not consistent with the last three points of the phase shift curve. This mismatch with the analytical calculations is given by the fact that the sample was drifting from its original position and this negatively affected our reconstructions at the last three angular positions.

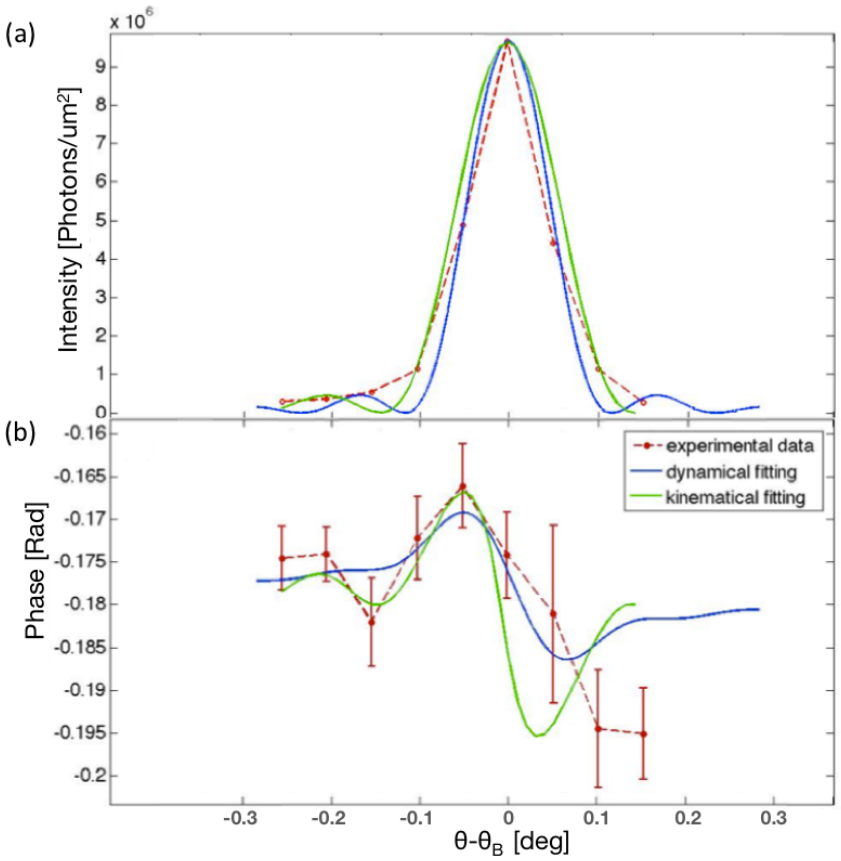

Figure 5.12: (a) Rocking curve of diffracted intensity and (b) transmitted phase shift together with the kinematical and dynamical fit curves.

This result shows a measurable phase shift even close to the kinematical limit. It is possible to see that the phase of the structure factor of a finite crystal varies across the rocking curve and this causes an angle-dependent phase shift in the transmitted beam also.

Another important issue that must be taken into account when retrieving the phase shift is that we can have an additional contribution to the phase in correspondence with the coordinate reference system chosen to identify the crystal structure. This effect can be easily pictured if we consider a simple two dimensional lattice where single atoms are equally spaced at all planes. The unit cell origin can be chosen arbitrary, but the way atoms are arranged within the cell itself can affect the phase of the diffracted beam according to the structure factor. If for instance the cell is chosen so that the atoms are located at its exact edges, then the additional phase contribute will be zero. On the contrary, if the unit cell origin lies between the planes the additional phase contribution will be π. Taking this effect into account in the fitting we have concluded that in our case the additional phase contribution was zero.

To compare the experimental results with theoretical predictions we performed simulations using the dynamical theory of X-ray diffraction [6]. In our model we assumed an incident radiation as a plane wave with 8.7 keV of photon energy and considered our object as an infinite 100 nm thick crystalline plate made of gold. The crystalline planes were inclined by 18° to the surface, which corresponds to the case of orthogonal incidence for selected {111} reflection. The complex wave field on the exit surface of the crystal was obtained by two approaches based on dynamical theory of X-ray diffraction. In the first one Takagi-Taupin equations [72] were solved numerically on a two-dimensional integration network [73], in the second one an analytical solution based on Green functions approach [74] was used. The complex diffracted and transmitted amplitudes for different angle deviations from the Bragg condition were obtained by these two methods as shown in Figure 5.12.a,b. Results of both approaches were consistent with each other. The rocking curve which is shown in Figure 5.12.a has a form of a sync-function that corresponds to the kinematical limit of dynamical diffraction. In Figure 5.12.b an angular dependence of the phase of the transmitted wave is presented. This curve reveals small variations from the constant refraction phase shift of 0.18 rad which are clearly visible. These variations about 0.016 rad in total originate from coupling between the transmitted and diffracted amplitudes.

Using a ptychographic approach [49] we have measured how the phase of an X-ray beam transmitted through a thin crystal changes when a diffracted beam is generated inside the crystal. The observed phase change is found to agree with both a quasi-kinematical model and the full dynamical theory of diffraction, evaluated numerically for the specific sample thickness. For the case we considered, the phase change follows a derivative lineshape, advanced on one side of the rocking curve and retarded

on the other. An off-axis {111} Bragg peak was used for the measurement for which the phase of the structure factor is zero, with the appropriate choice of unit cell origin. If a structure with more than one atom per primitive unit cell were measured the phase of its complex structure factor would also shift the phase of the reflected beam. Calculations (not shown) show that the asymmetry of the derivative line shape becomes reduced or reversed in this situation. It will therefore be possible to extract the phase of the structure factor directly from the profile of the transmitted phase.

This work also demonstrates the high accuracy of the phase that can be measured using the ptychography approach. This quality arises directly from the high coherence of the X-ray beam used. The beam traversing the crystal is coherently mixed with the beam that passes around it, resulting in a deviation of the diffracted beam. The pattern of these deviations is reconstructed as a phase image self-consistent for all positions of the sample probed by scanning and the resulting phase is very accurate.

Chapter 6

Design and preparation of new samples

After being encouraged by our results on gold nanocrystals, we decided to continue our investigations on other samples whose structural properties would have made it easier to see phase shift effects. We decided to use different crystals, Si and InP, and to design the new samples in a different way. In particular we wanted the new samples to be easy to use so we worked on a design which would have helped in implementing the experiment. The following step was, of course, to materially produce them. In this section both creative processes will be presented showing how we got from the paper design to the real samples.

6.1 Sample's design

The first samples that we worked on were the Si ones and we started from a 110 monoscristalline wafer. The starting idea for our samples was to obtain crystalline pillars by etching the wafer. Furthermore, because we wanted to observe the Bragg condition relative to the {111} plane of Si, we prepared our pillars in such a way that a beam almost perpendicular to the pillars' facets would have been able to easily reach the requested angle. It is worth noticing that for the 110 wafer, both transmitted and {111} Bragg reflected beams lie in the same plane as the wafer itself. A graphic representation of this design is shown below in Fig. 6.1.

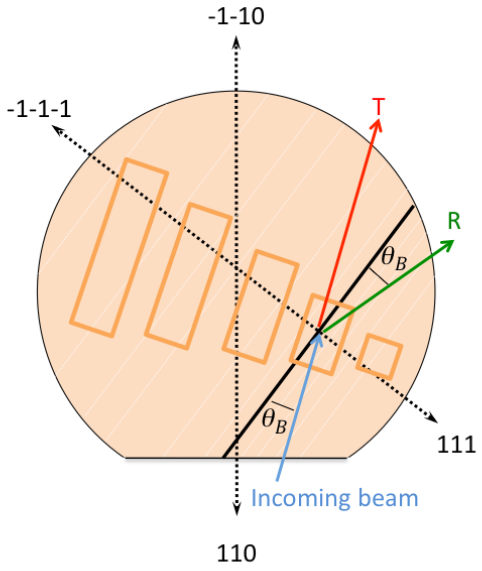

Figure 6.1: Schematic representation of our design. After identifying the {111} crystallographic direction, we considered its perpendicular set of planes (black bold line and white lines). In order to simplify the experimental setup, we cut a series of pillars (orange rectangles-top view) in such a way that the incoming beam at the Bragg angle (blue arrow) would alreadybe perpendicular to the pillars' facets. Θ_B represents the Bragg angle.

In order to define the orientation angle of our pillars we calculated the position of the {111} plane respect to the {110} direction using the geometrial formula

$$cos\phi = \mathbf{V}_1 \cdot \mathbf{V}_2$$
$$\phi = cos^{-1}\left(\frac{\mathbf{V_1}\cdot\mathbf{V_2}}{|\mathbf{V_1}|\cdot|\mathbf{V_2}|}\right) \tag{6.1}$$

where $\mathbf{V_1} = 1\mathbf{x}+1\mathbf{y}+0\mathbf{z}$ and $\mathbf{V_2} = 1\mathbf{x}+1\mathbf{y}+1\mathbf{z}$ so that the resulting angle between the two directions was of 35.26 degrees. At this point it was necessary to determine the Bragg angle for the {111} reflection and in order to do so we needed to also take into account the energy that we were planning to use during our experiments. We estimated that the resulting {111} Bragg angle at the energy of 8.7 Kev was of around 13 degrees. By combining these two angles, we determined the inclination for our pillars which resulted in 12 degrees respect to the {110} normal direction.

The single sample consisted on a silicon support with a set of equally spaced Si pillars at the top, all with different thicknesses (from 2 up to 32 microns) but same width (4 microns) chosen to match the piezo scan range. The reason for including a series of differently sized pillars was to observe how the

phase shift changed with the sample's thickness. Because the pillars were of much smaller dimentions respect to the size of the whole wafer, we cut the wafer into equally sized squares and replicated the design several times. Also, within the same piece of wafer, we replicated the series of pillars in order to have a backup in case of damages. The whole concept of our design is shown in Figure 6.2.

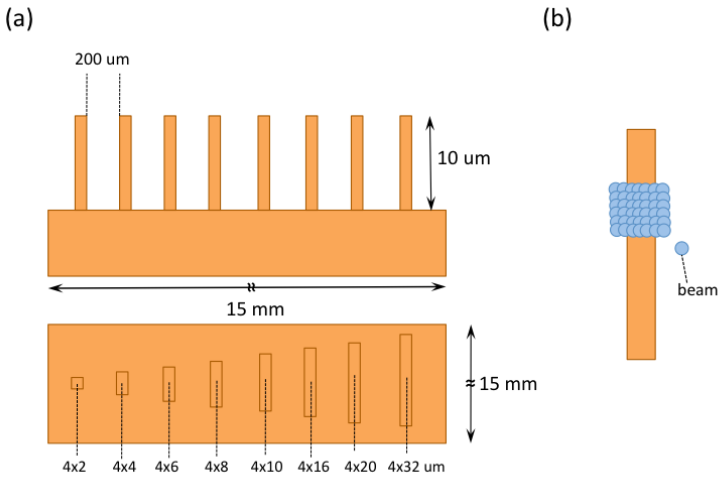

Figure 6.2: Lateral and top views of our samples. (a) We designed a set of Si pillars with same height (10 microns) and lateral profile (4 microns) but different thickness (from 2 up to 32 microns). The 15×15 mm dimensions refer to the size of the mask that we used to draw the pillars. On each sample we replicated the pillars series several times in order to have a backup from production defects or eventual damages during the experiment. (b) Here is an example of how to perform a ptychographic acquisition of a single pillar.

The resulting design can be described as a comb whose teeth are of same width but of different thicknesses. The idea that we wanted to implement was to have a sample which, mounted perpendicular to the X-ray beam, would have allowed us to easily find the Bragg relection and to change the position on the sample by moving from one pillar to aonther by simply shifting in one direction. The ptychographic acquisitions was to be perfomed on a single pillar at once, by illuminating its facet and collecting the resulting diffraction pattern in the far field.

A similar design was also used for the InP samples with the difference that in this case we used a 100 wafer with the idea of perfoming the experiment by collecting diffraction patterns from three distinct reflections coming from the {111}, {220} and {222} planes. In this case we decided to incline the pillars by 17 degrees respect to the {100} direction, but bearing in mind that the execution of this

experiment would have requested a change in the setup for each reflection.

6.2 Clean room production

The first step in preparing the sample was to cut the wafer into squares of equal sizes. The reason for doing so was to have a number of backup samples, mostly justified by the fact that the etching process that we wanted to use to cut our pillars is difficult to control. On one side we were not totally sure about how to set the etching time and having a number of spare samples would have allowed us to make few tries. What we wanted to achieve was to etch pillars 10 microns tall out of the substrate and the risk was of either etching too much, thus distroying the sample, or not enough having too short pillars. Having an height of around 10 microns was important for us because our idea was to perform ptychographic acquisitions close to the top of the pillars, staying far from the support so to avoid reflections that would have affected the diffraction patterns. Another reason for having more samples was that, even after setting the correct etching time, it usually happens that different samples put together inside the etching chamber will be etched in a different way because the flux of the etching gas is not perfectly homogeneous.

In order to produce our samples we used the clean room facilities available at the London Centre for Nanotechnology (LCN) which were easily accessible for us. The machine used to cut the wafer consisted in a vacuum chamber where the sample had to be mounted on a magnetic support. The magnets and the vacuum were used to secure the sample so to avoid movements that could have affected the precision of the cut. The whole system was software assisted so that we could easily decide the size of our squares, which in the end were of around 1×1 centimeters, as shown below in Figure 6.3.b. After cutting the wafer, another very important thing was to remember the orientation of the wafer for each square. As shown in Figure 6.3 as well as in the previous drawings, the orientation of the wafer was identified by a cut on one side of the wafer itself, so before disassembling the original wafer we marked each square to remember were the $\{110\}$ direction was.

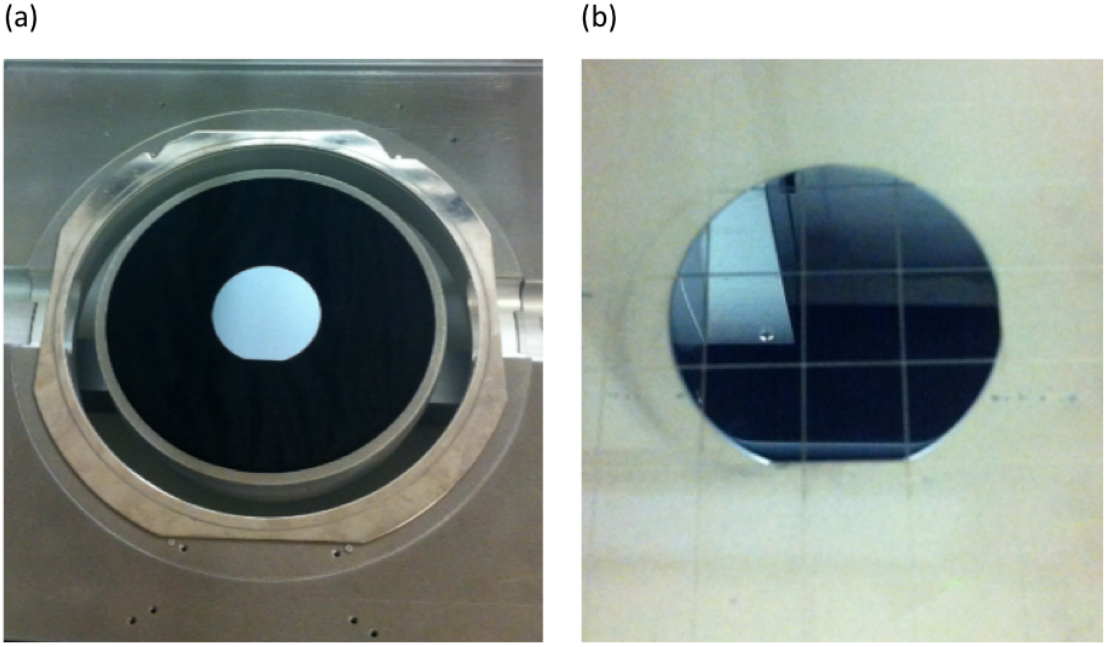

Figure 6.3: Starting point of the sample's preparation. (a) The 110 Si wafer is mounted on a support and inserted in a vacuum chamber where a compressed air saw will cut it into squares. (b) The resulting squares of 1×1 cm.

The following step in our production process was to prepare the squares for the electron-beam lithography, which would have allowed us to draw the masks that we wanted to use for our pillars. After removing the marked squares from the support we washed them with acetone and then we let them dry on a hot plate. At this point we were ready to put the e-beam resist on each square. In order to make sure that is was uniformly distributed on the samples' surface, we used a machine called spin coater, where the samples were processed once at a time. Spin coating is a commonly used practice to achieve high-precision lithography. It consists on rotating the sample so that the interaction between the viscous and centrifugal forces permit to obtain a uniform photoresist film of controllable and reproducible thickness. By using the spinner for the same amount of time for each square, we were sure to have the same photoresist coating on all samples.

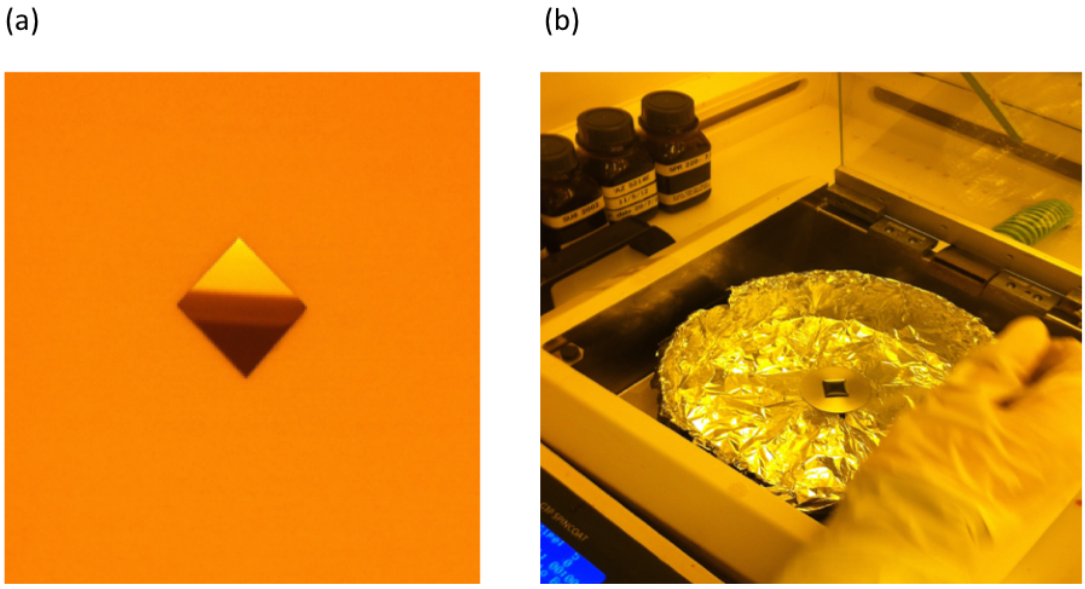

Figure 6.4: Photoresist deposition. (a) A single square obtained from the Si wafer. (b) E-beam resist deposition with the use of a spin coater.

After this stage we were finally ready to implement our design by using the e-beam lithography. This system operates by using a focused electrons beam which scans the sample and allows to draw custom shapes by interacting with the electron sensitive resist. Again, it is a software assisted procedure where the user interface allows to navigate the various samples mounted on the support in order to decide where, on each sample, to draw the masks pattern. In order to better visualize the pillars, we also decided to include a cross shaped mark of around 150 microns. Next to this cross we drew on a line the series of equally spaced pillars as shown in Figure 6.2.a. After processing the samples with the e-beam we had to develop the resist with a solvent whose purpose was to keep the masks exposed to the electrons beam, while dissolving the rest of the coating. This step was done separately for each Si square by washing the pieces in the hot solvent at a temperature of around 80 degrees for approximately 40 seconds. After developing the samples we dried them out with a hot plate and then we checked on the optical microscope the presence of the masks. These steps are illustated below in Figure 6.5.

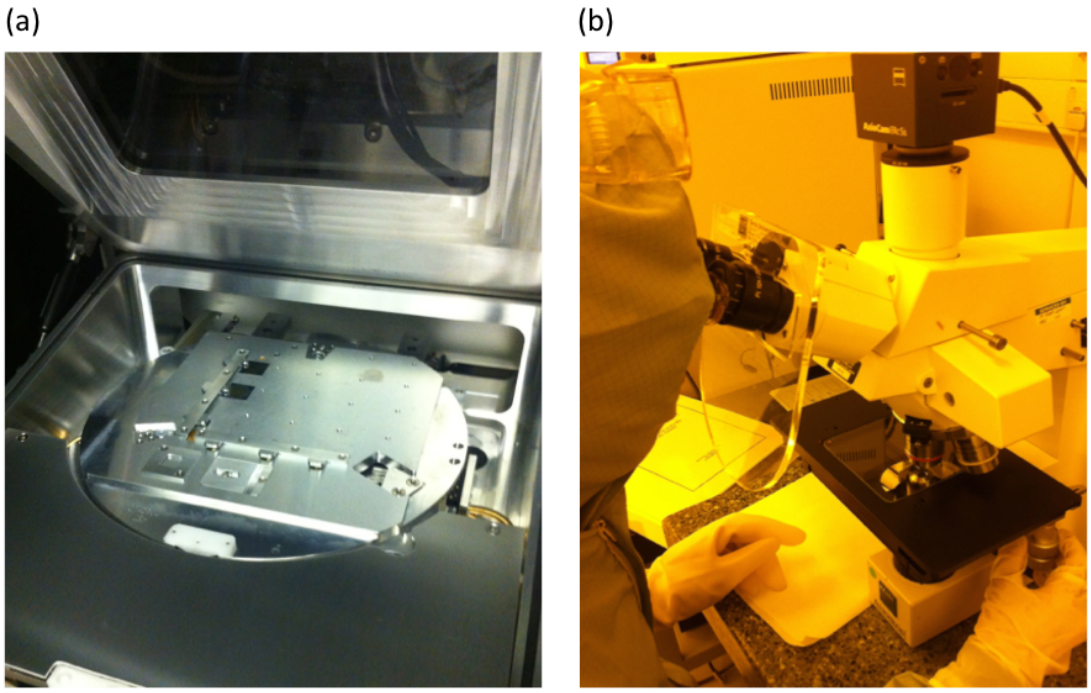

Figure 6.5: (a) Samples mounted in the e-beam system support. (b) After developing the processed photoresist, we checked the masks with an optical microscope.

At this point we were finally ready for the last step: the plasma etching. In this part of the production process we used a machine which used a high speed flow of appropriate gas to attack the exposed silicon substrate in order to obtain our pillars. The masks impressed on the surface allowed to preserve the shape of our pillars but the choice of the appropriate etching recipe, to be used for the correct amount of etching time, was of primary importance. As illustrated in Figure 6.6.a, the etching process itself is too aggressive and by only using it to process our samples we would have ended up with pyramid shaped pillars, this meaning that the masks would not have been able to endure for the whole etching period. Instead, in order to protect the masks and obtain the block-shaped pillars, we combined the deposition of C_4F_8 with SF_6 etching cycles.

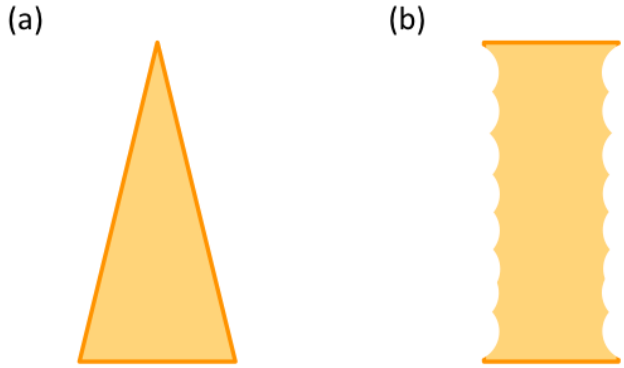

Figure 6.6: Etching process. (a) Etching itstelf is extremely aggressive so that the masks would not be able to persist. (b) If we combine depostion and etching, we can control the shape of the sample. Each etching cycle is visible on the pillar's edges and for our recipe of SF_6we estimated a 0.1-0.5 microns etch per cycle.

In developing the InP samples we had to modify the etching recipe and this proved to be a not so easy step since we did not have any previous experience in etching this material. We chose to process the samples by having steps of O_2 deposition followed by CH_4 /H_2 etching cycles, also trying different etching times, starting from 30 minutes up to 2 hours. The result gave us pillars 11 microns tall after etching for 30 minutes. As shown below in Figure 6.7c the InP etching was more difficult and as a result we had a massive presence of debris all over the sample when the processing time was too long. We compared samples obtained at different etching times, from 30 minutes up to 2 hours and we could see that after 30 minutes we had debris covering the surface of our samples, while after 1 hour we started losing the shape of our structures.

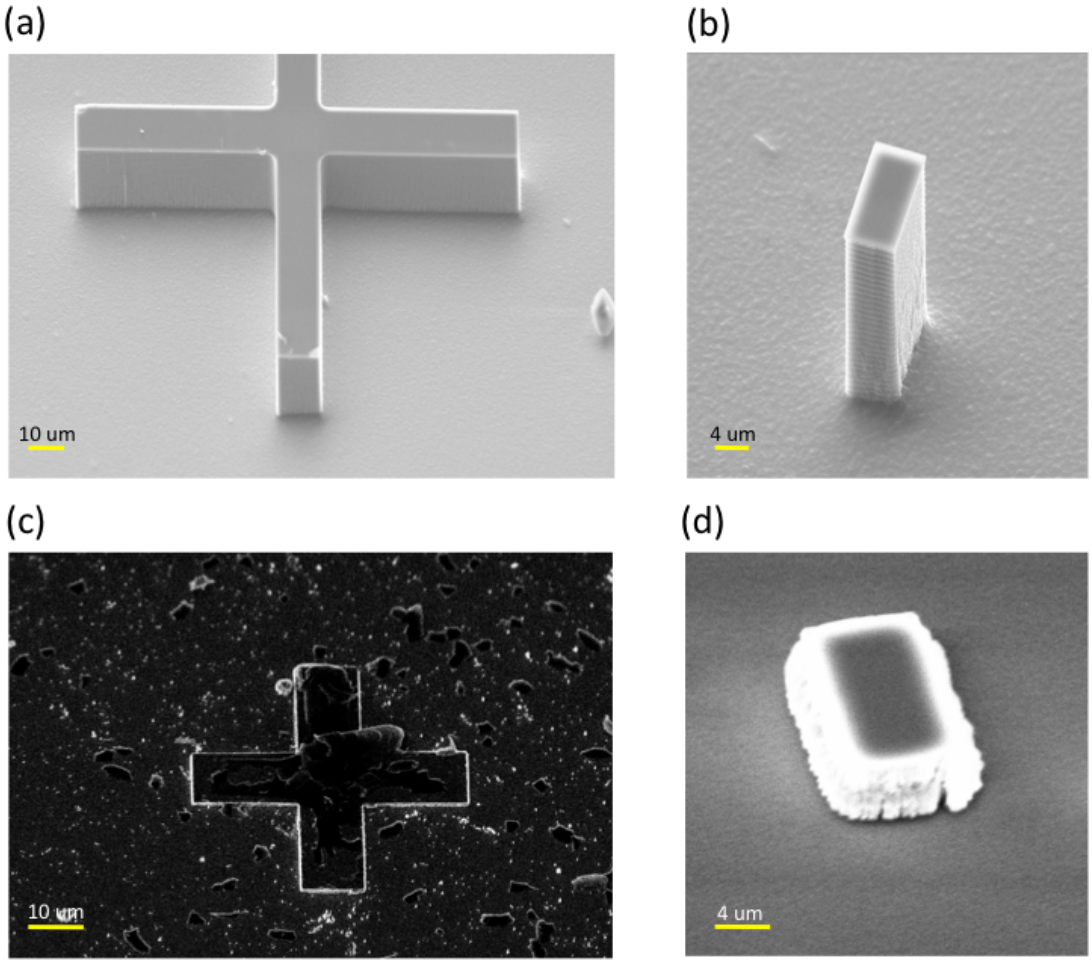

Figure 6.7: Etching results. a) and b) refer to the Si sample, while c) and d) show the result for the InP samples. c) For etching times longer than 30 minutes, the samples were full of debris. We saw that after one hour we completely lost the shape of our samples as a consequence of a too aggressive etching. d) InP pillar obtained after 30 minutes. By comparing it with b) we can see how the InP etching process was more difficult to control, as the shape of the pillar is less precise.

Chapter 7

Si and InP: experimental results

The experiments on the new samples were conducted at the 34ID-C beamline of the Advanced Photon Source (APS) facility at the Argonne National Labs in Illinois, USA. We performed our experiments separately, visiting the facility twice in November 2013 and April 2014[1]. In order to adapt our experiment to a beamline different from the one used for gold nanocrystals, we had to change the setup. In particular we did not use Fresnel Zone Plates to foucus our beam, but KB mirrors which are a more common setup for that beamline. At APS the white beam horizontal slit is located 27.5m away from the hutch, acting as a secondary source set to 150um to define the coherence as explained in [75]. Inside the experimental chamber we had the coherence-defining JJ slits whose aperture was adjusted several times during the experiments in accordance with the samples' thicknesses. Figure 7.1 shows the part of the setup which controls the beam size. The focus size for a coherent beam is diffraction-limited by the JJ entrance slits width d, as $f_{size} = \lambda D/d$ where. focusing point can be obtained through geometric considerations and in particular the angle ψ is obtained by combining the JJ slits aperture d and the distance D' between the pinhole and the focal point as $\psi = d/D'$.

[1] For future references the data were collected under the names UCL1113 and UCL414b, respectively.

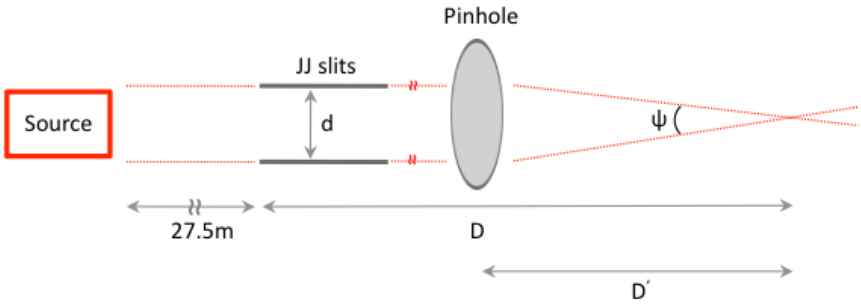

Figure 7.1: Experimental setup: lateral view. This first part of the setup that we used controlled the beam size. The source is 27.5m away from the sample and the associated optics, where the longitudinal coherence is set through another set of slits of 150 microns aperture. The JJ slits are used to modity the aperture d, so that the angle ψ will change accordingly. For the sake of an easy representation this sketch does not show the sample, but of course in our setup it was positioned in correspondence of the focal point.

The JJ slits size was used to control the rocking curve obtained when performing scans at different angles, in total similarity with what we did in our previous experiment. In this case, as it will be described later, the rocking curves were measured using a scintillator detector which collected the beam reflected from the sample. In order to make sure that our acquisitions were correct, before performing the complete set of ptychographic scans, we checked the rocking curve which had to be symmetric and well sized. In particular, as showed below in Figure 7.2, theoretically the width of the rocking curve changes with the sample's thickness. In our experiment we adjusted the JJ slits size in the horizontal direction so that the angular spread of the rocking curve would have been bigger than ψ. In these cases, after properly adjusting the JJ slits, we could record the correct rocking curves which in most cases also showed the lateral lobes.

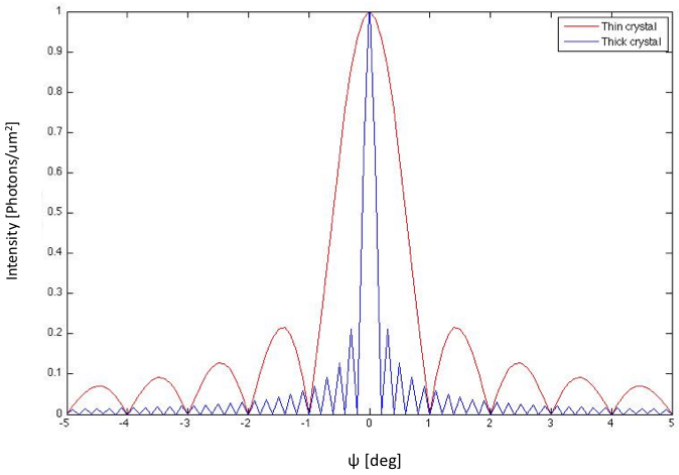

Figure 7.2: Rocking curves. Here we present the theoretical rocking curves whose angular spreads vary with the sample's thicknesses. The angle corresponding to the highest intensity is the one that satisfies the Bragg condition.

7.1 Si samples

The complete setup schematic representation is shown in Figure 7.3. After the KB mirrors block we used a 40 microns pinhole positioned 2.8cm downstream. We then mounted our sample on a 3D piezo stage, positioned 3.5cm away from the pinhole, where the silicon pieces were attached flat to the support. The idea was to have the beam parallel to the support, hitting the pillars perpendicularly to their facets. The beam size was of approximately 1 micron at the energy of 7.4 KeV. Behind the sample's stage we had a scintillator inclined by approximately 30 degrees in the horizontal plane, as shown later in figures 7.3 and 7.13a . This device was used in a similar way to the Pilatus 100K detector which was part of our setup during the gold nanocystals experiment. Before starting any set of ptychographic scans, in order to get the correct Bragg angle position we defined a range of angles and then rotated the sample accordingly. We then illuminated the sample moving at all angles and we measured the reflected beam intensity collected by the scintillator. The result of this acquisition showed the rocking curve, where the correct position of the Bragg angle corresponded to the highest intensity.

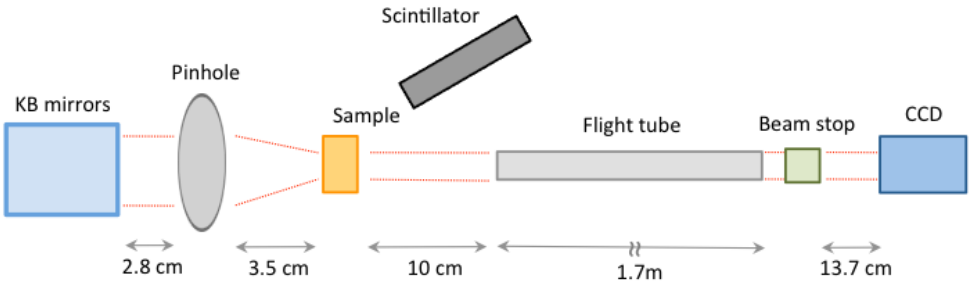

Figure 7.3: Top view scheme of the setup. The scintillator was coplanar with the sample stage and was positioned at an angle of around 30 degrees. In order to attenuate the scintillator's photons counts, so to prevent damages, we used aluminum foils which we had to add or remove manually. In this schematic representation the beam direction is assumed from left to right.

Downstream of the sample we used a 1.7m flight tube to reduce air scattering and then a 1x1mm^2 beamstop which partally blocked the direct beam that had not been diffracted by the sample, so to protect the detector from damages. The diffraction patterns were then collected using a Medipix detector with a single module of 256x256 pixels of 55 microns size.

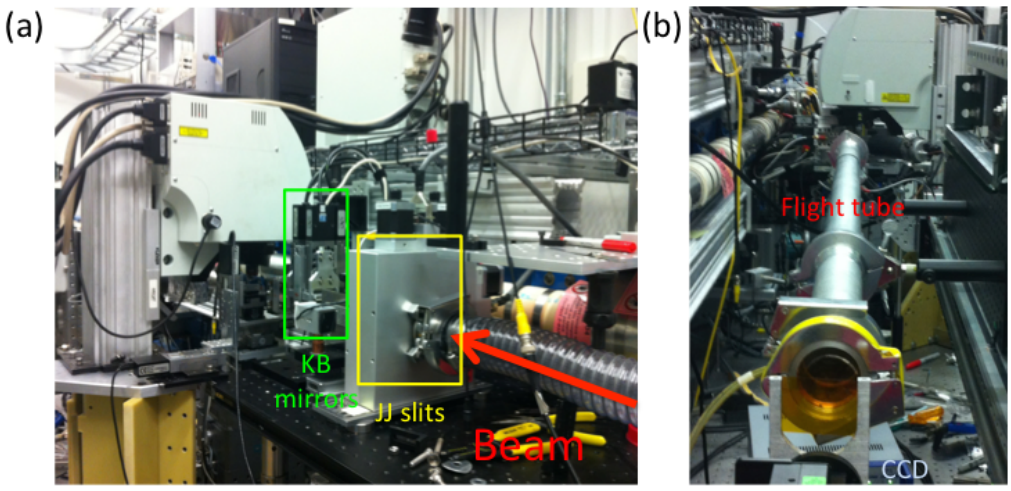

Figure 7.4: Photos from the beamline. (a) shows the portion of the setup upstream the sample while (b) is the downstream section.

Before using our Si samples, we performed several ptychographic acquisitions on a test pattern in

order to retrieve the probe. Once obtained a good illumination function, we mounted the Si sample and performed our experiments. During the data analysis step, we used the probe retrieved with the test pattern as an initial probe guess for our reconstructions. It is worth noticing that the beam can not be considered as stable during the whole beamtime. For this reason we had to move back to the test pattern and measure again the probe few times during the whole experiment. This step was necessary in order to use the correct probe for reconstructions of data acquired at different times during the experiment.

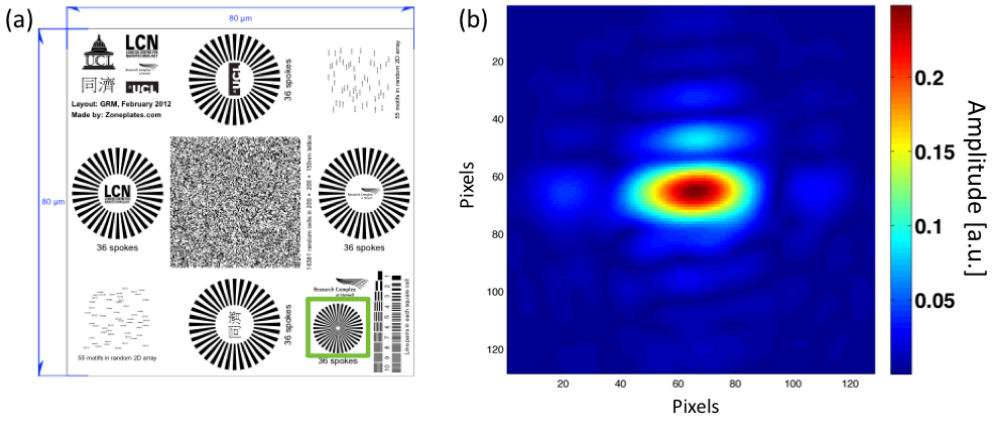

Figure 7.5: (a) Test sample layout, where the green square shows the 36 spokes siemens star that we used as test pattern. (b) Amplitude of the reconstructed probe obtained from the test pattern.

By following the same approach used in Chapter 5, one can have a precise estimate of the beam size starting from the amplitude of the reconstructed probe. In particular one can derive the linear profile of the probe's intensity and measure its FWHM which in this case corresponds to 50 pixels, as shown below in Figure 7.6. At this point, by applying the well known equation $pix_{sample} = (\lambda z)/(npix_{det})$ one can obtain that the pixels sixe at the sample's stage is of around 22nm[2]. By multiplying the pixel size by the FWHM one obtains 1.1micron which is consistent with what was previously stated.

[2]The values used in this formula are: n = 256 pixels, pix_{det} = 55microns, z = 1.93m and λ = 1.675Å.

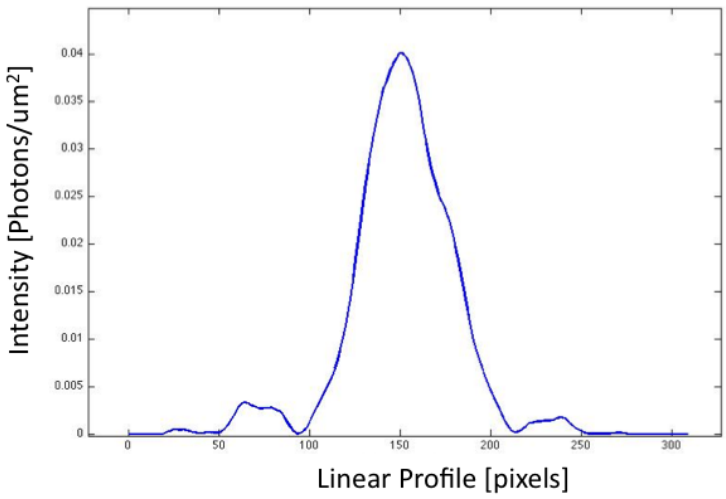

Figure 7.6: Probe intensity: linear profile.

Another aspect that it is worth highlighting is the shape of this probe which is different from what we showed in Chaper 5 for the gold nanocrystals experiment. In that case, as pictured in Figure 5.2, the probe was round shape while here we have a square shape. The explanation for this difference is given by the different setups used in the two experiments: the FZP gives the round shape, while the JJ slits-KB mirrors cascade results in a square probe. Because we could adjust the JJ slits aperture we could also see that the probe's size also changed accordingly as shown below in the schematic representation in Figure 7.7.

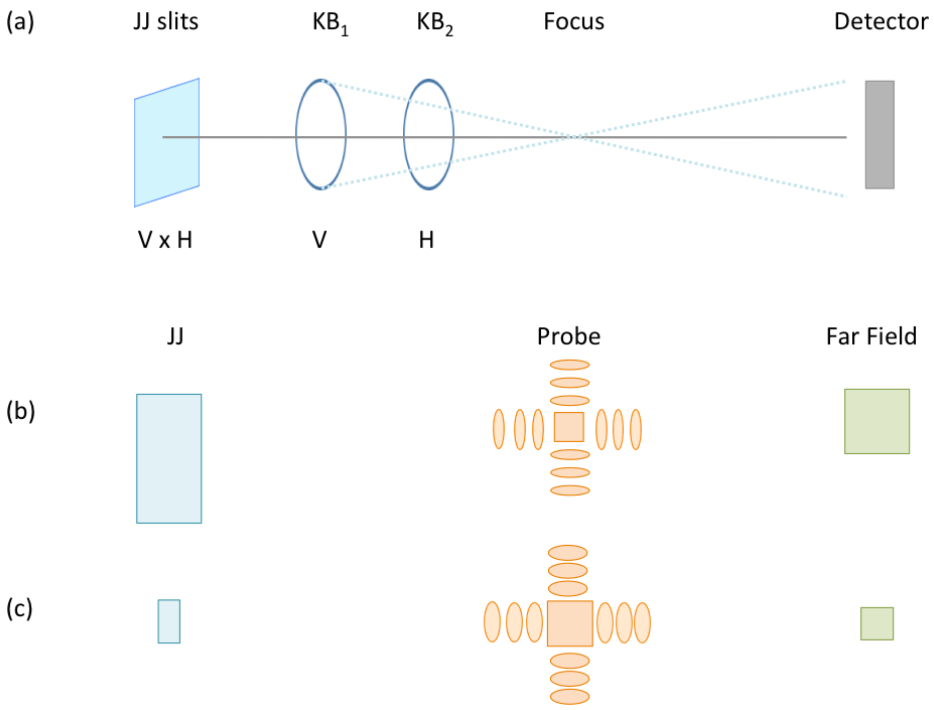

Figure 7.7: The JJ slits - KB mirrors cascade. (a) This schematic representation shows that the JJ slits aperture is set with a couple of values for the horizontal and vertical dimensions. Typical values are 30x60microns^2 (HxV) so to have a rectangular aperture. The KB mirrors cascade is represented with two lenses of different focal lenghts, where the first lens KB_1defines the vertical dimension while KB_2 defines the horizontal one. The typical focal lenghts are 220mm for KB_1 and 110mm for KB_2. This 2:1 ratio has the effect of modifying the shape of the probe which results squared. (b) Starting from a 30x60microns^2 (HxV) JJ slits aperture we obtain a square probe and then a square pattern in the far field. (c) Starting from a 20x10microns^{2}JJ slits aperture we have once again square probe and diffraction patterns in the far field, but the size will change respect to case (b) as shown in the scheme.

7.1.1 Si pillar: 4x4 microns

In this section experimental results for the 4x4x10 microns^3 Si pillar will be presented. In the next section similar results will be discussed for the 4x8x10 microns^3 pillar so to compare what happens at different thicknesses. For both acquisitions we set our JJ slits apertures to 10x60microns^2 (HxV).

In performing this experiment we tried to improve our fitting results and for this reason we performed a larger set of scans on and off the Bragg angle. In complete analogy to what we did for the gold naoncrystals, we made sure to center our scans around the Bragg angle which for this sample was the one correspondent to the {111} crystallographic plane. By following the well known Bragg's law,

one can calculate the theoretical Bragg angle for this configuration at the energy of 7.4 Kev, which results in 15.49 degrees. As discussed in the previous section, we used a scintillator in order to set the correct angular position of our acquisitions, which for this series corresponded to 7.987 degrees in the theta lab coordinates. This number will be shown in the following curves fittings at the end of this section.

As discussed in Chapter 5, the reconstructed pillars were affected by phase ramps and due to the large number of ptychographic scans that we performed for each series, we had to also correct drifts so to align all the reconstrucred pillars before calculating the phase shifts.

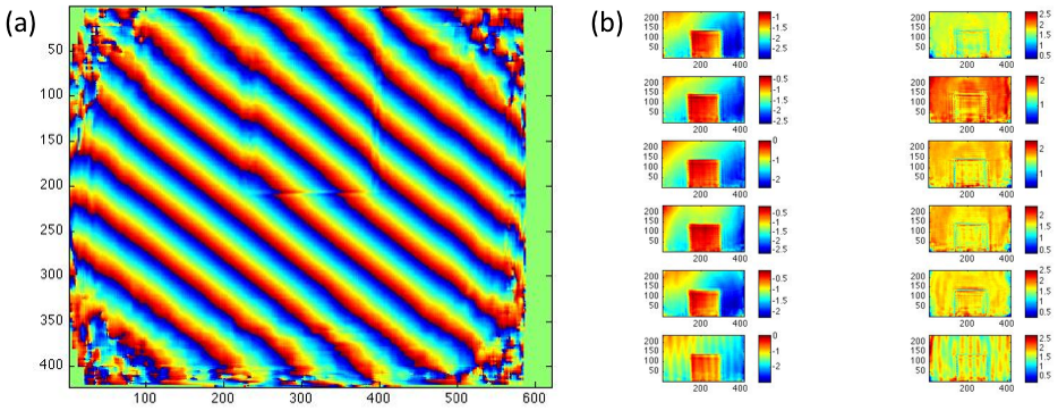

Figure 7.8: (a) Phase ramps affect the pillar's reconstruction. (b) Series of 6 scans, at different angles, after a first phase ramp removal step. The left column shows the phase, while the right presents the amplitudes. For both figures the values shown in both dimensions are pixel numbers.

As shown in Figure 7.8.b even after a first phase ramp removal step, the reconstructions were still affected by a residual ramp. In order to correct it we had to align the reconstructions and then run a second step of phase ramp removal by drawing custom masks around each pillar, as already discussed in Chapter 5.

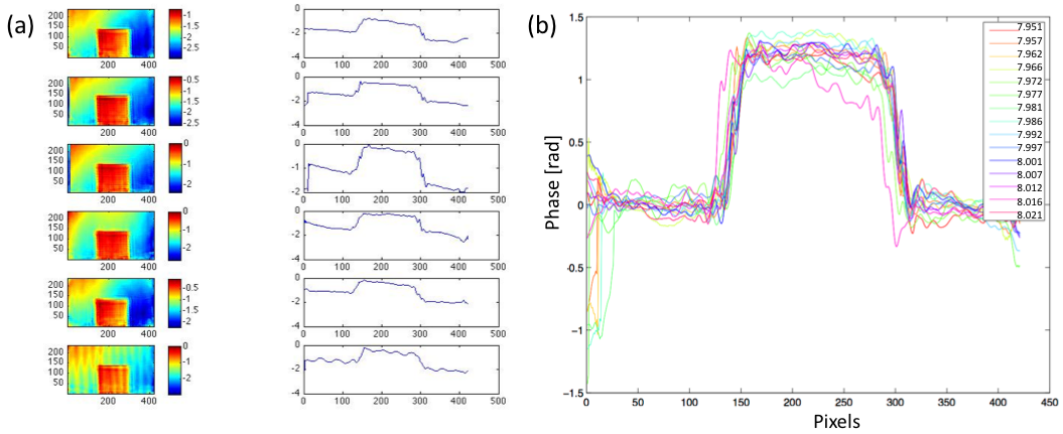

Figure 7.9: (a) Phase linear profiles before the final phase ramp removal, which is shown in (b). It is worth noticing that the total number of scans is 15, while figure (a) only shows the first 6 scans. The values in the legend are the angular lab coordinates of each scan. It is worth noticing that the reconstructed phase of the 6th scan shows stripes. This artifex will affect the final result as it will be discussed below. The last scan still shows a vertical ramp whose removal was particularly hard. The reason for this is that on the contrary to the gold nanocrystals case, the pillar can only have phase removal masks drawn on three sides (left, right and top of the pillar) instead of using the whole space surrounding it.

Once satisfied with the phase profiles we extracted the phase shift values by defining blocks inside and outside the pillar where we calculated the average phases. In this case we only had 4 boxes so that, for each angle, we could estimate the phase as

$$phase_{av} = phase_{av,c} - \frac{phase_{av,1} + phase_{av,2} + phase_{av,3}}{3}, \tag{7.1}$$

where $\text{phase}_{\text{av,c}}$ is the phase calculated in the box inside the pillar. At this point we could also extract the error-bars by taking into account the standard deviations ε_{i} of the phases calculated in each box, following the formula

$$\varepsilon_{tot} = \sqrt{\varepsilon_c^2 + \frac{1}{9}\varepsilon_1^2 + \frac{1}{9}\varepsilon_2^2 + \frac{1}{9}\varepsilon_3^2}. \tag{7.2}$$

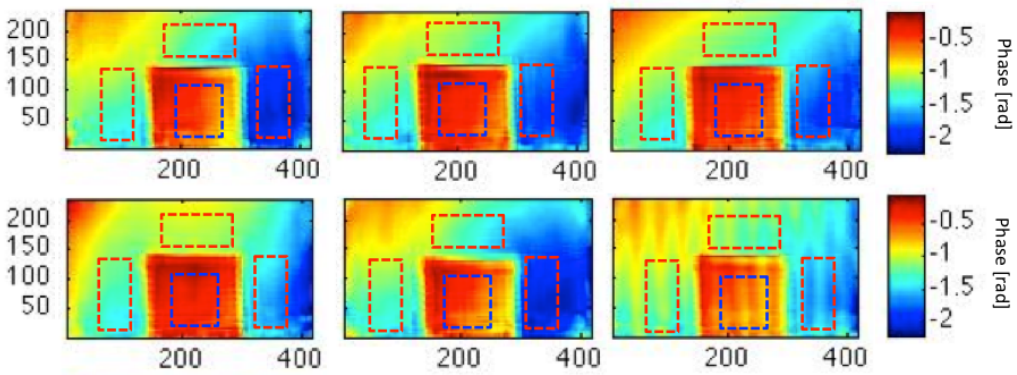

Figure 7.10: Boxes used to extract the average phase values for each scan. For simplicity here we show the boxes for the first 6 scans, but in our data analysis we extended this procedure to all scans in the series. The dotted red lines define the boxes outside the pillar, while the one inside is shown in blue. All boxes have the same number of pixels.

The result for the complete set of scans is shown below in Figure 7.11.

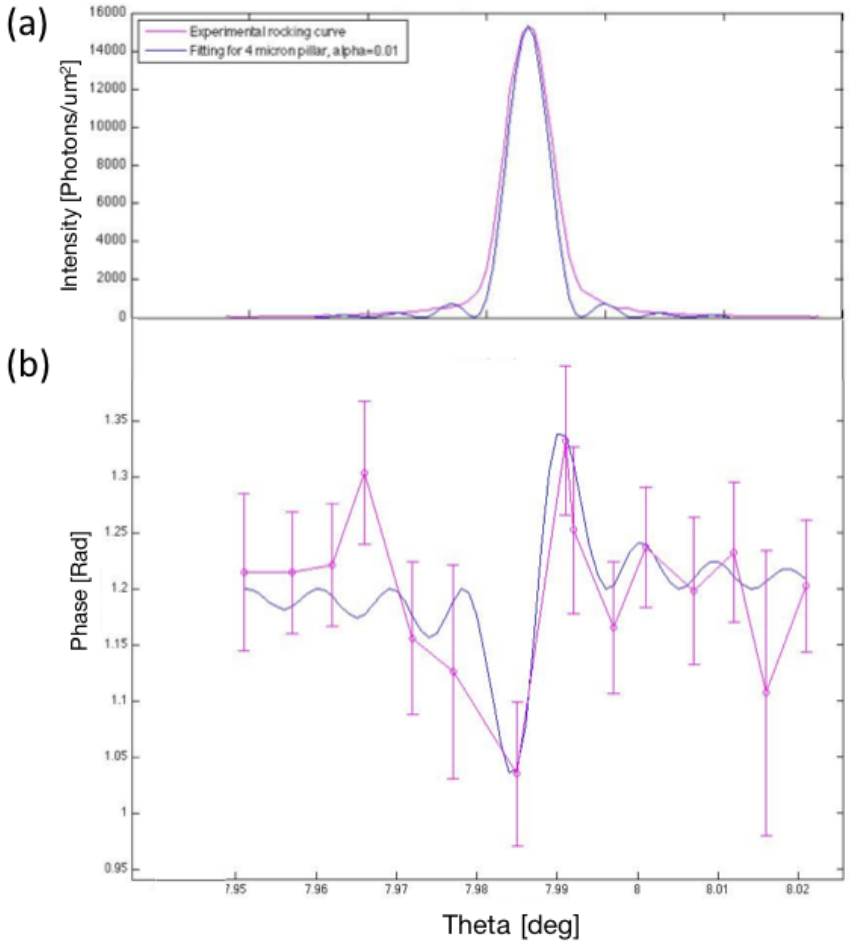

Figure 7.11: (a) Rocking curve and (b) phase shift fittings.

The fittings shown above were obtained using the kinematical approximations previously discussed in Chapter 5. The result shows a good fitting of the theoretical phase on the right side, while the initial scans don't seem to follow the theoretical curve. As previously anticipated, the 6th scan in the series is affected by artifects which could not be corrected, thus resulting in a large deviation from the theoretical curve.

7.1.2 Si pillar 4x8 micron

Our experiment continued with a set of ptychographic scans performed on a nearby Si pillar of same width (4 microns) but a larger thickness of 8 microns. We did not change the setup because we were still interested in the {111} reflection and also the probe and the beam size were, with a good approximation, the same. In conducting the data analysis we followed the same steps as above with similar intermediate results.

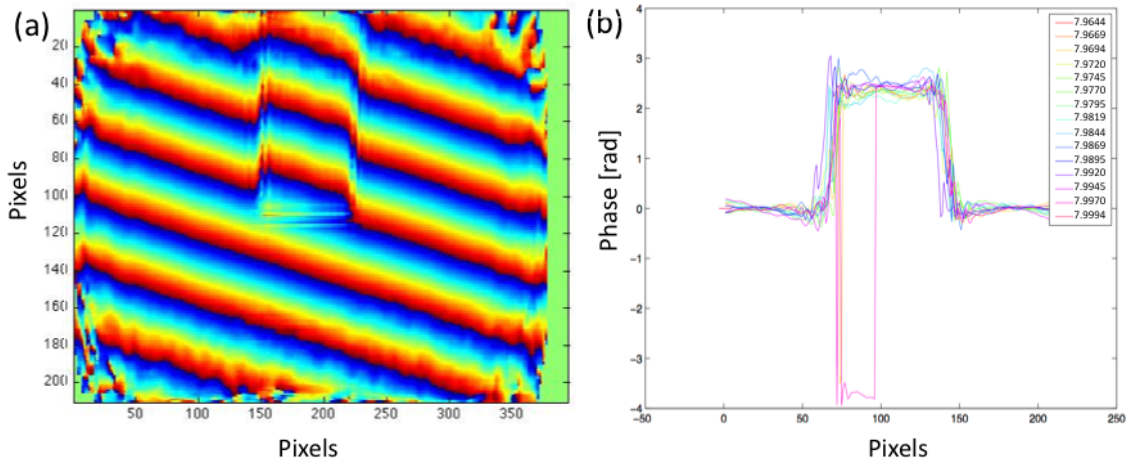

Figure 7.12: (a) Silicon pillar phase reconstruction before the phase ramp removal procedure. (b) Phase linear profiles. The values in the legend are the angular lab coordinates of each scan.

As one can notice from Figure 7.12.b, few reconstructions could not be corrected as they presented phase jumps and still residual ramps. In order to work on the theoretical fittings, we had to remove the faulty reconstructions and concentrate on the best ones. In this way we obtained the final fittings using 10 scans instead of 15. The final results for both rocking curve and are shown in Figure 7.13.

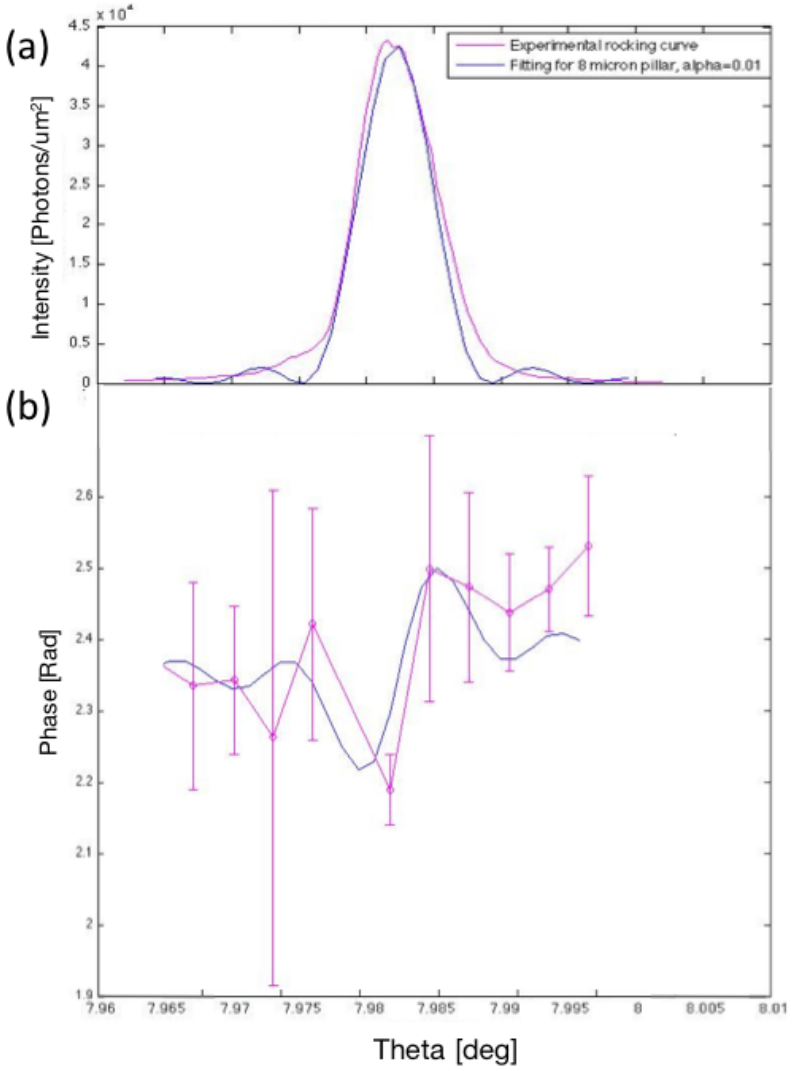

Figure 7.13: (a) Rocking curve and (b) phase shift fittings. The Bragg angle is at 7.983 degrees in the Theta lab coordinates.

In this case, while the rocking curve fitting is still good, the experimental results seem to follow the theoretical phase shift only around the Bragg angle. Off the Bragg condition we still have a good fitting on the right side because the experimental results follow the theoretical curve, despite having values higher than expected, while the left side is still not as good.

7.2 InP samples

We continued our investigation performing a similar experiment on InP pillars. As previously discussed in Chapter 6 the sample's layout is similar to the one used for the silicon wafer. We etched a 100 InP wafer and we modified the angular position of the pillars to 17 degrees with respect to the 100 normal. The main difference with the Si sample was that, while always having a set of different thicknesses for each pillar series, this time we also had 2 different lateral sizes: one of 4 microns and another of 6. In this section we will only present results for the 6 microns InP pillar of 4 microns thickness, but this time we will will refer to different Bragg reflections.

This experiment was once again performed at the 34ID-C beamline at APS, so for this reason the setup was the same that we used for the Si case, as shown in Figure 7.3. The only difference that we had to change the scintillator position because it had to be moved in accordance with the different reflections, as shown below in Figure 7.14.

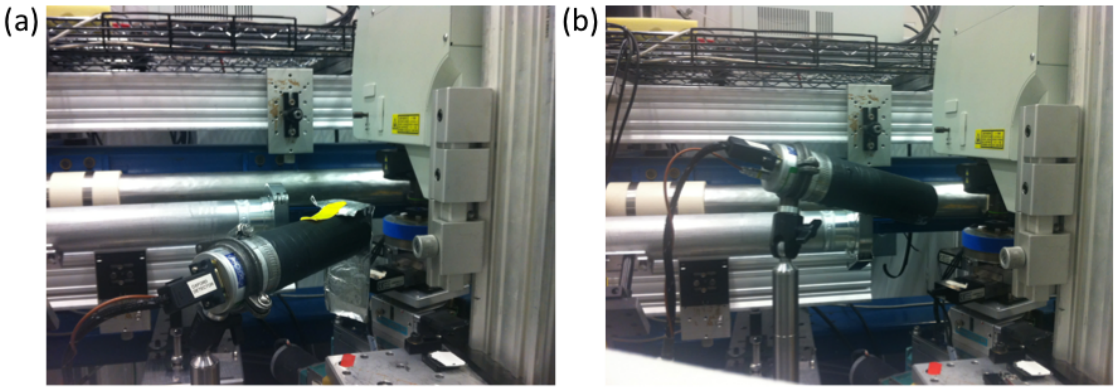

Figure 7.14: (a) Scintillator position for the 111 reflection. In this case we can see that the scintillator (black tube) lays on the sample's plane. (b) For the 200 reflection the scintillator is inclined respect to the sample's plane.

Before performing acquisitions on the InP sample we used again the test pattern in order to obtain a good probe to use in our recostructions. Because we also tried to used different JJ slits apertures, we performed acquisitions on the test pattern for each one of them. Once again we expected a beam size of around 1 micron but a more precise estimate could be obtained by analyzing the reconstructed probe, whose intensity is shown below in Figure 7.15.a.

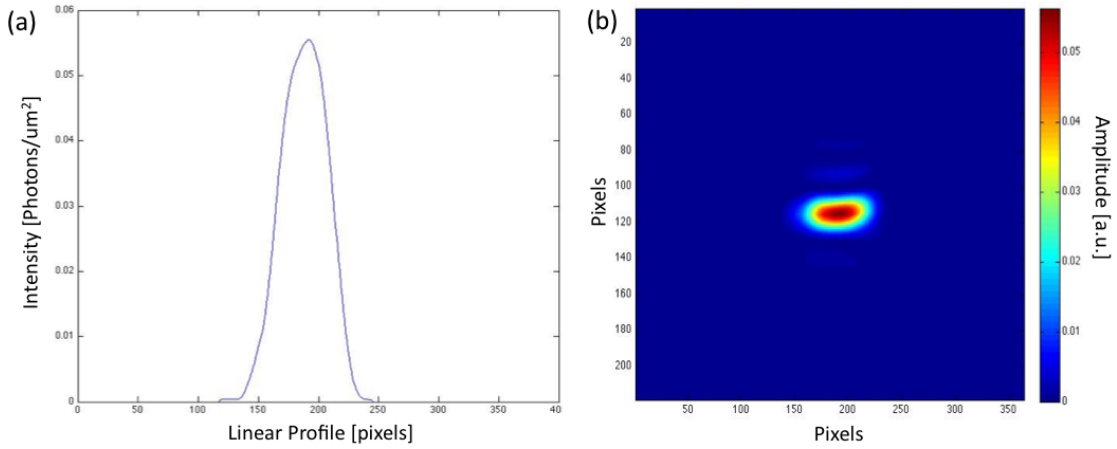

Figure 7.15: (a) Reconstructed probe's intensity linear profile and amplitude (b). The FWHM is of 50 pixels.

For this experiments we used an energy of around 9 KeV and by following the same procedure described in the previous section one can obtain a beam size of around 939 nm, which agrees with our expectations.

7.2.1 InP: {111} reflection

The first reflection that we wanted to analyze was the {111} because in this case the scintillator was laying on the sample's plane. The Bragg angle for this reflection is of around 11.66 degrees and the scintillator was placed at around twice this angle respect to the sample. Once again we used it in order to derive the precise position of the Bragg reflection and to define a set of angles around it. This device was once again used to compare the different rocking curve for a various sets of JJ slits aperture. In this case we set the JJ slits to 10x50 microns^2 (HxV). It is worth noticing that because our pillar was larger than the one analysed in the Si case (6 microns versus 4 microns for the Si), we had to perform much longer scans. This affected our reconstructions because as the scans took much longer to perform, we had considerable drifts, as shown below in Figure 7.16 which presents the phase reconstructions of the first and the last angular scans.

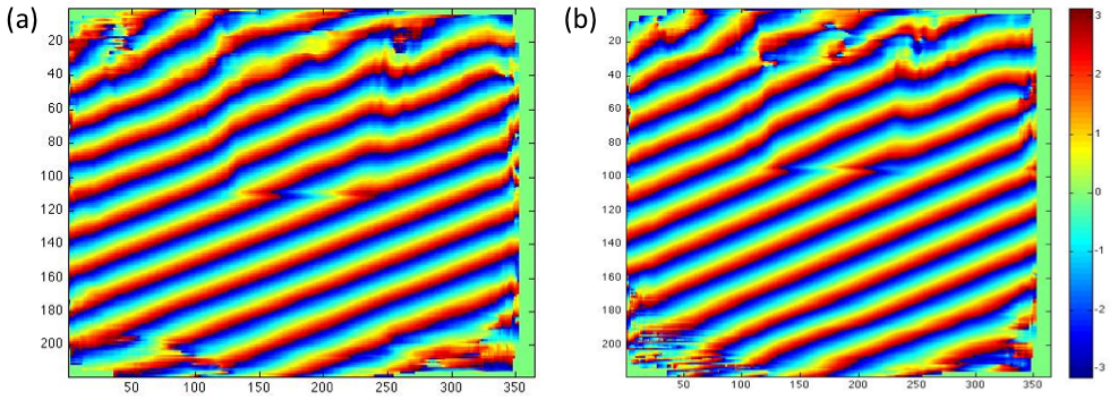

Figure 7.16: InP pillar reconstructions for the first (a) and last (b) angles of our series. One can notice that while performing ptychographic acquisitions for the complete set of angles around the Bragg, the sample moved consistently. The spatial coordinates are pixel numbers.

In order to be consistent with the data analysis and to be able to compare the results obtained for different angles, it was necessary to define the same region of interest for each scan. Because the sample drifted in downwards during the set of scans, we concentrated the analysis on the edge of the pillar. In total analogy with what we did for the Si samples, we corrected the phase ramps and we aligned the reconstruction in order to correct all drifts. The complete set of 9 scans is shown in Figure 7.17. A larger plot summarizing the phase profiles is presented in Figure 7.18. In this case the theta lab coordinate for the Bagg angle was 59.985 degrees.

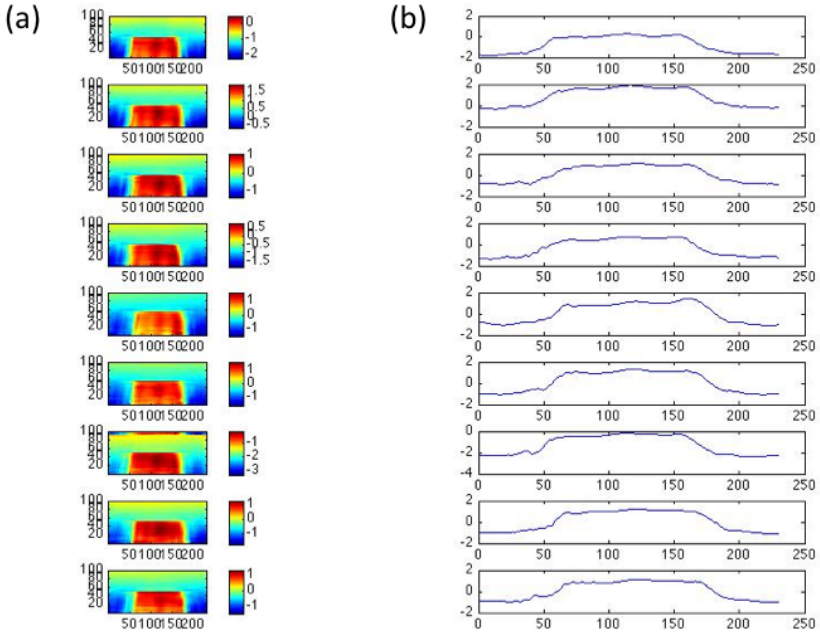

Figure 7.17: (a) Phase of the reconstructed pillar, corrected from phase ramps and shifts. One can notice that the region of interest has been considerably reduced respect to the complete field of view shown in Figure 7.16. (b) Linear phase profiles extracted for each phase reconstructions.

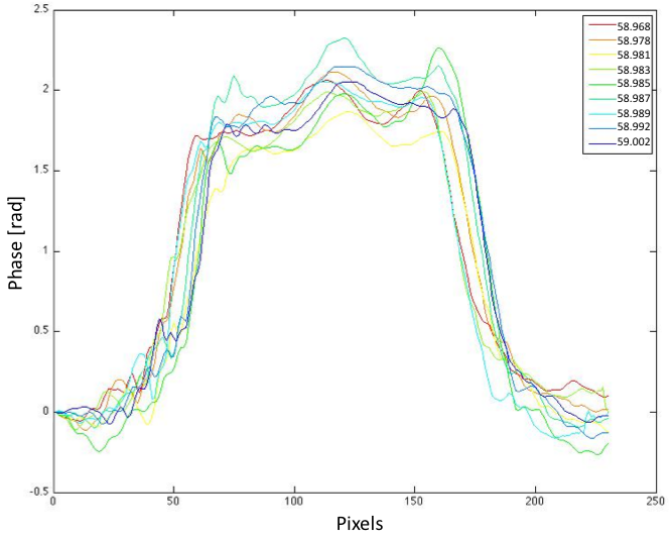

Figure 7.18: Phase profiles for different angles, showed in the legend. The Bragg position is at 59.985 degrees.

Contrary to what happened in the Si case, the phase profiles are not flat inside the crystal and also their width is different in few cases. This can maybe explained by the fact that the beam was fluctuating during the extremely long time of our acquisitions. We went on with the data analysis in total analogy with what we did for the Si case by drawing boxes of equal size, inside and outside the pillar, and by calculating the average phase and the error for each angle. The experimental results were then compared to the theoretical profiles obtained in the kinematical approximation, as shown in Figure 7.19.

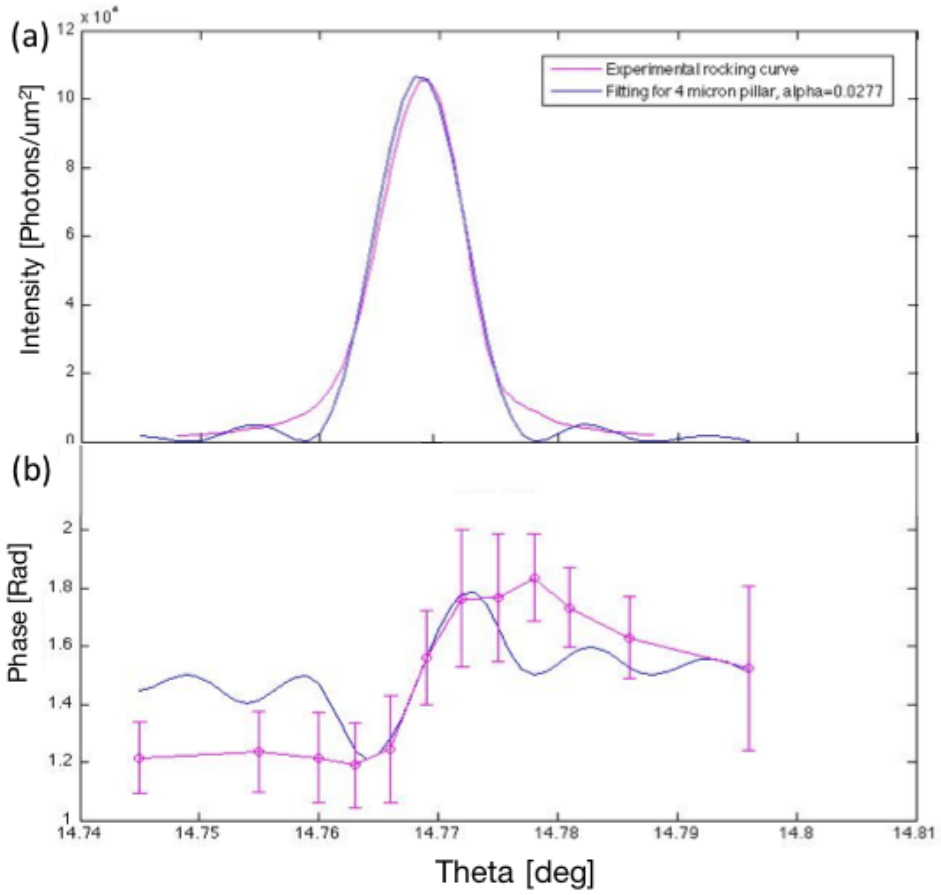

Figure 7.19: (a) Rocking curve and phase shift (b) fittings.

The phase fitting clearly shows very large errorbars which are consisting with the noise already

showed in the linear phase profiles. However it is worth noticing that the phase shift profile is symmetric respect to the Bragg angle. On the other side the rocking curve fitting is quite good, also showing side lobes.

7.2.2 InP: {220} reflection

In order to perform acquisitions of the {220} reflection we had to slightly modify our experimental setup by changing the scintillator inclination with respect to the samples's horizontal plane. As it is pictured below in Figure 7.20, the sample was designed in such a way that for the {111} reflection the beam (red arrow in the figure) only had to hit the pillar's surface perpendicularly.

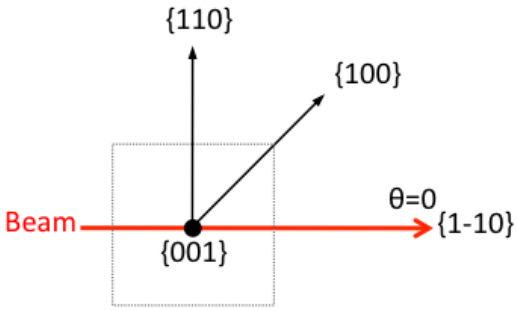

Figure 7.20: Top view of the sample layout. The pillars are designed in a way that the {111} reflection could be found by just hitting the pillar perpendicularly. For this reason, in this configuration, the scintillator lays on the sample's plane. When we wanted to collect other reflections we had to incline the scintillator at the appropriate ϑ angle. It is worth noticing that the {100} in plane direction is at 45 degrees.

In order to collect the {220} reflection, we had to change the ϑ angle from zero to the appropriate angle. The way we found it, was to first set the scintillator at twice the {220} Bragg angle, which at the energy of 9KeV is 19.27 degrees. Then we also changed the ϑ angle to the correspondent Bragg angle as well. At this point we started tilting the sample's stage in both the χ and φ angular direction. At this point we launched theta scans and used the sintillator to record the reflected intensity so to obtain the correct position of the Bagg reflection in lab coordinates, which

In performing this set of acquisitions we kept the JJ slits aperture to 10x50 microns^2 and launched

a set of 10 scans around the Bragg angle which, in lab coordinates, was located to 19.750 degrees. After performing the usual steps of phase ramp removal, alignment and average phase calculation, we were able to obtain better reconstructions and in fact the phase profiles, shown below in Figure 7.21, are less noisy.

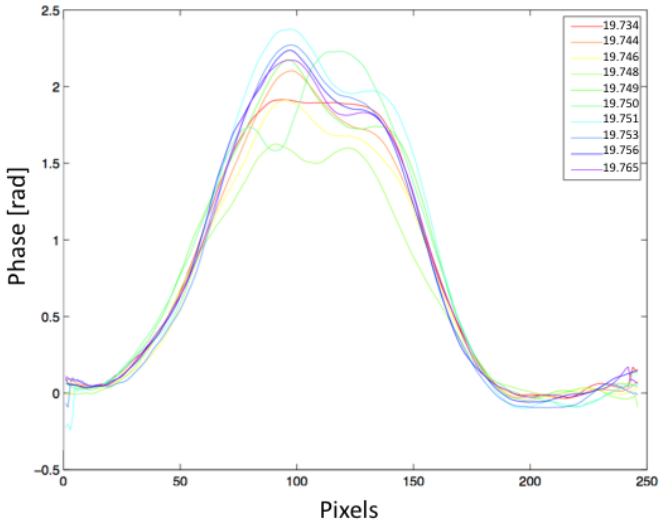

Figure 7.21: InP phase profiles forr the {220} reflection. The values in the legend are the angular lab coordinates of each scan.

It is worth highlighting that we can still see that the phase profiles are not flat inside the pillar. This is an important result because it demonstrates that what we found for the {111} reflection was not an artifact due to bad reconstructions but a real structure.

We went on conducting our data analysis by performing the kinematical fitting of our experimental results, as shown below in Figure 7.22.

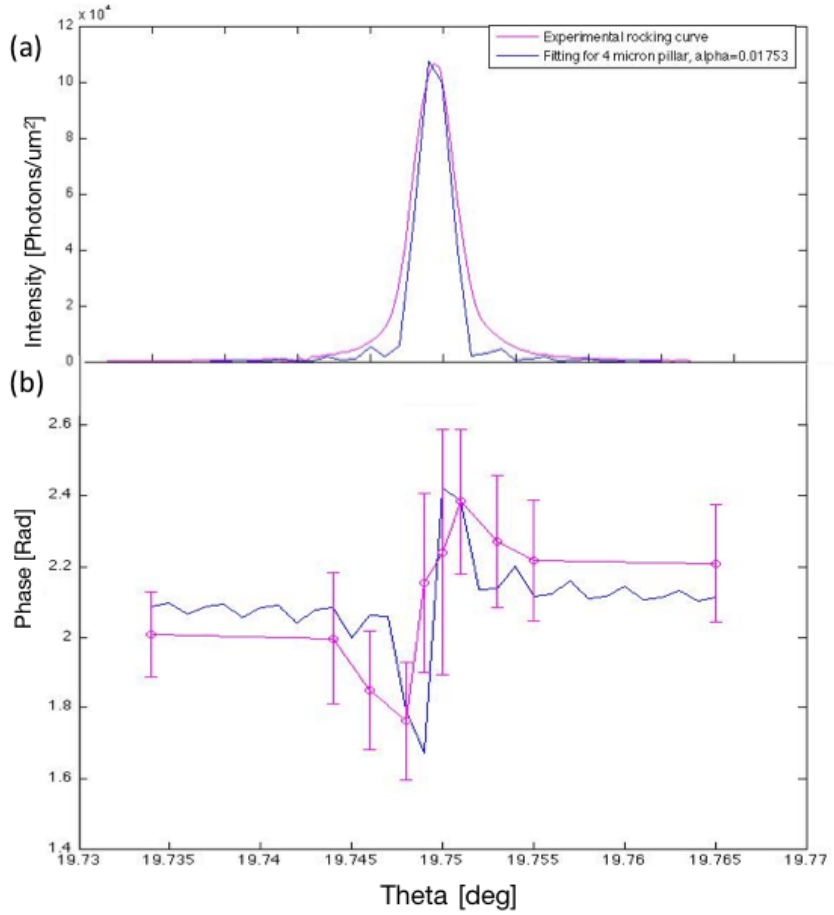

Figure 7.22: (a) Rocking curve and (b) phase shift fittings in the kinematical approximation for the {220} reflection.

Again the rocking curve fitting is quite good and the phase fitting is almost symmetrical and the larger deviation from the theoretical curve happens off the Bragg, at both sides. It is very interesting that the fitting is correct around the Bragg, which demonstrates that the internal structures inside the pillar which are more evident aroud the Bragg consition are real.

7.2.3 InP: {200} reflection

In performing this last set of acquisitions we modified the JJ slits aperture by opening the horizontal slits to 15 microns. Moreover, we also changed the scintillator inclination to $\theta = 45 + \theta_B$, where the Bragg angle is 13.49 degrees. After performing the set of procedures explained in the previous section,

we found that the position of the Bragg peak in the lab coordinates was of 14.769 degrees.

We performed a set of 12 ptychographic scans around the Bragg angle and after correctiog for phase ramps and lateral shifts of the sample, we obtained the linear phase profiles shown below in Figure 7.23.

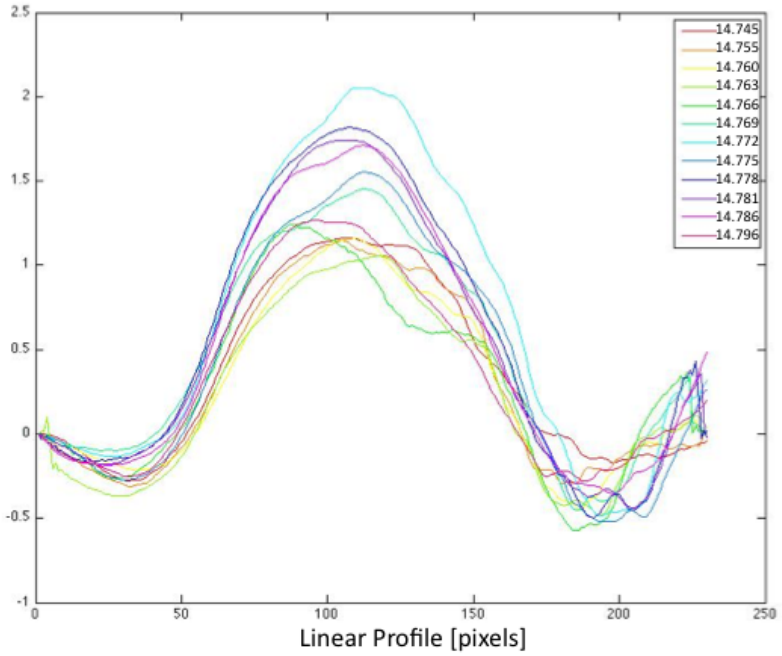

Figure 7.23: Linear phase profiles for the {200} reflection. The legend shows the complete set of angular positions.

In this case we can see that there is some noise that could not be corrected because in this case the reconstructions were not as good as before, maybe again due to the long scans and the implied difficulty in considering the beam stable for such a long time. However, despite a small phase ramp still persistent, we can still see that there is a phase structure inside the pillar and in particular it looks like this structure is more evident around the Bragg condition and tends to fade off Bragg.

At this point we went on with our analysis by drawing once again our boxes inside and outside the pillar in order to retrieve the average phase and the errorbars measures for each angular scan. The result is presented in Figure 7.24.

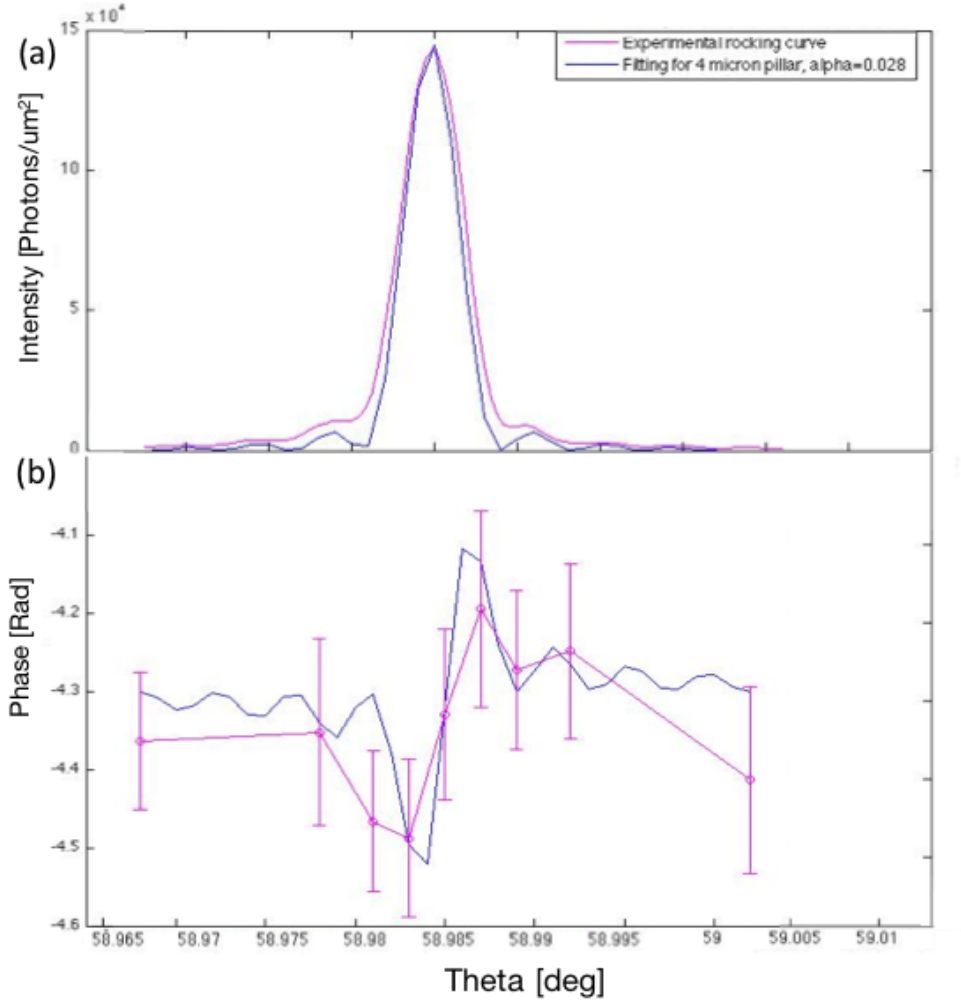

Figure 7.24: (a) Rocking curve and (b) phase shift profile fittings in the kinematical approximation.

In this case the phase shift profile fitting presents big error bars, but is symmetrical and it is following the theoretical curve trends.

Chapter 8

Conclusions

At the beginning of this PhD course I took part to my first experiment on gold nanocrystals perfomed at the cSAXS beamline at the Swiss Light Source. This experiment gave our research team those promising results that signed the path of my PhD project. From that first stage onwards I have been involved in all the aspects of this project: from data analysis to theoretical research, from sample development and preparation to experimental implementation. The structure of this Thesis follows this journey and shows almost chronologically all the steps that I took. In this final section conclusions will be discussed following the same approach. At the beginning the structure factor calculation, previously discussed in Chapter 4, will be presented for all our samples for different reflections. Then more attention will be devoted to how unit cells can be defined and to how this may or may not affect the experimental results. Finally experimental results will be discussed to draw the outcomes of this research.

8.1 Structure factor

The structure factor calculation has alredy been discussed in Chapter 4, but for the sake of clarity here I recall Equation 4.22

$$F\left(hkl\right) = \sum_{j}^{N} f_j e^{2\pi i(hx_j + ky_j + lz_j)}$$

where N is the number of atoms in the unit cell, f_j is the scattering power of the jth scattering element and the quantity in brakets represent the dot prduct between the scattering vector $\mathbf{q}$ and the direction

vector **r** that defines the coordinates of the each atom.

The following calculations will be performed under several assumptions. Given that all Au, Si and InP lattices have a FCC structure, here we will consider the conventional unit cell that has 4 atoms in the case of Au and 8 for both Si and InP, as shown below in Figure 8.1.

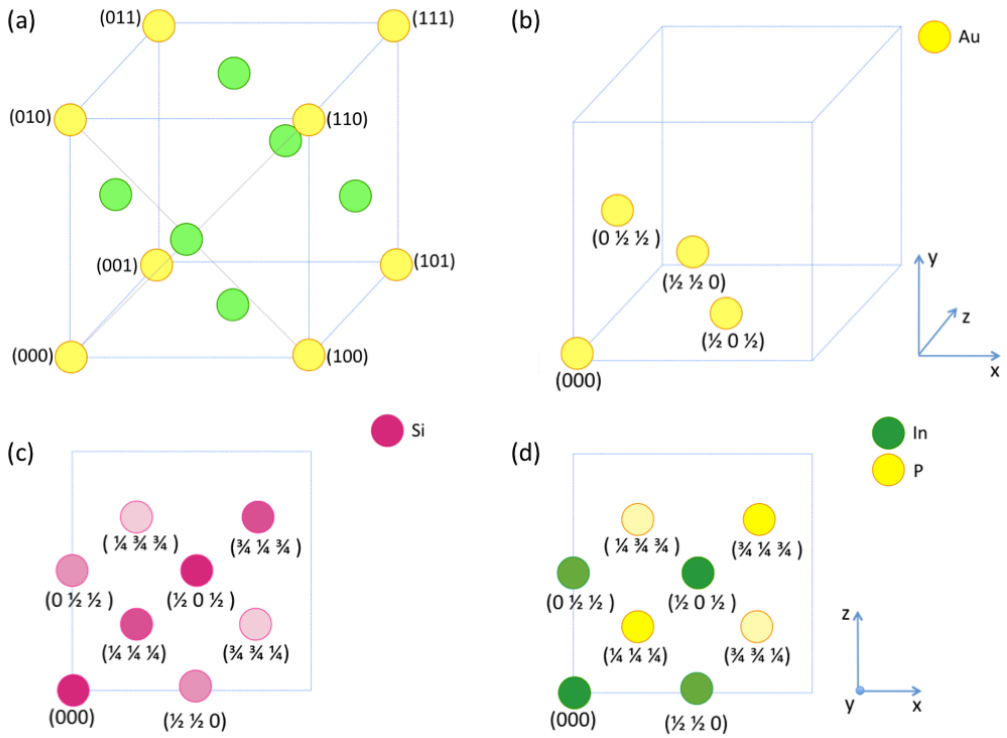

Figure 8.1: (a) 3D view of the conventional unit cell for the FCC lattice. In this structure there are 8 atoms distributed as shown: the yellow dots represent atoms at the vertices of the cube, while the green ones are at the centre of each facet. (b) 3D view of the Au conventional unit cell. Here we consider 4 atoms whose spatial coordinates are shown in the figure. (c) Top view of the Si unit cell. The coordinates are shown by each atom and the various shades refer to a different y-level. (d) Top view of the InP unit cell, where the two components are shown in green and yellow, respectively. The choice of placing the In at (000) is arbitrary and it might affect the results of the structure factor calculation as it will be later discussed in the text.

At this point one can go back to the structure factor equation and start calculating the results for all cases. For the simplest Au structure we have $N = 4$ and the **r** coordinates are those shown in the

figure which for simplicity can be summarized as

$$(x_j, y_j, z_j) = \begin{cases} (0,0,0) \\ \left(\frac{1}{2}, \frac{1}{2}, 0\right) \\ \left(\frac{1}{2}, 0, \frac{1}{2}\right) \\ \left(0, \frac{1}{2}, \frac{1}{2}\right) \end{cases} . \tag{8.1}$$

In order to calculate the structure factor for the various reflections the **q** vector components will change accordingly by taking into account the various Miller indices sets. The last quantity that needs to be defined is the scattering power f_j. Under the assumption that we are considering spherical atoms, thus neglecting all chemical bonds, and that we are estimating the scattering power at the centre of each atom we can write

$$f = Z, \tag{8.2}$$

where Z is the atomic number. For the Au case$f_j = f = Z_{Au} = 79$ electrons.

The calculation for Si is the same with the difference that here we consider 8 atoms in the unit cell, where the first 4 are spatially located as described in Equation 8.1 and the next 4 are placed as

$$(x_j, y_j, z_j) = \begin{cases} \left(\frac{1}{4}, \frac{1}{4}, \frac{1}{4}\right) \\ \left(\frac{3}{4}, \frac{3}{4}, \frac{1}{4}\right) \\ \left(\frac{3}{4}, \frac{1}{4}, \frac{3}{4}\right) \\ \left(\frac{1}{4}, \frac{3}{4}, \frac{3}{4}\right) \end{cases} . \tag{8.3}$$

In this case the scattering power, or form factor, is $f_j = f = Z_{Si} = 14$.

The same assumptions can be made for the InP calculation with the important difference that here we consider two different atoms in the unit cell. We know that the conventional unit cell structure has 8 atoms which are equally divided into the two elements. At this point we need to make the assumption that either In or P are at the origin of our coordinates system. If we place In at (000) this means that the 4 In atoms will be dislocated following the four sets of coordinates in Equation 8.1, while the remaining P atoms will follow Equation 8.3, as also shown in Figure 8.1.d. Otherwise

we can exchange the positions of the two elements and consider P at the origin. This difference does affect the structure factor calculation because the phase for the 200 and 220 reflections will be 0 or π in accordance with the chosen system. Furthermore, because In and P have different atomic number, the sum in Equation 4.22 is split into two separate components as

$$F(hkl) = \sum_{j}^{N} f_{In,j} e^{2\pi i(hx_{In,j}+ky_{In,j}+lz_{In,j})} + \sum_{j}^{N} f_{P,j} e^{2\pi i(hx_{P,j}+ky_{P,j}+lz_{P,j})} \tag{8.4}$$

where $N = 4$ for each sum and

$$\begin{cases} f_{In} = Z_{In} = 31 \\ f_P = Z_P = 13 \end{cases}.$$

A table summarizing the structure factors calculations for a set of different reflections is shown below in Table 8.1.

Reflection	Au		Si		InP	
	amplitude	phase	amplitude	phase	amplitude	phase
100	0	-	0	-	0	-
111	316	0	79.19	-π/4	134.46	-π/8**
110	0	-	0	-	0	-
200	316	0	0	-	72	0 or π*
222	316	0	0	-	72	0 or π*
220	316	0	112	0	176	0
400	316	0	112	0	176	0

* depending on the atom considered at the origin: 0 for In and π for P
** considering In at (000)

Table 8.1: Structure factor calculations for different crystallographic planes. The amplitude calculation shows values in number of electrons. In the case the structure factor results in a positive real value, the phase is shown with a zero, while in the case the amplitude is zero, the phase is not defined hence it is showed with a dash. In the InP case we need to distinguish the two scenarios where either In or P are at the (000) position. The $-\pi/8$ value, which is an approximation for -22.75 degrees, is obtained when considering In at (000), while π refers to a negative real value that is obtained in the calculations when considering the P atom at the unit cell origin.

The InP case is different from the Au and Si conditions because here we can arbitrary decide which

atom to put at the center of or coordinates system. If we exchange the positions the amplitude remains the same, but the phase value is different. It is also worth noticing that when considering the $\{\overline{111}\}$ reflection the resulting structure factor is the complex conjugate of the one obtained for the $\{111\}$ case. A summary is showed in Table 8.2.

Reflection	In at (000)		P at (000)	
	amplitude	phase	amplitude	phase
111	134.46	-22.75	134.46	-67.24
$\overline{111}$	134.46	22.75	134.46	67.24

Table 8.2: Structure factor calculation for InP considering both $\{111\}$ and $\{\overline{111}\}$ reflections. The phase values are showed in degrees.

8.2 Phase of the scattered beam

As previously discussed in Chapter 5, with these experiments we retrieved the phase of the transmitted beam collected in the far field and, in order to fit our experimental data, we compared its phase to the theoretical one, obtained by taking the reflected beam into account. The assumption at the basis of this way of operating is that the generation of the scattered wave R takes some energy away from the forward direction T. This quantity is of course complex and can be quantified in both amplitude and phase. We can then simply write that

$$|T(\mathbf{Q})|^2 = 1 - |R(\mathbf{Q})|^2 \tag{8.5}$$

where the minus sign refers to this behaviour and can be considered as a phase difference of π between R and T. The scattered wave R is complex and its phase, measured for different Bragg reflections, inglobates the structure factor information. Before discussing this point further, it is worth noticing that there also are other phase contributes that need to be taken into acount.

The choice of the spatial coordinates origin is arbitrary and we made the assumption to identify this point to one of the cubic unit cell's vertices. By following this approach we calculated the structure factors and their phases for different reflections. However it is worth highlighting the fact that by shifting the origin we can introduce an additional phase. For example, in the one dimensional case

where we shift the origin by 1/2 we obtain an additional phase of π as

$$e^{i2\pi\left(0+\frac{1}{2}\right)} = e^{i2\pi*0} * e^{i2\pi*\frac{1}{2}} = 1 * e^{i\pi}. \tag{8.6}$$

In the 3D case this phase will apply to all spatial directions in the same way. Figure 8.2 summarizes how this additional contribute affects the transmitted beam's phase.

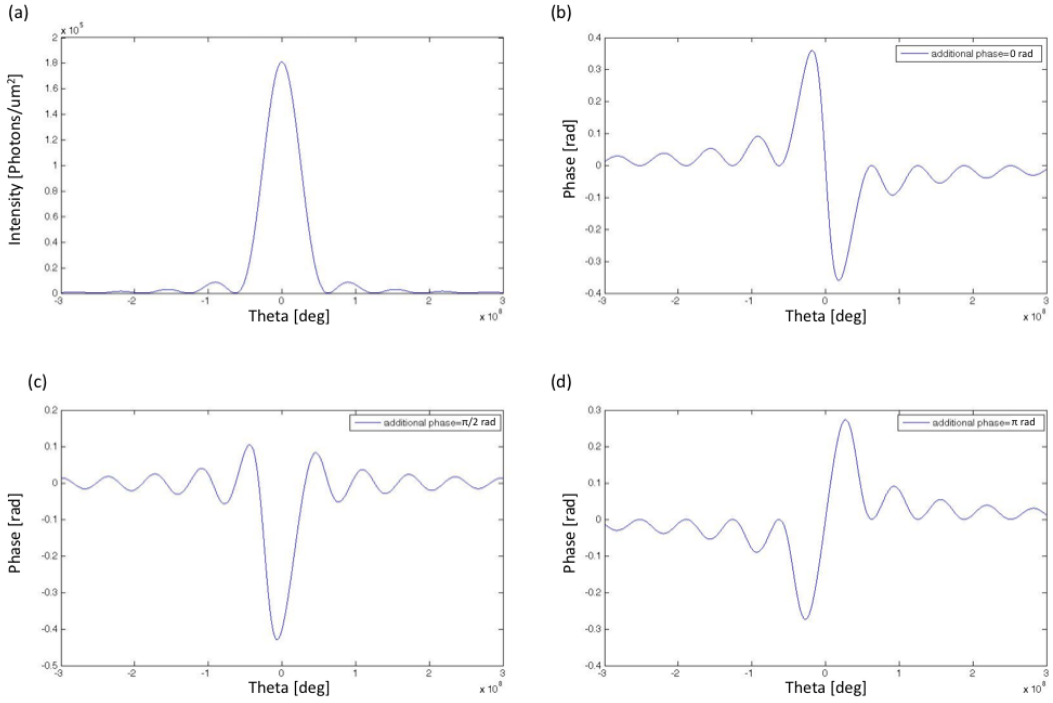

Figure 8.2: (a) Rocking curve. (b) Transmitted beam's phase with no additional contribute. (c) and (d) show the transmitted beam's phases for the additional contributes of $\pi/2$ and π, respectively.

Another aspect that can similarly affect the phase of the scattered wave is the way the experiment is performed. For example, when comparing the two experimental setups that we used, we saw that the rotation angles of our sample's stages were moving differently respect to the detectors in the scattering direction. For example, at the cSAXS beamline the Pilatus 100k detector that we used to collect the scattered beam was below the sample's plane in a direction opposite to the rotation angle that we used to perform our acquisitions. On the other side, the scintillator detector that we used at APS's 34-IDC beamline was positioned on the sample's plane (or above in accordance with the reflection being

considered) in the same direction of the rotation angle. For simplicity the two setups are schematically represented in Figure 8.3.

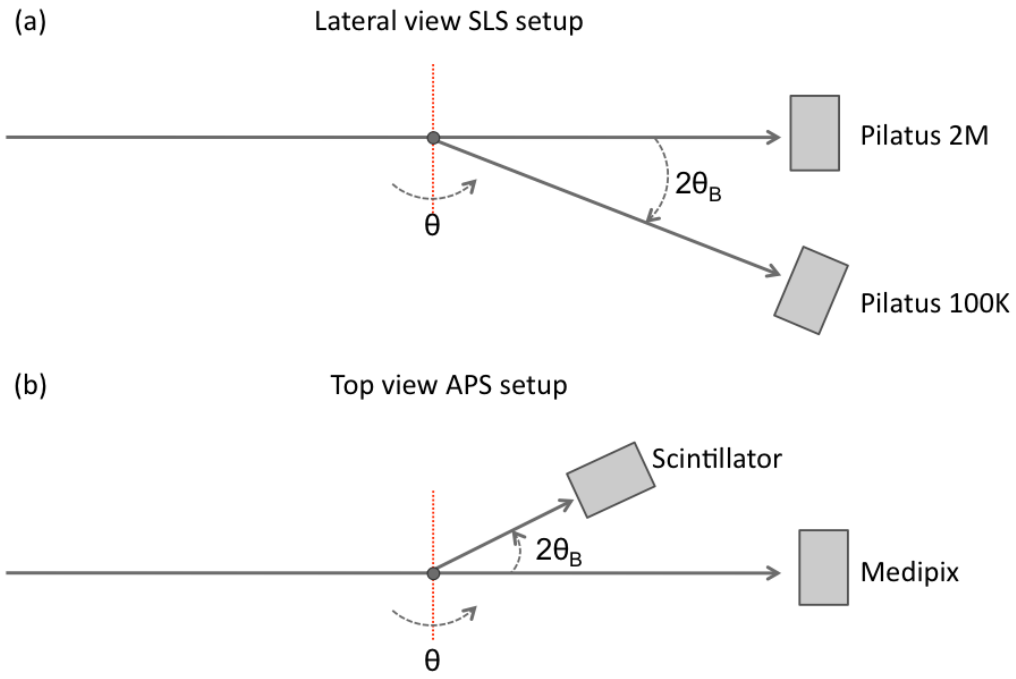

Figure 8.3: (a) Lateral view of the cSAXS setup. (b) Top view of the 34-IDC setup.

When comparing the phase shift profiles obtained from the two experimental setups, we immediately saw that there was a π phase correction, as shown below in Figure 8.4. We believe that this effect is not a consequence of the spatial coordinates used to define the atoms in the unit cell but it is only a result of the setup in the sense that that the scanning angles were defined in a different way. The main reason for stating this is that the phase correction only appears for both Si and InP, whose experiments where performed at APS by using the same setup.

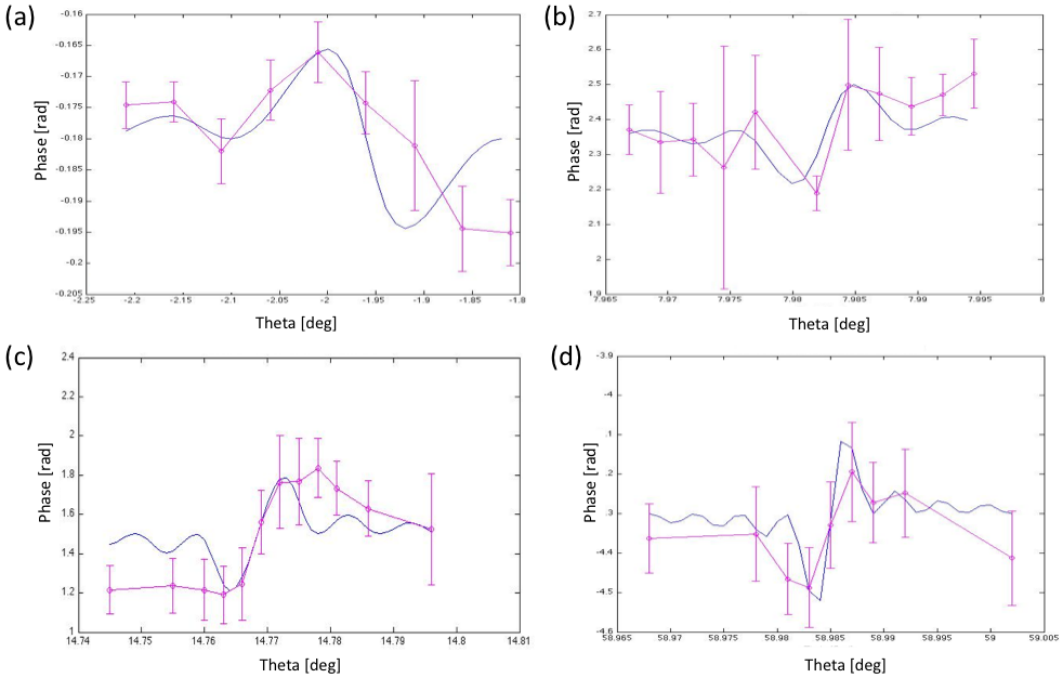

Figure 8.4: Phase shift fittings for different materials: Au {111} reflection (a), Si {111} reflection (b), InP {111} and {200} reflections (c) and (d) respectively. The theoretical fitting is shown in blue and it is easy to see that there is a phase contribution of π that affects all the profiles for both Si and InP.

8.3 Structure factor phase

During the whole thesis we have discussed many times the fact that the phase of the scattered beam R affects the resulting transmitted wave T. We were able to fit our experimental data in the kinematical approximation by calculating R as a superposition of scattering vectors

$$\alpha R_N(\mathbf{q}) = \alpha \sum_{\mathbf{j=0}}^{\mathbf{N-1}} \mathbf{e^{q \cdot d_j}} = \alpha \frac{1 - e^{iqN}}{1 - e^{iqd}}$$

where N represents the number of cristallographic planes, d is the distance between two layers and α is a real parameter that we used to do our fittings. In Chapter 5, when discussing the gold nanocrystal experiment, we also showed how this kinematical fitting can be compared with the dynamical one and we concluded that the two results agreed with each other. We now want to focus our attention to what happens when considering the scattered and transmitted waves in both amplitude and phase. In this

approximation we will consider the equation

$$T(\mathbf{q}) = 1 - \alpha R(\mathbf{q}) \tag{8.7}$$

which is different from Equation 8.5 because it violates the conservation of energy, but it is still consistent with the kinematical approximation. Figure 8.5 graphically shows how the transmitted wave is obtained from the scattered beam for different rocking angles.

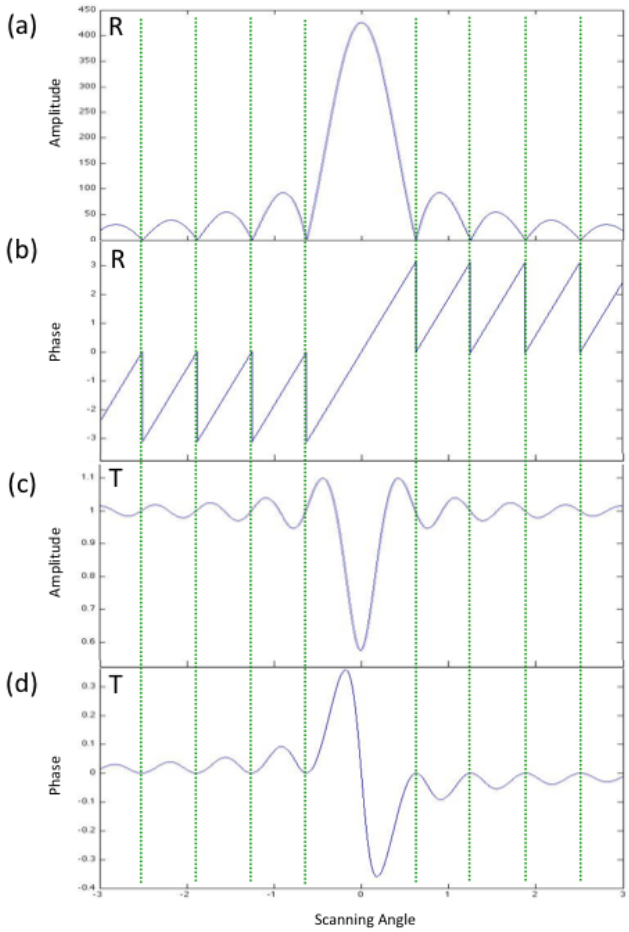

Figure 8.5: Scattered and transmitted beam's amplitudes (a-c) and phases (b-d). In this representation the Bragg angle is at 0 degrees and corresponds to the angular position where whe have the rocking curve's maximum value (a).

The curve obtained for the phase of the transmitted wave is consistent with what we found in the

experimental phase profiles. If we now consider a complex factor α which can be written as

$$\alpha = \alpha_0 e^{i\psi}, \tag{8.8}$$

we can see how the additional phase affects the phase of the transmitted wave. The result of this calculation for a set of equally spaced phases between 0 and π is showed below in Figure 8.6.

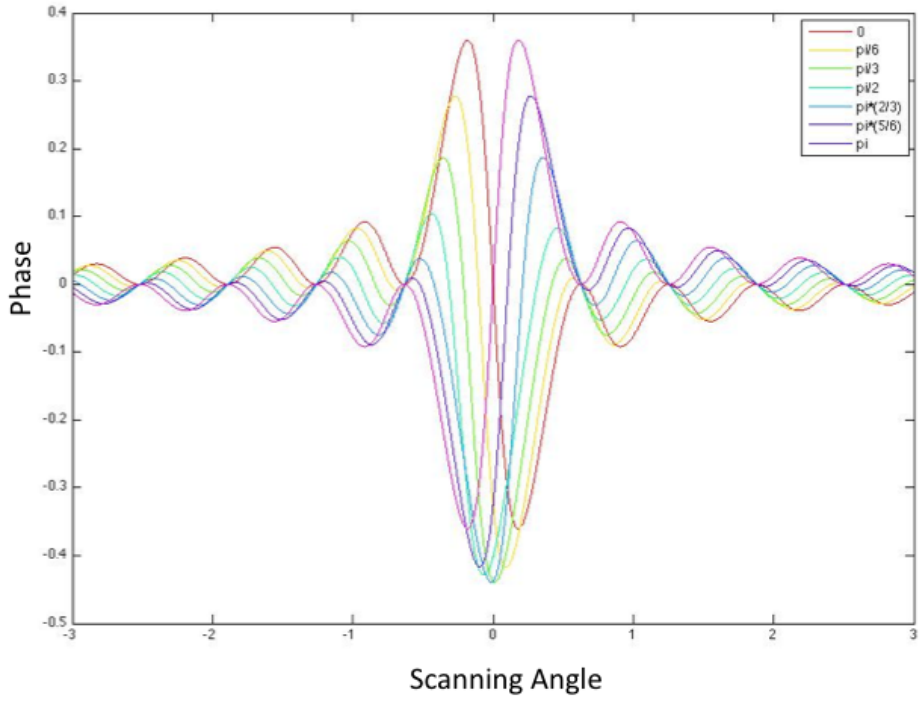

Figure 8.6: An additional phase component affects the transmitted wave's phase by shifting its profile in different ways. It is worth noticing that this effect is different in the Bragg's angle region where the zero-crossing point moves every time. On the other hand, off the Bragg condition the zero-crossings remain always the same.

The possibility to extract the phase of the structure factor from the transmitted wave is still being debated and in fact it is the object of future publications. According to private communications that we had with other research teams, we could learn that when considering the dynamical approximation the phase variation in the transmitted wave should include a factor

$$F_{hkl} * F_{\overline{hkl}} \tag{8.9}$$

where F_{hkl} is the structure factor for a given {hkl} reflection. The phase of this factor should appear for non-centrosymmetric structures where the angular contribute of $F_{\overline{hkl}}$ should be different from the phase of F_{hkl}. In our experiments we had InP whose lattice structure should satisfy what is required by this theory, however we calculated the structure factors for different reflections and, as showed in Table 8.2, we saw that $F_{\overline{hkl}}$ is just the complex conjugate of F_{hkl}. For this reason we concluded that the phase of the structure factor, no matter the symmetry of the crystal, should not be seen from the transmitted beam.

The phase shifts of the transmitted waves can be easily estimated from the profiles shown in the previous chapters. In the cases of Si and InP they are quantified in 0.3 and 0.4 radians respectively, as shown below in Figure 8.7. For the experimental data, which are highly constrained by the rocking curve, we could see that the best additional phase contribute ψ defined as

$$T(\mathbf{q}) = 1 - \alpha_0 R(\mathbf{q})\, e^{i\psi} \tag{8.10}$$

is within error of 0. This is also shown in Figure 8.7 where the additional phases are plotted in green. As one can easily see the experimentally determined phase shift is of $\psi = 0 \pm 0.4$ rad.

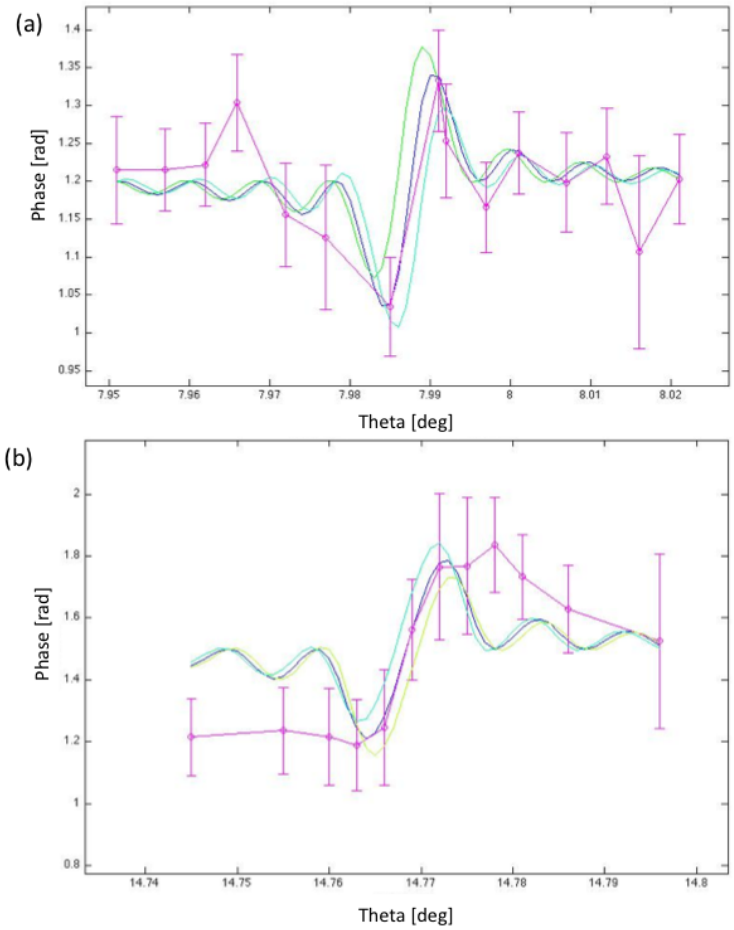

Figure 8.7: Si (a) and InP (b) phase shift fittings for the {111} reflection. The green lines refers to additional phase contributes of ±0.4 rad.

In conclusion, through these experiments we showed a method to measure how the phase of the direct beam transmitted through a crystal can change whenever a Bragg peak is generated. We saw that, despite what one can theoretically imagine, the way one defines the unit cell's coordinates does not have an impact with the final result. This is consistent with the fact that the lattice representation is a way that one can use to describe the materials and its definition can be arbitrary, but nevertheless the real structure of our samples remains the same, so for this reason we can't have different results in the actual experiment. Furthermore, we also saw that the way the experimental setup is defined can have an impact in the retrieved phase. In particular we could quantify in a phase shift of π the

impact of the scanning angle direction respect to the reflection detector position.

Finally we could demonstrate that the phase of the transmitted beam can be derived from the scattered beam and that for our experimental data the best additional phase contribute ψ is within error of 0. Whether we should be able to see the phase of the structure factor in the transmitted wave is still being debated. According to our investigation it should not be possible to detect it because the structure factor phase component should disappear when considering the transmitted wave. However other research teams are investigating this effect, sustaining that there are cases where one should be able to measure the phase of the structure factor. Whether this is going to be demonstrated or not is something that we will be able to see in future works.

List of Figures

List of Tables

Bibliography

[1] G. Bricogne. Maximum-entropy and the foundations of direct methods. *Acta Crystallographica*, A40:410–445, 1984.

[2] H. Hauptman and J. Karle. The probability distribution of the magnitude of a structure factor. *Acta Crystallographica*, 6:136–141, 1953.

[3] H.J. Juretschke. Invariant-phase information of x-ray structure factors in the 2-beam bragg intensity near a 3-beam point. *Phys Rev Lett*, 48:1487–1489, 1982.

[4] S.L. Chang, H.E. King, M.T. Huang, and Y. Gao. Direct phase determination of large macromolecular crystals using 3-beam x-ray interference. *Phys Rev Lett*, 67:3113–3116, 1991.

[5] Q. Shen. Solving the phase problem using reference-beam x-ray diffraction. *Phys Rev Lett*, 80:3268–3271, 1998.

[6] A. Authier. Dynamical theory of x-ray diffraction. *Oxford University Press*, 2001.

[7] Q. Shen and R. Colella. Phase observation in an organic-crystal (benzil-c14h10o2) using long-wavelength x-rays. *Acta Crystallographica*, A44:17–21, 1988.

[8] E. Weckert and K. Hummer. Multiple-beam x-ray diffraction for physical determination of reflection phases and its applications. *Acta Crystallographica*, A53:108–143, 1997.

[9] K. Hirano and A. Momose. *Phys Rev Lett*, 76:3735, 1996.

[10] E. Wolf. Solution of the phase problem in the theory of structure determination of crystals from x-ray diffraction experiments. *Phys Rev Lett*, 103:075501, 2009.

[11] Rodenburg JM et al. Hard-x-ray lensless imaging of extended objects. *Physical Review Letters*, 98, 2007.

[12] H.M. Faulkner and J.M. Rodenburg. A phase retrieval algorithm for shifting illumination. *Applied Physics Letters*, 85:4795–4797, 2004.

[13] Takeo Kamino Joachim Mayer, Lucille A. Giannuzzi and Joseph Michael. Tem sample preparation and fib-induced damage. *MRS Bulletin*, 32:400–407, May 2007.

[14] Susan Swapp. Scanning electron microscopy (sem). *University of Wyoming, Geochemical Instrumentation and Analysis department.*

[15] H. Rohrer G. Binnig. Scanning tunneling microscopy. *IBM Journal of Research and Development*, 30:4, 1986.

[16] Gerber Ch. Binning G., Quate C. F. Atomic force microscope. *Physical Review Letters*, 56:930:936, 1986.

[17] C. Jacobsen J. Kirz and M. Howells. Soft x-ray microscopes and their bio- logical applications. *Quarterly Reviews of Biophysics*, 28(1):33–130, 1995.

[18] Richard Bean. *Domain Structure Imaging with Bragg Geometry X-ray Ptychography.* PhD thesis, London Centre for Nanotechnology, University College London, 2012.

[19] McMorrow D. Nielsen J.A. *Elements of Modern X-ray Physics.* Wiley, 2011.

[20] Baez A. Kirkpatrick P. Formation of optical images by x-rays. *Journal of the Optical Society of America*, Vol 38, Num 9:766–774, 1948.

[21] Snigireva et. Refractive x-ray lenses. *Journal of Applied Physics*, 38:218–222, 2005.

[22] W Chao. Soft x-ray microscopy at a spatial resolution better than 15 nm. *Nature*, 435:1210–1213, 2005.

[23] Schmahl G. Niemann B., Rudolph D. X-ray microscopy with synchrotron radiation. *Applied Optics*, 15:1883–1884, 1976.

[24] M. Lerotic. *Finding the patterns in complex specimens by improving the acquisition and analysis of x-ray spectromicroscopy data.* PhD thesis, State University of New York at Stony Brook, 2005.

[25] Kirz J. Howells M. R. Chang P. Coane P.J. Feder R. Houzego P. J. Kern D. P. Sayre D. Rarback H., Kenney J. M. Recent results from the stony brook scanning microscope. *X-Ray Microscopy*, 43:203–215, 1984.

[26] Jacobsen C. Hornberger B., Feser M. Quantitative amplitude and phase contrast imaging in a scanning transmission x-ray microscope. *Ultramicroscopy*, 107:644–655, 2006.

[27] M. G. L. Gustafsson. Surpassing the lateral resolution limit by a factor of two using structured illumination microscopy. *Journal of Microscopy*, 198:82–87, 2000.

[28] Shao L. Carlton P. M. Wang C. J. R. Golubovskaya I. N. Cande W. Z. Agard D. A. Sedat D. A. Gustafsson, M. G. L. Three-dimensional resolution doubling in wide-field fluorescence microscopy by structured illumination. *Biophysical Journal*, 94:4957–4970, 2008.

[29] Juskaitis R. Wilson T. Neil, M. A. A. Method of obtaining optical sectioning by using structured light in a conventional microscope. *Optics Letters*, 22(24):1905–1907, 1997.

[30] Juskaitis R. Wilson T. Neil, M. A. A. Real time 3d fluorescence microscopy by two beam interference illumination. *Optics Communications*, 153:1–4, 1998.

[31] Squire A. Juskaitis R. Bastiaens P. I. H. Wilson T. Neil, M. A. A. Wide-field optically sectioning fluorescence microscopy with laser illumination. *Journal of Microscopy*, 197:1–4, 2000.

[32] Herriott H. D. Gallagher J. E. Rosenfeld D. P. White A. D. Brangaccio D.J. Bruning, J. H. Digital wavefront measuring interferometer for testing optical surfaces and lenses. *Applied Optics*, 13(11):2693–2703, 1974.

[33] Gao M Zhang R Nagahara LA. Zuo JM, Vartanyants I. Atomic resolution imaging of a carbon nanotube from diffraction intensities. *Science*, 300(5624):1419–21, 2003.

[34] Onken J.D. Pfeifer M.A. Williams G.J. Pfeiffer F. Metzger H. Zhong Z. Bauer G. Vartanyants I.A., Robinson I.K. Coherent x-ray diffraction from quantum dots. *Physical Review B: Condensed Matter and Materials Physics*, 71:245302, 2005.

[35] Bates R.H.T. Fourier phase problems are uniquely sol- uble in more than one dimension.i: underlying theory. *Optik*, 61:247–262, 1982.

[36] Theory of signals class notes. Technical report, Politecnico di Milano.

[37] Chapman H. N. Miao J., Sayre D. Phase retrieval from the magnitude of the fourier transforms of nonperiodic objects. *J. Opt. Soc. Am.*, 15(6):1662–1669, 1998.

[38] Newsam G. Barakat R. Necessary conditions for a unique solution to two-dimensional phase recovery. *journal of Math. Phys.*, 25:3190–3193, 1984.

[39] J. R. Fienup. Phase retrieval algorithms: a comparison. *Applied Optics*, 21:2758–2769, 1982.

[40] Wackerman C. C. Fienup, J. R. Phase-retrieval stagnation problems and solutions. *J. Opt. Soc. Am.*, 3:1897–1907, 1986.

[41] M. Howells. Coherent x-rays and their applications, lecture 1. In *ESRF Experiments Division.*

[42] Hoppe W. Hegerl R. Ber. bunsenges. *Ptys. Chem*, 74:1148, 1970.

[43] Nellist P.D. Rodenburg J.M. Electron ptychography i: experimental demonstration beyond the conventional resolution limits. *Acta Crystallographica*, 54:49–60, 1998.

[44] Plamann T. Rodenburg J.M. Electron ptychography ii: theory of three-dimensional scattering effects. *Acta Crystallographica*, 54:61–73, 1998.

[45] J.M. Rodenburg, I. Johnson, K. Jefimovs, C. David, O. Bunk, F. Pfeiffer, B.R. Dobson, A.G. Cullis, and A.C. Hurst. Hard-x-ray lensless imaging of extended objects. *Phys Rev Lett*, 98:034801, 2007.

[46] Maiden A.M. Rodenburg J.M. An improved ptychographical phase retrieval algorithm for diffractive imaging. *Ultramicroscopy*, 109:1256–1262, 2009.

[47] J.M. Rodenburg. Ptychography and related diffractive imaging methods. *Advances in Imaging and Electron Physics*, 150:87–184, 2008.

[48] J. Miao, P. Charalambous, J. Kirz, and D. Sayre. Extending the methodology of x-ray crystallography to allow imaging of micrometre-sized non-crystalline specimens. *Nature*, 400:342–344, 1999.

[49] J.M. Rodenburg. Ptychography and related diffractive imaging methods. *Advances in Imaging and Electron Physics*, 150:87–184, 2008.

[50] A. Schopp, P. Boye, A. Goldschmidt, Honig S., and Hoppe R. J. Non-destructive and quantitative imaging of a nano-structured mi- crochip by ptychographic hard x-ray scanning microscopy. *Journal of Microscopy*, 241:9–12, 2011.

[51] K Giewekemeyer, P. Thibault, Kalbfleisch S., A. Beerlink, C. Kewisk, M. Dierolf, F. Pfeiffer, and T. Salditt. Quantitative biological imaging by ptychographic x-ray diffraction microscopy. *Proceedings of the National Academy of Sciences*, 107:529–534, 2010.

[52] M. Dierolf, Menzel A., Thibault P, P. Schneider, C.M. Kewish, R. Wepf, O. Bunk, and F. Pfeiffer. Ptychographic x-ray computed tomography at the nanoscale. *Nature*, 467:436–439, 2010.

[53] M. Dierolf, P. Thibault, A. Menzel, C.M. Kewish, K. Jefimovs, I. Schlichting, K. von Konig, O. Bunk, and F. Pfeiffer. Ptychographic coherent diffractive imaging of weakly scattering specimens. *New Journal of Physics*, 12:035017, 2010.

[54] E. Lima, A. Diaz, M. Guizar-Sicairos, S. Gorelick, P. Pernot, T. Schleier, and A. Menzel. Cryo-scanning x-ray diffraction microscopy of frozen-hydrated yeast. *J. Microscop.*, 249:1–7, 2013.

[55] P. Thibault and A. Menzel. Reconstructing state mixtures from diffraction measurements. *Nature*, 494:68–71, 2013.

[56] Cullis A. Rodenburg J.M., Hurst A. Transmission microscopy witwith lenses for objects of unlimited size. *Ultramicroscopy*, 107:227–231, 2007.

[57] Sweeney F. Midgeley P.A. Rodenburg J.M., Maiden A.M. Wave-front phase retrieval in transmission electron microscopy via ptychography. *Phys Rev B*, 82:121415–, 2010.

[58] Maiden A.M. Rodenburg J.M. An improved ptychographical phase retrieval algorithm for diffractive imaging. *Ultramicroscopy*, 109:1256–1262, 2009.

[59] Elser V. Phase retrieval by iterated projections. *Journal of the Physics Society of America*, 20:40–55, 2003.

[60] P. Thibault, M. Dierolf, A. Menzel, O. Bunk, C. David, and F. Pfeiffer. High-resolution scanning x-ray diffraction microscopy. *Science*, 321:379–382, 2008.

[61] P. Thibault, M. Dierolf, O. Bunk, A. Menzel, and F. Pfeiffer. Probe retrieval in ptychographic coherent diffractive imaging. *Ultramicroscopy*, 109:338–343, 2009.

[62] R.M. Goldstein, H.A. Zebker, and C.L. Werner. Satellite radar interferometry: Two-dimensional phase unwrapping. *Radio Science*, 23:713–720, 1988.

[63] W.L. Bragg. The structure of some crystals as indicated by their diffraction of x-rays. *Proc. R. Soc. Lond. A*, 89:248–277, 1913.

[64] Chen H. Kinematic diffration of x-rays. *Lecture notes-University of Illinois at Urbana-Champaign Urbana, IL, USA*.

[65] website. Crystal physics. *msheiksirajuddeen.blogspot.it*, 2011.

[66] website. Fourier transform. *www.roymech.co.uk*, 2010.

[67] P.P. Ewald. *Ann. Phys. Lpz.*, 54:519, 1917.

[68] Cole H. Batterman B. W. Dynamical diffraction of x-rays by perfect crystals. *Reviews of Modern Physics*, 36:681–717, 1964.

[69] A. Authier. *Dynamical Theory of X-Ray Diffraction*. Oxford University Press, New York, 2001.

[70] M. Guizar-Sicairos, A. Diaz, M. Holler, M.S. Lucas, A. Menzel, R. Wepf, and O. Bunk. *Optics Express*, 19:21345–21357, 2011.

[71] M. Guizar-Sicairos, S.T. Thurman, and J.R. Fineup. Efficient subpixel image registration algorithms. *Opt. Lett*, 33:156–158, 2008.

[72] S. Takagi. *, J. Phys. Soc. Japan*, 26:1239, 1969.

[73] J. Gronkowsky. *Phys. Rep*, 206:1, 1991.

[74] V.G. Kohn, I. Snigireva, and A. Snigirev. Theory of imaging a perfect crystal under the conditions of x-ray spherical wave dynamical diffraction. *Phys. Status Solidi B*, 222:407–423, 2000.

[75] Robinson I.K. Optimisation of coherent x-ray diffraction imaging at ultrabright synchrotron sources. *Z. Kristallogr. Suppl.*, 27:27–35, 2008.